Volume 1 , Issue 2 , December 2015 ISSN 2356-8569

مركز الأكاديمية للنشر
ACADEMY Publishing Center

Journal of Renewable Energy and Sustainable Development

RESD

Academy Publishing Center
Journal of Renewable Energy and Sustainable Development (RESD)
First edition 2015

Permissions may be sought directly Academy Publishing Center, Arab Academy for
Science, Technology, and Maritime Transport, Abu Kir Campus
Alexandria, EGYPT:
P.O. Box: Miami 1029
Tel:(+203) 5622366/88 – EXT 1069 and (+203) 561 1818
Fax: (+203) 561 1818
Web Site: http://apc.aast.edu

Volume 1, Issue 2, December 2015

ISSN: 2356-8518 Print Version

ISSN: 2356-8569 Online Version

Journal of Renewable Energy and Sustainable Development

RESD

Renewable Energy and Sustainable Development (RESD) is a biannual international peer-reviewed journal which presents a global forum for dissemination of research articles, case studies and reviews focusing on all aspects of renewable energy and its role in sustainable development. The topics of focal interest to RESD include, but are not limited to, all aspects of wind energy, wave/tidal energy, solar energy, as well as energy from biomass and biofuel. The integration of renewable energy technologies in electrical power networks and smart grids is another topic of interest to RESD. Experimental, computational and theoretical studies are all welcomed to RESD.

Sustainable development is a multidisciplinary advancing to the center of energy research with the declaration of UN millennium development goals for the first time in 2000, and continued to constitute a challenge in energy technologies in the past decade. RESD is mainly interested in case studies of sustainable development and its relation to transition economies in the Middle East, Africa, Asia and Oceania.

RESD has an outstanding editorial board of eminent scientists, researchers and engineers who contribute and enrich the journal with their vast experience in different fields of interest to the journal. The journal is open-access with a liberal Creative Commons Attribution-NonCommercial-NoDerivatives 4.0 International License. Which preserves the copyrights of published materials to the authors and protects it from unauthorized commercial use or derivation. The journal is financially supported by Arab Academy for Science, Technology and Maritime Transporting in order to maintain quality open-access source of research papers on renewable energy and sustainable development.

Editorial Commitee

Editor-in-Chief

Yasser Gaber Dessouky, Ph.D
Professor of Electrical Engineering and Renewable Energy Technologies
Arab Academy for Science and Technology and Maritime Transport (AASTMT)
Abu Kir Campus, POBox: 1029 Miami,
Alexandria, EGYPT
E-mail: ygd@aast.edu

Associate Editors

Rania El Sayed Abdel Galil, Ph.D.
Associate Professor, Architectural Engineering and Environmental Design
Arab Academy for Science and Technology and Maritime Transport (AASTMT)
Abu Kir Campus, POBox: 1029 Miami,
Alexandria, EGYPT
Email: rania@aast.edu

Ahmed Kadry A. Abdel-Salam , Ph.D.
Assistant Professor, Electrical and Control Engineering
Arab Academy for Science and Technology and Maritime Transport (AASTMT)
Abu Kir Campus, POBox: 1029 Miami,
Alexandria, EGYPT
Email: ahmed.abdel-salam@ieee.org

Aly Ismail Shehata , Ph.D.
Assistant Professor, Mechanical Engineering
Arab Academy for Science and Technology and Maritime Transport (AASTMT)
Abu Kir Campus, POBox: 1029 Miami,
Alexandria, EGYPT
Email: aliismail@aast.edu

Editorial Board

Abdel Salam Hamdy Makhlouf, PhD
Professor, University of Texas – Pan American, USA

Adam Fenech, PhD
Associate Professor, University of Prince Albert Island, CANADA

Adel Al Taweel, PhD
Professor, Dalhousie University, CANADA

Ahmed Zobaa, PhD
Senior Lecturer, Brunel University London, U.K

Aziz Naamane, PhD
Senior Researcher, Laboratoire des Sciences de l’information et des Systèmes, FRANCE

Barry Wayne Williams, Ph.D
Professor, Strathclyde University, U.K

Chin-Hsiang Cheng, Ph.D
Professor, National Cheng Kung University, TAIWAN

Dieter Schramm, PhD
Professor, University of Duisburg-Essen, GERMANY

Ehab Fahmy El-Saadany, Ph.D
Professor, University of Waterloo, CANADA

Fei GAO, PhD
Associate Professor, University of Technology of Belfort-Montbéliard, FRANCE

Francesco Martinico, PhD
Professor, Università di Catania, ITALY

Frede Blaabjerg, PhD
Professor, Allborg University, DENMARK

Fouad H. Fouad, PhD
Professor, University of Alabama at Birmingham, U.S.A

Han-Seung Lee, PhD
Professor, Hanyang University, SOUTH KOREA

Hassan M.K. Abdel-Salam, PhD
Professor, Alexandria University, EGYPT

Hebatalla F. Abouelfadl, PhD
Associate Professor, Faculty of Fine Arts, Alexandria University, EGYPT

Jawad Faiz, Ph.D
Professor, University of Tehran, IRAN

Kouzou Abdellah, PhD
Associate Professor, Djelfa University, ALGERIA

Mohamed Youssef, PhD
Assistant Professor, University of Ontario, Institute of Technology, CANADA

Mohamed Ismail, PhD
Professor, Hanyang University, SOUTH KOREA

Moustafa Abdel-Maksoud, Dr.-Ing
Professor, Hamburg University of Technology, GERMANY

Nacer Msridi, PhD
Senior Researcher, Laboratoire des Sciences de l'information et des Systèmes, FRANCE

Perter Breuhaus, PhD
Chief Scientist, International Research Institute Stavanger, NORWAY

Ping Zheng, PhD
Professor, Harbin Institute of Technology, CHINA

Robert F. Boehm, PhD
Professor, University of Nevada, Las Vegas, U.S.A

Robert W. Peters, Ph.D
Professor, University of Alabama, U.S.A

Sheldon Williamson, PhD
Associate Professor, University of Ontario, Institute of Technology, CANADA

Stephen Connelly, PhD
Senior Lecturer, The University of Sheffield, U.K

Suk Won Cha, PhD
Professor, Seoul National University, SOUTH KOREA

Susan Roaf, PhD
Professor, Heriot Watt University, U.K

Waleed F. Faris, PhD
Professor, International Islamic University of Malaysia, MALAYSIA

Yi-Tung Chen, Ph.D
Professor, University of Nevada Las Vegas, U.S.A

Youcef Soufi, PhD
Professor, University of Tébessa, ALGERIA

Advisory Board

Abbas Abdel Halim Yehia, PhD
Professor, Head of The Architectural, Engineering & Environmental Design, Department, Arab Academy for Science & Technology, Egypt

Abdel-Wahab Shalaby Kassem, PhD
Professor, Agricultural Engineering Department, Faculty of Agriculture, Alexandria University, Egypt

Adel Khalil, PhD
Professor, Mechanical Power Engineering Department Faculty of Engineering, Cairo University, Egypt

Ahmed Abu Saud, M.Sc
Chief Executive Officer (CEO) Of Egyptian Environmental Affairs Agency (EEAA)

Ahmed Hossam El-Din, PhD
Professor, Electrical Engineering Department, Alexandria University, Egypt

Almoataz Y. Abdelaziz, PhD
Professor, Faculty of Engineering, Ain Shams University, EGYPT

Amr A. Amin, PhD
Professor, Electric Power And Machines Department, Faculty of Engineering, Helwan University, Egypt

Anhar Ibrahim Hegazi, PhD
Director, Energy Efficiency Unit, IDSC, Egyptian Cabinet of Ministers, Egypt

Fatma Ahmed Moustafa Ali, PhD
Chairman for The Executive Committee for The Regional Center for Renewable Energy and Energy Efficiency (RCREEE), Egypt

Fatma El Zahraa Hanafi Ashour, PhD
Chairman, Chemical Engineering Department, Faculty of Engineering, Cairo University, Egypt

Fuad Ahmed Abulfotuh, PhD
Professor Emeritus, Alexandria University, Egypt

Galal Osman, PhD
Vice President, World Wind Energy Association (WWEA), Bonn, Germany

Hend Farouh, PhD
Executive Director of The Central Unit For Sustainable Cities & Renewable Energy, New Urban Communities Authority, NUCA

Khaled El Zahaby, PhD
Chairman, Housing And Building National Research Center, HBRC, Cairo, Egypt

Table of Contents

Editorial Articles

Sustainability and energy self-sufficiency; overcoming the barriers 230-231
Rania Abdel Galil
Associate Professor, Architectural Engineering and Environmental Design, Arab Academy for Science and Technology and Maritime Transport (AASTMT)

Changing Climate in the MENA Means Changing Energy Needs 232
Adam Fenech
Director of the Climate Lab at the University of Prince Edward Island, CANADA

Current and Future Trends of the Automotive Industry 233-234
Dieter Schramm
Prof. Dr.-Ing., Dean of Faculty of Engineering, Duisburg-Essen University, GERMANY

Sustainable Development is the only path to achieve the green economy 235
Ahmed Abou Elseoud
Chief Executive Officer (CEO) of Egyptian Environmental Affairs Agency (EEAA), EGYPT

Journal Articles

Modeling and Simulation of a Wind Turbine Driven Induction Generator Using Bond Graph 236-242
A. Ramdane, A. Lachouri and M. Krikeb

Implications of Human Induced Changes on the Distribution of Important Plant Species in the Northwestern Coastal Desert of Egypt 243-263
Marwa Waseem Halmy , Paul E. Gessler and Selim Z. Heneidy

Solitons and the new renewable energy approach 264-270
Mahmoud Akdi and Moulay Brahim Sedra

The Boost Converter – Revisited 271-293
B. W. Williams and T. C. Lim

Artificial Neural Network Algorithm for Condition Monitoring of DC-link Capacitors Based on Capacitance Estimation 294-299
Hammam Soliman, Huai Wang, Brwene Gadalla and Frede Blaabjerg

Investigation of Efficiency and Thermal Performance of the Y-source Converters Range for a Wide Voltage 300-305
Brwene Gadalla, Erik Schaltz, Yam Siwakoti, and Frede Blaabjerg

Sustainability and energy self-sufficiency; overcoming the barriers

Ass. Prof. Rania Abdel Galil

Engendering more positive attitudes to renewable energy is by no means a simple feat. Renewable energy technologies are viewed as radical innovations which necessitate substantial changes in production and consumption patterns, hence often met with resistance from both institutions and individuals. Yet action is needed; global energy consumption is expected to rise by 41% and global carbon dioxide emissions by 29%, with most of the demand and rise coming from emerging economies (BP energy outlook 2035). Further, countries need to meet objectives of reduction of GHG under the United Nations Framework Convention on Climate Change. Renewable energy share in the global energy mix needs to significantly increase in order to reach supply sufficiency, energy security, energy equity and environmental sustainability.

Meeting demands of energy is critical for the economic and social development of any country; energy must be secure, accessible and affordable at all levels of society, and any negative impact of energy production and energy use on the environment must be minimized. Middle East energy consumption is expected to grow by 69% whilst production to grow by 32%, with 97% of demand still met by fossil fuels by the end of the 2035. Energy investment of $316 billion will be required in the Middle East and North Africa (MENA) between 2015 and 2019 to meet its growing demand for power (Apicorp, 2014). Diversifying energy sources is indeed of interest in the MENA region, spurred by growing demand for power and desalinated water, fluctuating fuel price, GHG emission reduction targets, depleting fossil fuel reserves and advances in renewable energy technology. However, there are many barriers that hinder the adoption of renewable energy technologies worldwide, but more so in the MENA region. These barriers are political, economic, social and technological. With a focus on Europe and MENA, it can be said that these barriers have much in common albeit framing the struggle on the micro level in Europe and on the macro level in MENA.

On a political level, renewable energy policies in Europe are criticized as being uncoordinated, unstrategised and based on multiple interests, generally favouring macro level and inadequate to stimulate widespread adoption at the micro level. Similarly, in the MENA region, there is a lack of coordination between sustainable energy policies with other policy fields, namely economic, financial, environmental and social policy, with a lack of expertise in renewable energy policies and supportive policies for private investment. On an economic level, in Europe, sourcing and accessing finance is a major barrier for communities, with a lack appropriate organizational structures, the volatility of grant regimes and uncertain infrastructural costs perhaps associated with the near monopolistic position of some grid companies. Whereas in the MENA region, there are no incentives for economical use of energy, there is a lack of funding in public utilities in most countries, the investment climate is less attractive and a monopoly position of most electricity producers exists.

Technically, on a national level in Europe, a problem of the incompatibility of the new technologies with the current infrastructure (grid connection and capacity) are often identified as barriers, whilst on a community level, the lack of data on the efficiency of techniques, lack of technical skills and experience to implement renewable energy solutions act as barriers. In MENA, technologies involving the use of renewables have barely become established on the market and there is a significant lack of knowledge in the areas of technology transfer, marketing and the development of services within the energy sector. Finally, on a social level, the picture in the MENA region is bleaker. In Europe, governments and communities are well aware of the challenges laying ahead in terms of energy and some are well underway in achieving targets on the energy sustainability front (WEC, 2013). That is not to say that social barriers do not exist. They are manifested in the hindrance of knowledge transfer between social actors including misinformation, inadequate public consultation, and lack of inertia, access to relevant professional services, expertise and skills. Also, community concern over aesthetics, environmental issues and a perception of unequal distribution of benefits. However, in the MENA there is barely any awareness on the issue of energy security, equity and sustainability among individuals and the society, with lack of education and information on production and consumption, and no incentives for change. The rate of adoption, although not homogenous across the region, has been slow to date. Policy makers will not be persuaded to change, as a bottom-up approach is unlikely and the market will not develop accordingly, for lack of demand. Also, top-bottom approaches will be ineffective as the adoption of new systems are often met with resistance and the uptake will require change of entrenched practices and incentives for adoption.

Challenges to the wider adoption of renewable energy lie in two areas; provision and choice. The later can be overcome by awareness campaigns, incentive-based initiatives, and involving and empowering individuals and local communities in the development of renewable energy solutions. There is an urgent need to support initiatives in the MENA region to collaborate on environmental and energy related issues, build capacities to enable civil society engagement in the context of developing and implementing national energy plans and increase awareness on the needed shift towards a sustainable energy future. Meaningful global price for carbon is but one example to provide incentives for everyone to play their role in meeting the world’s increasing energy needs whilst combating climate change and maintaining good air and water quality. To conclude, a quote by the United Nations Secretary-General Ban Ki-moon comes to mind: “energy is the golden thread that weaves together economic growth, social equity, and environmental sustainability”. If sustainable development is to be realized, if there is to be a universal access to modern energy services and energy self-sufficiency, the share of renewable energy sources and the global rate of improvement in energy efficiency need to intensify, in addition to a strong shift of attitudes and policy towards cleaner choices of energy.

About Ass. Prof. Rania Abdel Galil

Associate Professor Rania Abdel Galil has graduated from Alexandria University, Faculty of Engineering. She was appointed in the Arab Academy for Science, Technology and Maritime Transport (AASTMT) till present. She received her PhD from Sheffield University, United Kingdom in 2007. Following her PhD, she accepted an appointment in the Department of Town and Regional Planning, Sheffield University, UK, where she taught for two years. During that time, she was a member in a winning bid for a research commissioned by the Parliamentary Commissioner for the Environment, New Zealand. She is now an associate professor in the Department of Architectural Engineering and Environmental Design, AASTMT. Besides teaching, she acted as RIBA coordinator over the last 5 years and currently liaises for international relations and training opportunities. Rania has presented in many international conferences, has been a member of the scientific and organizing committees and actively participated in numerous workshops and symposiums. She is the Associate-Editor of the Journal of Renewable Energy and Sustainable Development (Egypt) and an Editorial board member of the International Development Planning Review Journal (UK). She is a peer reviewer in several journals, supervised numerous PhD and MSc theses and has published over 20 research papers. Her research interests are in sustainability and the North/South divide.

Changing Climate in the MENA Means Changing Energy Needs

Dr. Adam Fenech

The leading authority on climate change, the Intergovernmental Panel on Climate Change (IPCC) has concluded that warming of the climate system is unequivocal, and will continue for centuries. The regions in the Middle East and Northern Africa (MENA) have experienced numerous extreme climate events over the past few years including the 2009 flooding in Jeddah, Kingdom of Saudi Arabia; the 2005 dust storm in Al Asad, Iraq; water scarcity throughout the Arab MENA; and the rising sea levels on the Nile Delta coast, Egypt. A climate baseline can be developed for regions in the MENA by locating climate stations in the study area using observations made in the Global Climate Observing System (GCOS). For projections of future climate, global climate models (GCMs), mathematical equations that describe the physics, fluid motion and chemistry of the atmosphere, are the most advanced science available. The Climate Research Lab at the University of Prince Edward Island has a dataset available to researchers, called the Climate, Ocean and Atmosphere Data Exchange (COADE), that provides easy access to the output from forty global climate models used in the deliberations of the Intergovernmental Panel on Climate Change's (IPCC) Fifth Assessment Report (AR5) including monthly global climate model projections of future climate change for a number of climate parameters including temperature and precipitation. Over the past 50 years, climate changes in the MENA Region have led to increases in annual mean temperatures and decreases in annual total precipitation. Applying all four greenhouse gas emission futures on a base climate normal of 1981-2010 to an ensemble of forty global climate models used in the Fifth Assessment Report of the Intergovernmental Panel on Climate Change (IPCC AR5) results in future temperature increases for the MENA Region ranging from 1.6 to 2.3 degrees Celsius, and in a range of future precipitation changes from reductions of 11 percent to increases of 36 percent by the 2050s (2041-2070). These preliminary results should assist the MENA Region in planning its energy needs and its needs for renewable energy through increasing the understanding of how climate has impacted the region in the past, and how climate will impact in the future.

About Dr. Adam Fenech

Dr. Fenech has worked extensively in the area of climate change since the Intergovernmental Panel on Climate Change First Assessment Report in 1988. He has edited 8 books on climate change, most recently on Climate Impacts and Adaptation Science. Dr. Fenech has worked for Harvard University researching the history of the science/policy interfaces of climate change. He has represented Canada at international climate negotiating sessions; written climate policy speeches for Canadian Environment Ministers; and authored Canadian reports on climate change to the United Nations. Dr. Fenech has taught at the University of Toronto as well as the Smithsonian Institution for almost 20 years, and lectures regularly at universities across Canada and around the world. He is presently the Director of the University of Prince Edward Island's Climate Research Lab that conducts research on the vulnerability, impacts and adaptation to climate change.

Current and Future Trends of the Automotive Industry

Prof. Dieter Schramm

Mobility, and especially individual physical mobility, is still an essential component of nearly all societies. The combustion engine was for more than a hundred years, and is still today, the backbone of road-based mobility. However, the guarantor for the triumphant advance of the combustion engine was by far not its technical superiority over its electrical rival at the beginning of the automobile era, but the energy density and the easy worldwide availability of fossil fuels as a means of energy storage. So, e.g. to store the energy equivalent of one kg Gasoline, a lithium ion battery with a mass of about 180 kg would be required (Schramm, 2012), even if the higher efficiency of the electric motor vs. the combustion engine is taken into account. Actually an electric motor is much better suited as a drive source for a motor vehicle as an internal combustion engine. Only the achievable energy density along with the cost of its chemical-process based storage, the battery, still prevent its immediate breakthrough in the automotive drive technology.

Nevertheless, the German Government has set the target to bring at least a million electrified motor vehicles on Germany's roads by 2020, which is already impossible to reach from today’s perspective. However, strategies are needed to achieve a sustainable transition to electric mobility. This, in addition to continued research on high-efficiency batteries which also includes the development of vehicles that offer a good compromise between coverage, costs and consumption while satisfying the mobility needs of their users.

Another trend that will lead to a paradigm shift in the use of individually-powered vehicles is the automation of the task of driving up to the highly automated or even autonomous vehicle. The technical prerequisites like sensors and actuators for these new systems are already available at least for application on motorways and rural regions, e.g. in Germany. More activities are required for robust algorithms and strategies to hand over control back to the driver in complex situations and even vice versa from the driver to the car in cases where the driver is unable to further control his car, e.g. in case of a heart attack. Another open field is the question of the responsibility in case of an accident along with even ethic problems.

A widely uncharted aspect is the individual customer who is expected and needed to buy the vehicle and his/her behaviour of vehicle use. For this reason currently a variety of activities is underway to find out how cars are actually being used in different countries. Those different usage scenarios would have a significant effect on the availability, environmental impact and economics notably of electrified vehicles. So a project funded by the German government is the Ruhr Car Sharing Project operated by the University of Duisburg-Essen and their partners for several years especially for electric and hybrid vehicles (Tewiele et al., 2015). Still unidentified, however, is the influence of a large proportion of electrified and highly automated vehicles on consumption, the total CO2 emissions and traffic jams (Jeschke et al., 2014). For this purpose extensive field experiments are conducted along with activities using simulation models to predict these impacts reliably for the future. It has to be made possible to successfully derive development strategies for Europe and other regions as well (Schüller et al., 2015).
Despite all difficulties, we are confident that there will be solutions for robust environment friendly technical solutions, acceptance by humans and even legal obstacles. As Albert Einstein once said, “Amid the difficulty lies opportunity.”

References

[1] Jeschke S, Hirsch H, Koppers M and Schramm D (2014) Investigations on the impact of different electric vehicle traction systems in urban traffic. In Vehicle Power and Propulsion Conference (VPPC) 2013, S 1 - 6 IEEE Beijing, China.

[2] Schramm D (2012) Diversity of Future Mobility - Automotive Landscape 2025. (ed.), Duisburg.

[3] Schüller M, Tewiele S, Bruckmann T and Schramm D (2015) Evaluation of alternative drive systems based on driving patterns comparing Germany, China and Malaysia. in 3rd International Conference on Recent Advances in Automotive Engineering & Mobility Research (ReCar)(ed.), Malakka, Malaysia.

[4] Tewiele S, Schüller M, Koppers M and Schramm D (2015) Driving Pattern Analysis of Hybrid and Electric Vehicles in a German Conurbation including a Drive System Evaluation. in 3rd International Conference on Recent Advances in Automotive Engineering & Mobility Research (ReCar)(ed.), Malakka, Malaysia.

About Prof. Dieter Schramm

Dieter Schramm graduated in mathematics at the University of Stuttgart in 1981, worked there from 1981-1986 as a research assistant and received his PhD in Engineering in 1986. From 1986-1998 he worked at Robert Bosch GmbH as group leader and department head of predevelopment and series development departments for automotive systems. He joined Tyco Electronics Ltd.

in 1999 and held the positions of Director Global Automotive Engineering and later CEO of Tyco Electronics Pretema GmbH until 2003. In 2004 he was appointed Full Professor and head of the Chair of Mechatronics at the University of Duisburg-Essen and in 2006 he was elected Dean of the Faculty of Engineering. His current research interests are electrified and alternative fuel driven automobiles, driver assistance systems, vehicle dynamics and cable driven manipulators.

In 2015, he was awarded Dr. h.c. by the University of Miskolc, Hungary. Along with his research activities he is director and partner of several companies in the field of research and post graduated education.

Sustainable Development is the only path to achieve the green economy

Eng. Ahmed Abou Elseoud

Sustainable development is the management of renewable resources for the good of the entire human and natural community. Built into this concept is an awareness of the animal and plant life of the surrounding environment .The goal of sustainable development is to provide resources for the use of present populations without compromising the availability of those resources for future generations, and without causing environmental damage that challenges the survival of natural ecosystems. Consequently, sustainable economies cannot be based on the use of non-renewable resources. Ultimately, sustainable economies must be supported by the use of renewable resources such as biological productivity, and solar, wind, geothermal, and biomass energy sources. However, even renewable resources may be subjected to overexploitation and other types of environmental degradation. Central to the notion of sustainable development is the requirement that renewable resources are utilized in ways that do not diminish their capacity for renewal, so that they will always be present to sustain future generations of humans. On the other hand, Egypt welcomes the concept of the green economy to achieve sustainable development ,within the framework of respect for national priorities of each country, in order to achieve more decent work opportunities, and developments continued, and use environmental resources. Egypt have passed already in the implementation of a number of pilot projects in this regard, and look forward to witnessing the next stage for more cooperation with development. The energy is the main driver of economic and social development with the necessity to development of primary energy resources and the proper management and use of the most important policies and development strategies Egypt depends in achieving economic development and technological several sources of energy available to a power and petroleum and natural gas, but that recently Egypt has seen a severe lack of energy due to the following reasons Increased energy consumption rate - Lower crude oil and gas production rates in the country - Some electricity production plants with low efficiency - increasing proportion of commercial waste- Slow expansion of the use of alternative energy .In this sense the Ministry of Environment has searched for alternative sources of energy assessing its environmental impact and its economic and social impact at the same time and take measures and actions that would raise sustainable proportion of renewable energy in the Egyptian energy mix and working to reduce the pressures of climate change where can these measures can contribute to maximize the utilization of alternative energy resources and traditional such as the use of solid waste as well as alternative fuels and use them as a form of alternative energy.

About Eng. Ahmed Abou Elseoud

Currently the Chief Executive Officer, Egyptian Environmental Affairs Agency, Ministry of Environment. He has over 29 years of experience in different aspects and phases of water environmental management. He also has a significant expertise in computer modelling, management information systems, decision support systems and environmental quality monitoring and analysis including oversight of biomonitoring and environmental flow monitoring to EU Water Framework Directives, in Egypt, Armenia, Azerbaijan and Georgia. Eng Abou Elseoud has served as Water Resources Planner in the Egyptian Ministry of Water Resources and Irrigation for 15 years and moved to the Ministry of Environment where promoted to be the First Deputy Secretary Head of the Central Department for Environmental Quality in the Egyptian Ministry of Environment. He is a member of the Management Board of the Egyptian Electricity Holding Company, Cairo, charged with reviewing annual strategic planning, investment project and tariff structures for electricity in Egypt.

Modeling and Simulation of a Wind Turbine Driven Induction Generator Using Bond Graph

A. Ramdane *, A. Lachouri *, M. Krikeb *
*Team Leader in Automatic Laboratory, Electrical Engineering Department, Faculty of Technology,
University of 20 August 1955, Skikda. 21000, Algeria, ID, 83844-1133, USA.,
E-mail: Adlene_soft2005@yahoo.fr, alachouri@yahoo.fr, krikeb@yahoo.fr

***Abstract* -** This paper deals with the modelling and simulation of wind turbine driven by induction generator. Usually in mechatronic systems, several types of energy are involved. By its nature of a power conserving description of a system, the Bond-Graph method is especially practical when several physical domains have to be modeled within a system simultaneously. This is certainly the case in wind turbine systems where mechanical and electrical systems in several combinations are present. This work presents an implementation of the wind turbine model in bond graph approach. Simulation results are carried out by means of simulation in 20-sim software environment.

***Keywords* -** wind turbine, modelling, bond graph, induction generator.

I. INTRODUCTION

Energy consumption has increased considerably in recent years with the technology evolution. This has increased the demand for fossil fuels and has made firstly, electrical energy more expensive and secondly, the fossil fuels have a several disasters on the environment protection by the emissions of greenhouse gases and undesired particles into the atmosphere. Because of such reasons, it is necessary to focus on other forms of energy production to meet the growing needs of today's world. Furthermore, the wind energy, being one as an efficient source of alternative and cleanest sources of electricity, has emerged as one of the most preferred sources for electricity generation.

The wind energy is the kinetic energy of the flowing air mass per unit time. Therefore, when performing wind power integrated network planning or analysis of the operation, the engineers have put a lot of effort in modelling the wind rather than focusing on the problem itself. Thus, a wind model compatible with the analytical tools of commercial power system is in imminent need.
In Electromechanical Engineering, the global analysis of systems is difficult because of their heterogeneity and their multi-domains nature. Nevertheless, this system approach is essential because it underlines couplings between elements of different physical fields. To facilitate this analysis, the unified formalism Bond Graph is used. This modelling method illustrates the energetic transfers in the system. Moreover, this methodology offers interesting solutions in terms of system analysis.

Much research has been done on the modelling and control of wind turbines [2], [4], [6] and [7]. Most of this research has been done using simple wind mechanical and aerodynamic models that overlook a number of important features. Research on wind turbines based on more sophisticated mechanical and aerodynamic models was made only with relatively simple models of electric generator, its controllers, and model of the power system. This is because most researchers who have studied the wind power, they are focusing on aspects either electrical or mechanical part, without paying attention to the operation of the complete electromechanical system. There are many types of WT models, ranging from single mass, one state model to multiple mass models. In a simulation point of view, it is desirable that the model is as simple as possible and can capture as much of the dynamics that appear in reality.

In this context, our study is interested in the wind turbine system. This document is based on modelling and simulation method with Bond Graph (BG) applied to the wind turbine driven by generator induction. This method becomes a powerful tool when the complex interaction of subsystems of different types should be evaluated. The paper is organised as follows: The section 2 gives a brief introduction on bond graph methodology then, on finds in section 3 a modelling of different parts of wind turbine system and their bond graph in 20-sim software is presented. In section 4 is illustrated the simulation results and theirs discuss. A conclusion is given at the end of this paper.

II. BOND GRAPH

A. Bond Graph methodology

The methodology of the bond graph modelling is based on the characterization of power exchange phenomena within a system. The idea of the bond graph modelling is the representation of dissipated power as the product flow and effort to bind the various junctions to reproduce the system. The bond graph is a powerful tool in modelling systems; especially in cases where subsystems of different physical character (mechanical, electrical, thermal, hydraulic …) are interact. The exchange of energy between the subsystems of a more complex system in bond graph modelling is of an essential significance. Bond graph is therefore a directed graph whose nodes represent subsystems and arrows - the transfer of energy between the subsystems.

B. Bond Graph Elements

In BG modelling, there are a total of nine different elements. We will first present the basic elements of BG and introduce the causality assignments.

Source element: there are two type of 1-ports source: the effort source and the flow source. In each case, an effort or flow is assumed to be maintained constant independent of the power supplied; the constitutive relation and causality is showing in Fig.1.

Fig .1. Sources elements

Resistive element: is an element in which the effort and flow variables at the single port are related by a static function Fig2.

Inertia element: the inertia port corresponds to the electrical inductors, the momentum p is related the flow f. There are two choices for the causality assignment for the I-element Fig2.

Compliance element: is an element that relates effort e and displacement q. the power flows into the port and a sign convention similar to that used for the resistor is adopted Fig.2.

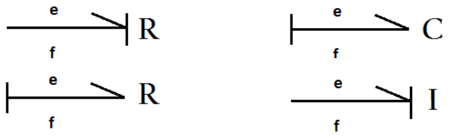

Fig .2. Resistance, Inertia and compliance elements

Transformer and gyrator: the transformer and gyrator can work in two ways; transformer transforms a flow to another flow or an effort to another effort. The gyrator transforms a flow into an effort or transforms the effort into a flow.

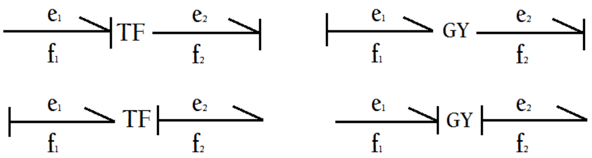

Fig .3. Transformer and Gyrator elements

Junctions: there are two different types of junctions that connect the different parts in BG, the 0-junction and 1-junction. Junctions are power conserving at each instant and the power transport of all bonds add up to zero at all times. The junction elements represent the two types of connections, which, in electrical terms, are called the series, and parallel connections

III. MODEL DESCRIPTION

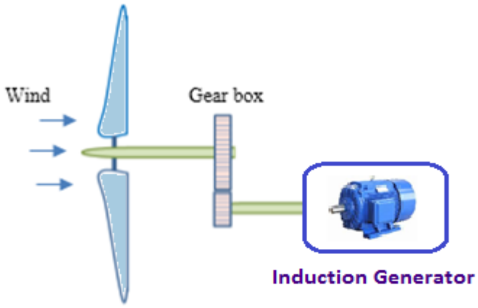

Fig .4. Wind turbine model description

In this section, the dynamic simulation model is described for the proposed wind turbine energy conversion. The block diagram of the integrated overall system is shown in Fig.4. Afterwards, each sub-model of the wind turbine is presented and combined to obtain a complete model of the wind turbine.

The all parts of system modelling in 20-sim software is showing in Fig.5.

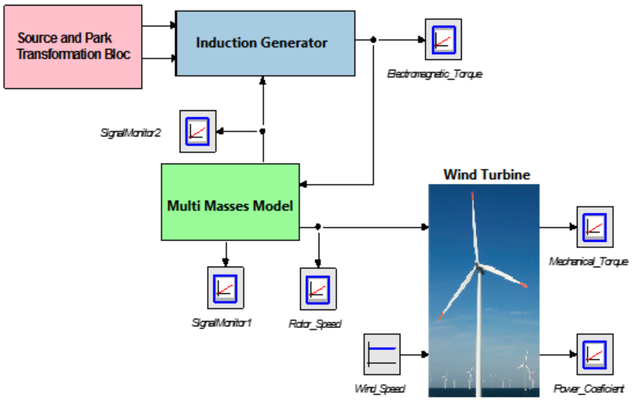

Fig .5. System Parts modelling in 20-sim software

A. *Aerodynamic Model*

Wind turbine electrical generation systems power comes from the kinetic energy of the wind. Thus, it can be expressed as the kinetic power available in the stream of air multiplied by a Cp factor called power coefficient or Betz's factor. The Cp Mainly depends on the relation between the average speed of the air across the area covered by the wind wheel and its angular speed and geometric characteristics of the turbine. The power extracted by the wind turbine has the following expressions [2]:.

$$P_w = \frac{1}{2}.\rho.A.C_p.{V_W}^3 \qquad (1)$$

$$A = \pi.R^3 \qquad (2)$$

Where P_w is the air stream kinetic power, ρ the air density assumed to be constant, A is the surface covered by the wind wheel and V_W the average wind speed. The power that wind turbine can catch from wind is:

$$T_W = \frac{P_W}{\Omega} \qquad (3)$$

There have been different approaches to model the power coefficient ranging from considering it to be constant for steady state and small signal response simulations to using lookup tables with measured data. Another common approach is to use an analytic expression [2]:

$$C_p = 0.22\left(\frac{116}{\lambda'} - 0.4\beta - 5\right)e^{\frac{-12.5}{\lambda'}} \qquad (4)$$

With:

$$\frac{1}{\lambda'} = \frac{1}{\lambda+0.08\beta} - \frac{0.035}{\beta^3+1} \qquad (5)$$

Where λ is so called tip-speed ration and it is defined as $\lambda = \frac{\omega R}{V_w}$ *(6)*

and β is the pitch angle.

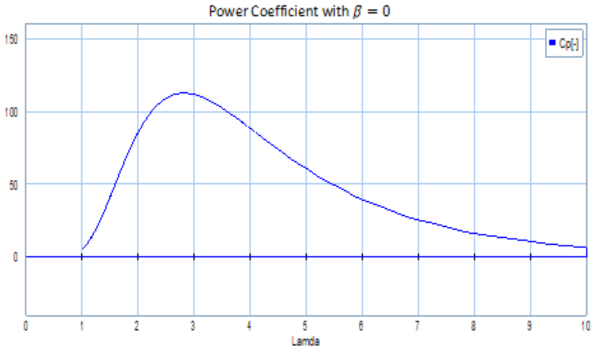

Fig .6 Power Coefficient of wind turbine

In general the C_p coefficient is represented by the Graph which depends on the tip-speed ratio λ and the pitch angle β.

The bond graph of aero-dynamical part of wind turbine model implemented in 20-sim software from [4] is show in Fig.4.

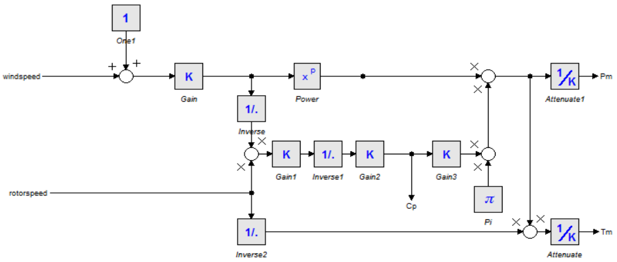

Fig .7 The bloc diagram Model of Aero-dynamical part of wind turbine model in 20-sim Software

B. *Mechanical Part*

The mechanical part of the wind turbine system includes all the mechanical elements of Systems (blades, lock rotor, shafts, Speed Multiplier (gear box)

... etc.).This multiplier is modelled mathematically in [3] for the following equations:

$$\boldsymbol{C_r} = \frac{\boldsymbol{T_m}}{\boldsymbol{G}} \tag{7}$$

$$\boldsymbol{\Omega_{turbine}} = \frac{\boldsymbol{\Omega_{mec}}}{\boldsymbol{G}} \tag{8}$$

G: The speed multiplier gain

$$\boldsymbol{J} = \frac{\boldsymbol{J_{turbine}}}{\boldsymbol{G^2}} + \boldsymbol{J_r} \tag{9}$$

The fundamental equation of dynamics used to determine the evolution of the mechanical speed from the total mechanical torque ($\boldsymbol{C_{mec}}$) applied to the rotor:

$$\boldsymbol{J}\,\frac{\boldsymbol{d\Omega_{mec}}}{\boldsymbol{dt}} = \boldsymbol{C_{mec}} \tag{10}$$

J The total inertia appears on the generator rotor. The mechanical torque depends on the electromagnetic torque ($\boldsymbol{C_{em}}$) produced by the generator, the torque of viscous friction ($\boldsymbol{C_{vis}}$) and load torque ($\boldsymbol{C_r}$).

$$\boldsymbol{C_{mec}} = \boldsymbol{C_r} - \boldsymbol{C_{em}} - \boldsymbol{C_{vis}} \tag{11}$$

The viscous torque is modelled by.

$$\boldsymbol{C_{vis}} = \boldsymbol{f}.\boldsymbol{\Omega_{mec}} \tag{12}$$

$\boldsymbol{f}$: Is the viscous friction coefficient.

C. Three Masses Model

The equivalent model of a wind turbine drive train is presented in Fig 6. The masses correspond to a large mass of the wind turbine rotor, masses for the gearbox wheels and a mass for generator respectively.

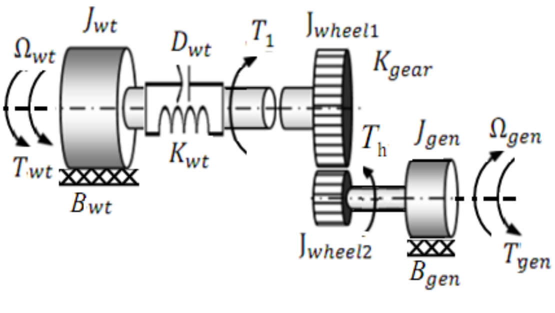

Fig 6. Three-mass model of a wind turbine drive train.

The inertia of the low-speed shaft also includes the inertia of the rotor, while the friction component includes bearing frictions. The dynamics of the low-speed shaft is:

$$\boldsymbol{T_{wt}} - \boldsymbol{T_1} - \boldsymbol{B_{wt}\Omega_{wt}} = \boldsymbol{J_{wt}}\frac{\boldsymbol{d\Omega_{wt}}}{\boldsymbol{dt}} \tag{13}$$

Where:

B_{wt} Is the viscous friction of the low-speed shaft [Nm/(rad/s)],
J_{wt} Is the moment of inertia of the low-speed shaft [Kgm2],
T_{wt} Is the torque acting on the low-speed shaft [Nm],
θ_{wt} Is the angle of the low-speed shaft [rad],

The inertia of the high-speed shaft also includes the inertia of the gearbox and the generator rotor. The friction coefficient covers bearing and gear frictions. The dynamics of the high-speed shaft is:

$$\boldsymbol{T_h} - \boldsymbol{T_{gen}} - \boldsymbol{B_{gen}\Omega_{gen}} = \boldsymbol{J_{gen}}\frac{\boldsymbol{d\Omega_{gen}}}{\boldsymbol{dt}} \tag{14}$$

Where:
B_{gen}: The viscous friction of the high-speed shaft [Nm/(rad/s)];
J_{gen} : The inertia moment of the high-speed shaft [Kgm^2];
T_{gen} : The generator torque [Nm];
T_h : The torque acting on the high-speed shaft [Nm];
θ_{gen} : The angle of the high-speed shaft [rad];

The remaining part of the gearbox modeling is to apply a gear ratio, as defined below.

$$\boldsymbol{T_h} = \frac{\boldsymbol{T_1}}{\boldsymbol{K_{gear}}} \tag{15}$$

K_{gear} is the drive train gear ratio.

The torsion of the drive train is modelled using a torsion spring and a friction coefficient model, described according to:

$$\boldsymbol{T_1} = \boldsymbol{K_{wt}\theta_\Delta} + \boldsymbol{D_{wt}\dot{\theta}_\Delta} \tag{16}$$

$$\boldsymbol{\theta_\Delta} = \boldsymbol{\theta_r} - \frac{\boldsymbol{\theta_{gen}}}{\boldsymbol{K_{gear}}} \tag{17}$$

Where:
D_{wt} is the viscous friction of the low-speed shaft [Nm/(rad/s)]
K_{wt} is the torsion stiffness of the drive train [Nm/rad]
$\theta_\Delta$is the torsion angle of the drive train [rad]

$$\boldsymbol{T_1(t)} = \boldsymbol{K_{wt}}\left(\boldsymbol{\theta_r} - \frac{\boldsymbol{\theta_{gen}}}{\boldsymbol{K_{gear}}}\right) + \boldsymbol{D_{wt}}\left(\boldsymbol{\Omega_{wt}} - \frac{\boldsymbol{\Omega_{gen}}}{\boldsymbol{K_{gear}}}\right) \tag{18}$$

After simplification and substituting equations obtains

$$\begin{cases} \boldsymbol{J_{wt}\frac{d\Omega_{wt}}{dt} = T_{wt} - K_{wt}\left(\theta_r - \frac{\theta_{gen}}{K_{gear}}\right) - (D_{wt} + B_{wt})\Omega_{wt}} \\ \qquad \boldsymbol{+ \frac{D_{wt}}{K_{gear}}\Omega_{gen}[Nm]} \\ \boldsymbol{J_{gen}\frac{d\Omega_{gen}}{dt} = \frac{K_{wt}}{K_{gear}}\left(\theta_r - \frac{\theta_{gen}}{K_{gear}}\right) + \frac{D_{wt}}{K_{gear}}\Omega_{wt}} \\ \qquad \boldsymbol{- \left(\frac{D_{wt}}{K_{gear}} + B_{gen}\right)\Omega_{gen} - T_{gen}[Nm]} \\ \boldsymbol{\dot{\theta}_\Delta = \dot{\theta}_{wt} - \frac{\dot{\theta}_{gen}}{K_{gear}}[rad/s]} \end{cases} \tag{19}$$

Three first order differential equations have been derived in this section in order to describe the behavior of the drive train. In the next section, the effect on the tower from the aerodynamic thrust is considered.

Bond graph bloc diagram model of three masses system is showing in Fig.8.

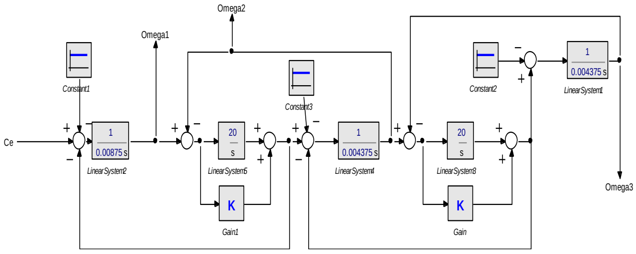

Fig 8. Multi masses system model

D. *Electrical Part*

The generator used for the wind system is an asynchronous squirrel-cage generator whose parameters are quoted in table1. The model of the asynchronous machine is deduced from the two-phase machine by supposing that the variables are expressed in a reference frame x-y turning at the speed of the electric field. The results obtained by simulation illustrate the behaviour of this generator and give the par values of operation.

The induction machine equations are [2]:

$$\begin{cases} U_{sx} = R_s I_{sx} + S\Psi_{SX} - \omega_S.\Psi_{SY} \\ U_{sy} = R_s I_{sy} + S\Psi_{Sy} - \omega_S.\Psi_{Sx} \\ 0 = R_r I_{rx} + S\Psi_{rx} - (\omega_S - \omega_r)\Psi_{ry} \\ 0 = R_r I_{ry} + S\Psi_{ry} - (\omega_S - \omega_r)\Psi_{rx} \\ Ce = P.L_{sr}\left(I_{sy}.I_{rx} - I_{sx}.I_{ry}\right) \\ \Psi_S = \mathrm{L_s}.\mathrm{I_s} + \mathrm{L_{sr}}.\mathrm{I_r} \\ \Psi_r = \mathrm{L_r}.\mathrm{I_r} + \mathrm{L_{sr}}.\mathrm{I_s} \end{cases} \tag{20}$$

This system can be presented as follows:

$$\begin{cases} S\Psi_{sx} = U_{sx} - R_s.I_{sx} + \omega_s.\Psi_{sy} \\ S\Psi_{sy} = U_{sy} - R_s.I_{sy} + \omega_s.\Psi_{sx} \\ S\Psi_{rx} = R_r.I_{rx} + (\omega_S - \omega_r)\Psi_{ry} \\ S\Psi_{ry} = R_r.I_{ry} + (\omega_S - \omega_r)\Psi_{rx} \\ Ce = P.L_{sr}\left(I_{sy}.I_{rx} - I_{sx}.I_{ry}\right) \\ I_s = \frac{\mathrm{L_r}.\Psi_s + \mathrm{L_{sr}}.\Psi_r}{\mathrm{L_s}.\mathrm{L_r} - \mathrm{L_{sr}}^2} \\ I_r = \frac{\mathrm{L_s}.\Psi_r + \mathrm{L_{sr}}.\Psi_s}{\mathrm{L_s}.\mathrm{L_r} - \mathrm{L_{sr}}^2} \end{cases} \tag{21}$$

U_{SX}, U_{sy} : The stator voltage Components expressed in x-y reference.

I_{SX}, I_{sy} : The stator current Components expressed in x-y reference.

R_S : Stator resistance;

R_r : Rotor resistance;

L_S : Stator Inductance;

L_r : Rotor Induction;

L_{Sr} : Mutual inductance;

P : Number of pole pairs;

C_e : Electromechanical torque;

ω_S : Speed of the electric field;

ω_r : Electric rotor speed;

The bond graph of induction machine in 20-sim software using library developed in [5] is showing in Fig.9.

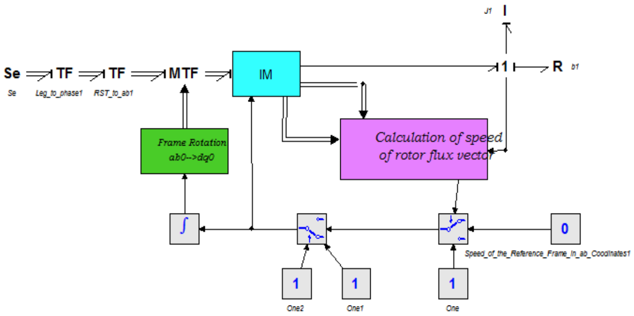

Fig 9. Induction Generator bond graph model

IV. SIMULATION RESULTS

Simulation step is done on a specific bond graph software 20-sim, which is an object oriented hierarchical modelling software. It allows users to create models using bond graph, block-diagram and equation models. A list of numerical values of wind turbine system parameters used in this simulation is presented in Table-1.

Table 1. Model Parameters

Nominal Power	Pn=180KW
Rotor Diameter	D=23.2m
Rotor Speed	Ω=42tr/min
Multiplier Coefficient	23.75
Number of Blades	3
Air Density	ρ=1Kg/m^3
Turbine Moment Inertia	J_T=102,8Kgm^2
Generator Moment Inertia	J_G=4,5Kgm^2
Rigidity Coefficient	K_{12}=2700Nm/rad
Damping Coefficient	B_{12}=0.1Nms/rad
Number of Pairs	P=3
Stator Resistance	Rs=0.0092Ω
Rotor Resistance	Rr=0.0061Ω
Stator Mutual Inductance	Lls=186µH (Ls= Lls+ Lm)
Rotor Mutual Inductance	Llr=427µH (Lr= Llr+ Lm)
Magnetizing Inductance	Lm=6.7mH (Lsr= Lm)

The Fig.5 shows all parts of system modelling implemented in 20-sim software. The Fig.6 presents the Power Coefficient C_p evolution function of tip-speed ration (λ). Through this figure, we can easily see that the evolution of the C_p retrieve its maximum at the $\lambda_{op} = 3$. The Fig.7 illustrated a bond graph bloc diagram Model of Aero-dynamical part of wind turbine and Fig.8 presents a Bond graph of Multi mass model under 20-sim software. The Fig.9 depicts Induction Generator bond graph model. The Fig.10 and Fig.11 show the mechanical power and torque curves respectively of the wind turbine. They occur the maximum point at the $\lambda_{op} = 3$. The Fig.12 shows the power coefficient with blade pitch β and its maximum value at $\lambda_{op} = 3$. With regard to the instantaneous torque (Fig.13), we can indicate the presence of oscillations in magnitude for a very short time at start up, and then these oscillations are cleared. Figures (Fig.14-16) show the curves velocities of multi-mass model. They have strong oscillations during the transient regime during 0.02s, and converse to its nominal speed at 157rad /s.

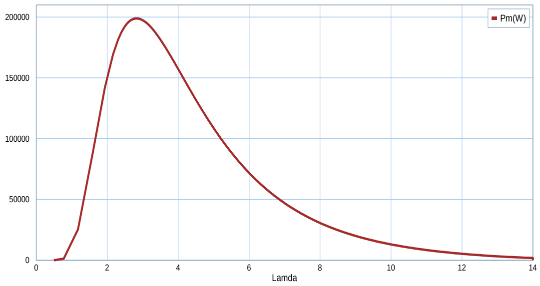

Fig 10. Mechanical Power in 20-sim software

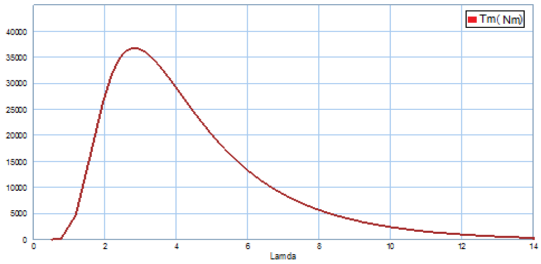

Fig 11. Mechanical Torque In 20-sim Software

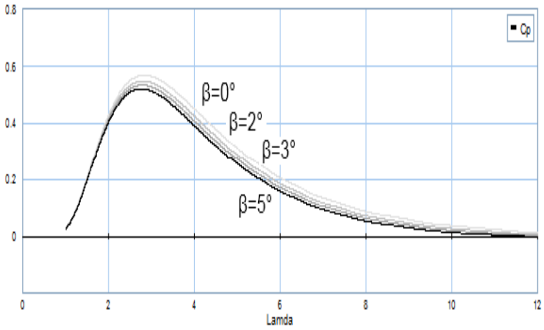

Fig 12. Power Coefficient

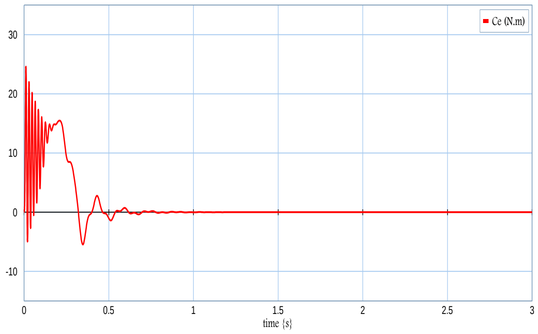

Fig 13. Torque characteristic

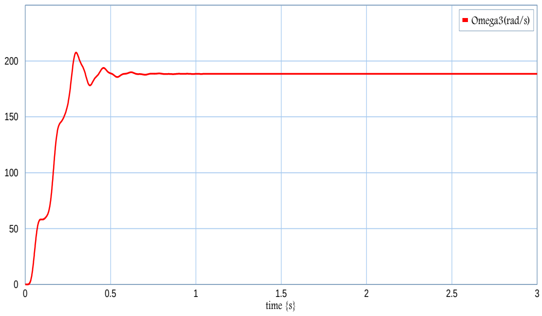

Fig 14. First mass Speed

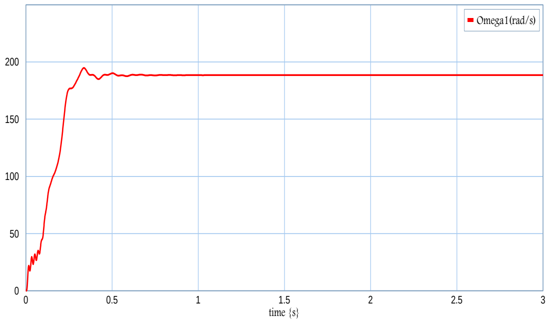

Fig 15. Second mass Speed

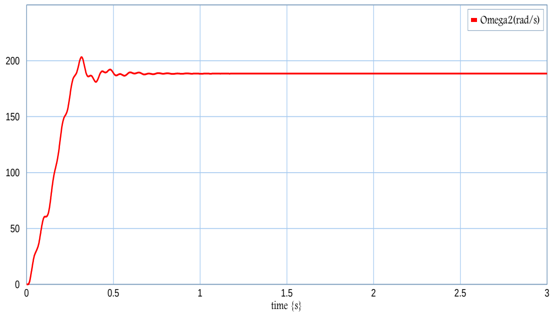

Fig 16. Third mass Speed

V. CONCLUSION

In this paper, a power conversion system was studied with a “system viewpoint methodology” by using a Bond Graph technique. However, the different fields of energy conversion, the nonlinearity and the different dynamics of the system involve the use of a global unified formalism for studying the global system. The software ‘‘20-sim’’ permit to implemented the bond graph system model’s. The simulation results from this approach confirm one of the benefits of BG as a generally usable approach to modelling mechatronic systems and offers interesting solutions in terms of system diagnosis and analysis.

REFERENCES

[1] A.Djeziri, R. Merzouki, B. Ould Bouamama, G. Dauphin-Tanguy. ‘Bond Graph Model Based For Robust Fault Diagnosis’ IEEE, 2007, 1-4244-0989-6/07.

[2] Sanae Rechka, GillesRoy, Sébastien Dennetiere et Jean Mahseredian,’Modélisation de systèmes électromécanique multi-masses à base de machines asynchrones, à l’aide des outils MATLAB et EMTP,avec Application aux éoliennes ,juillet 2004.

[3] F. Kendouli, K. Nabti, K. Abed et H. Benalla,’ Modélisation, simulation et contrôle d’une turbine éolienne à vitesse variable basée sur la génératrice asynchrone à double alimentation ‘ Revue des Energies Renouvelables Vol. 14 N°1 (2011) 109 – 120.

[4] J.G. Slootweg, S.W.H.H Polinder and W.L. king, ‘General Model for representing variable speed wind turbines in power systems dynamics simulations’, IEEE Transaction on power system, Vol 18, No. 1, February 2003, pp. 144-151.

[5] Sergio Junco, Gonzalo Dieguez, Facundo Ramirez, ‘ une librairie 20-sin pour la simulation basée bond graphs de système de commande des machines électrique ‘cifa_2008_T18-I-07-0338.

[6] Lucian Mihet-Popa, Frede Blaabjerg, Ion Boldea,’ Wind Turbine Generator Modeling and Simulation Where Rotational Speed is the Controlled Variable’,IEEE Transactions On Industry Applications, Vol. 40, No. 1, January/February 2004.

[7] B. ChittiBabu , K.B. Mohanty,’ Doubly-Fed Induction Generator for Variable Speed Wind Energy Conversion Systems- Modeling & Simulation', International Journal of Computer and Electrical Engineering, Vol. 2, No. 1, February, 2010 ,1793-8163.

[8] Tore Bakka and Hamid Reza Karimi,’ Wind Turbine Modeling Using The Bond Graph’, 2011 IEEE International Symposium on Computer-Aided Control System Design (CACSD),Part of 2011 IEEE Multi-Conference on Systems and Control Denver, CO, USA. September 28-30, 2011.

Implications of Human Induced Changes on the Distribution of Important Plant Species in the Northwestern Coastal Desert of Egypt

Marwa Waseem Halmy [1]*, Paul E. Gessler [2], Selim Z. Heneidy [1]
[1] Department of Environmental Sciences, Faculty of Science, Alexandria University, Alexandria, Egypt,
[2] Department of Forest, Rangeland and Fire Sciences, P.O. Box: 441133, University of Idaho, Moscow, ID, 83844-1133, USA.,
*Corresponding author, Email: marwa.w.halmy@alexu.edu.eg
Address: Department of Environmental Sciences, Faculty of Science, P.O. Box: 21511, Alexandria, Egypt.

***Abstract* -** The application of species distribution modeling in deserts is a useful tool for mapping species and assessing the impact of human induced changes on individual species. Such applications are still rare, and this may be attributed to the fact that much of the arid lands and deserts around the world are located in inaccessible areas. Few studies have conducted spatially explicit modeling of plant species distribution in Egypt. The random forests modeling approach was applied to climatic and land-surface parameters to predict the distribution of ten important plant species in an arid landscape in the northwestern coastal desert of Egypt. The impact of changes in land use and climate on the distribution of the plant species was assessed. The results indicate that the changes in land use in the area have resulted in habitat loss for all the modeled species. Projected future changes in land use reveal that all the modeled species will continue to suffer habitat loss.

The projected impact of modeled climate scenarios (A1B, A2A and B2A) on the distribution of the modeled species by 2040 is varied. Some of the species were projected to be adversely affected by the changes in climate, while other species are expected to benefit from these changes. The combined impact of the changes in land use and climate poses serious threats to most of the modeled species. The study found that all the species are expected to suffer loss in habitat, except Gymnocarpos decanderus. The study highlighted the importance of assessing the impact of land use/climate change scenarios on other species of restricted distribution in the area and can help shape policy and mitigation measures directed towards biodiversity conservation in Egypt.

***Keywords* -** climate change - land use change - random forests - species conservation importance (SCI) index - species distribution models (SDMs).

I. INTRODUCTION

A. Species Distribution Models (SDMs)

Species distribution models (SDMs) were founded in ecology and natural history based on gradient modeling and niche theory [1], [2], [3]. Habitat or species distribution models (SDM) are defined as models that 'statistically relate the geographical distribution of species or communities to their present environment' [4]. Species distribution models (SDM) are also known as: bioclimatic models; climate envelopes; ecological niche models (ENMs); habitat models; resource selection functions (RSFs); and range maps [2]. The premise of these models is that environmental factors control the distribution of species and consequently communities [1], [4], [5].

Prediction of species distribution started early on by descriptive studies conducted by ecologists interested in understanding the relationship between patterns of species in relation to geographical settings and environmental gradients [2]. Later the evolution in ecology and other related fields coupled by the emergence of numerical analysis and quantitative approaches has greatly influenced species distribution modeling. Quantitative approaches of species distribution modeling developed as a result of convergence of two lines of research trends in ecology and geography. The first line started in ecology as field-based research that studied species-habitat relationships. These studies later adopted quantitative approaches by applying statistical analysis techniques (e.g. linear multiple regression techniques), then the advanced regression techniques (e.g. Generalized Liner Models (GLMs) and boosted regression techniques) were developed to overcome limitations of the linear paradigm. The second line emerged in geography, and specifically in physical geography, through the advancement in geographic information systems and remote sensing techniques [2]. The integration of GIS and remote sensing has allowed the development of methods for interpolation of global climate and modeling global surface elevation, in addition to provision of spectral data that were employed in species prediction models. The development of the field of species distribution modeling and mapping has been driven by the need to map vegetation patterns over large areas for resource management and conservation planning, and to predict the effects of environmental changes on vegetation distribution [1], [5].

A suite of statistical and machine-learning techniques has been developed for conducting SDMs [6]. Although many approaches are used for the species distribution modeling, no rules exist to provide guidelines on the best modeling approach to use [3]. It is also likely that some approaches may be better for prediction of one species over another. This is related to many factors that include: the nature of the data used (quantity & quality); the nature of the predicator variables used; the spatial scale used (resolution and the extent); and the relevance of the environmental predicators used to the ecological characteristics of the species being predicted [4], [7], [8], [9], [10].

B. Applications of SDMs for Studying Global Changes

The use and application of SDMs for different purposes is growing rapidly [11], because SDMs provide useful tools for understanding the gaps in knowledge of species distribution. More recently they have been used to assess potential impacts of changes in environmental and climatic conditions on the distribution of species [12], [4], [3], [13]. In most cases these studies deal with different land use/land cover and climatic scenarios.

The study by Sala and his colleagues [14] is one of the first studies that provided projection of changes in biodiversity at the global scale under different scenarios of climate and land use change by 2100. The study provided scenarios of change in the ten widely known terrestrial biomes plus the fresh water aquatic ecosystems. They based their scenarios on how the change in some drivers (for example; climate, vegetation, land use, and levels of carbon dioxide) will trigger changes in biodiversity.

Over the last three decades, numbers of General Circulation Models (GCM’s) have been developed. The Data Distribution Center (DDC) of the IPCC distributes a number of datasets, derived from various general circulation models (GCMs). These models are available on the web at: http://www.ipcc-data.org/. Due to the coarse resolution of these data, they are mostly used to assess the potential impact of change in climate at a broad scale. This coarse resolution does not suit applications aiming at assessing the climate change impact on agriculture and biodiversity at finer scales [15], [16]. Therefore, many attempts have been made for downscaling and disaggregating GCM outputs (for example; [17], [16]). Spatial disaggregation based on WorldClim data [15] as baseline climate was applied to 24 different GCMs used in the IPCC4th assessment report for different emission scenarios and for seven different 30-year running mean periods [16]. The data are freely available through the CGIAR Research Program on Climate Change, Agriculture and Food Security (CCAFS) web: http://www.ccafs-climate.org/data/. The data have been used to assess the response of different species to the simulated changes in climate (for example, [18], [19], [20]).

Arid lands in general and deserts specifically, are poorly studied areas with regard to the assessment of their biodiversity and understanding the distribution of species in their vicinity [21]. This is likely related to the harsh nature of these areas and the inaccessibility of parts of the desert areas. The few studies that used species distribution modeling techniques in desert ecosystems were successful in providing tools for modeling the distribution patterns of species. Yet SDM approaches have rarely been used for addressing the influence of environmental changes (climate, land use change or any other disturbances) on the distribution of species in arid lands. This may be because arid lands are some of the most poorly studied areas in the world. Species distribution modeling techniques were used in the current study to project the impact of environmental changes on the distribution of ten important plant species in the northwestern coastal desert of Egypt. This region has experienced rapid change in land use/land cover recently due to coastal development projects. Species distribution modeling techniques and available environmental predictors (bioclimatic and land-surface parameters) were used here to: 1) predict the potential distribution of ten important plant species; 2) study the effect of land use change on distribution of the modeled species; and 3) project the potential changes in distribution of the species under different climate/land use scenarios.

II. MATERIALS AND METHODS

A. Study Area

The study area is part of the northwestern coastal desert of Egypt. It extends for 40 km from El-hamam town to westward to El-Alamein town and from the Mediterranean coast southward to Moghra Oasis (Figure 1), occupying an area of about 2800 km2 located between 30° 10' to 30° 55' and N 28° 55' to 29° 25' E.

The area has a short rainy season, which occurs mostly during winter from November to April but may extend to May. Little precipitation occurs during the rest of the year [22], [23]. The mean annual precipitation ranges from100 to 150 mm/year, thus the area considered arid (rainfall zones of 0-300 mm) [24]. The climatic records [25] indicate that the total monthly evapotranspiration in the coastal area exceeds the total annual precipitation. This reflects the arid conditions and the water deficiencies that prevail in the area. A north-south climatic gradient was noticed in this region, with an increase in environmental aridity and 'thermal continentality' towards the South [26]. The vegetation of the region is dominated by dwarf shrubs less than one meter [24]. The agricultural activities in the northern part have resulted in changes throughout the area that might have impacted species distributions.

The Omayed Biosphere Reserve (OBR) a.k.a. ElOmayed Protected Area (OPA) is located in the northern part of the study area (Figure 1). The protected area is considered as one of the largest terrestrial protected area in Egypt [27].

B. Data Collection

Field visits were conducted to survey the plant species in the area, where more than 800 plots were selected randomly in order to account for the major physiographic variation in the study area. Plant species were recorded and identified according to "Students' Flora of Egypt" by Täckholm [28] and nomenclature of the species was updated following "Flora of Egypt" by Boulos [28], [29], [30], [31], [32] and the Latin names of the species were updated following the "Flora of Egypt: Checklist" by Boulos [33]. Species distribution modeling could be developed based on the presence-only data or presence-absence data [35]. In the current study, both presence and absence data were employed in modeling.

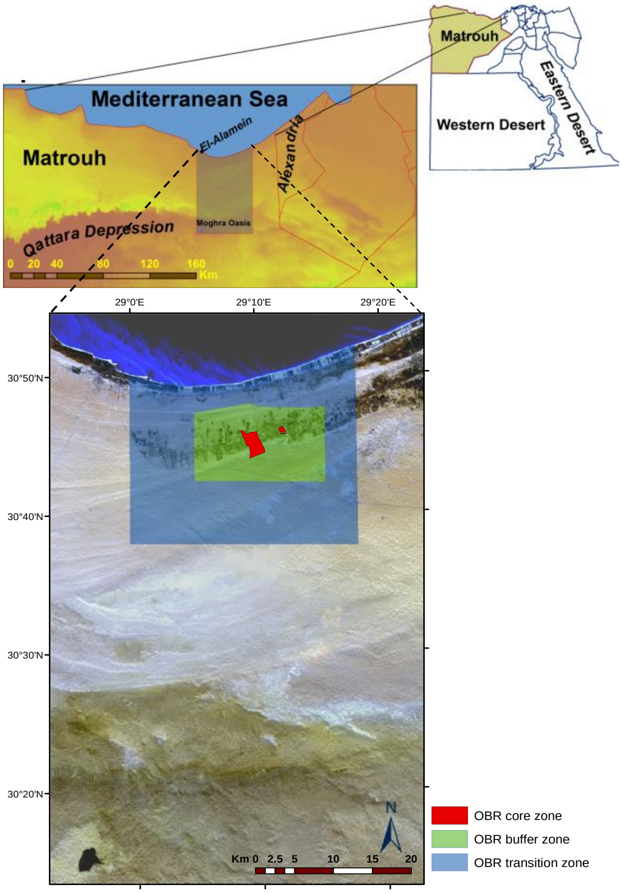

Fig .1. Location of the studied area: a) Egyptian governorates' administrative boundaries; b) the northwestern coastal desert showing location of the study area northeast of Qattara Depression; and c) the study area as shown through part of Landsat Thematic Mapper 2011 image. The location of Omayed Biosphere Reserve (OBR) is highlighted, core zones in red, buffer zone in green and transition zone in blue (After [34]).

C. Predictors

The accuracy and the predictive power of any habitat distribution model depend on the quality and the accuracy of the field data employed and the choice of the environmental variables used to build the model [40]. In the current study, a number of land-surface parameters and bioclimatic variables were used to build the plant species distribution models (Table 1). Ecological land-surface parameters derived from digital elevation models (DEMs) are considered important for mapping vegetation, especially if combined with other parameters including spectral indices derived from satellite imagery [41]. A digital elevation data SRTM V4.1 (Jarvis et al. 2008) were used for the derivation of land-surface parameters. The land-surface parameters employed in the study (Table 1) included slope; a terrain roughness index (TRI) that provides an quantification of the level of undulation and the complexity of the surface [42]; topographic wetness index (TWI) [43]; and a slope length and steepness (LS) factor. All the land-surface parameters were derived using the Automated System Geoscientific Analyses version 2.0.7 [44].

Climatic conditions are recognized as the most important environmental variables responsible for the patterns of species distribution at broad scales [45]. However, the availability of climatic data layers of appropriate resolution has been rare for researchers intending to do species distribution mapping, especially in understudied areas [3]. Recently, interpolated global climatic data layers that represent the previous and current climatic conditions were made available to the public (for example; WorldClim [15] and CliMond [46]). ‘WorldClim’ is available with global coverage at a spatial resolution of 1 km2 and can be downloaded from http://www.worldclim.org. The WorldClim data include monthly mean total precipitation and mean, minimum, and maximum temperature in addition to nineteen other bioclimatic variables. The current study used thirty environmental variables (Table 1) representing important factors for plant survival; including bioclimatic variables, topographic variables and light controlling factors. The incorporation of light controlling factors in modeling plant distribution was recommended, particularly in studies that involve assessment of the impact of climate change on plant distribution [47]. Solar insolation indices were derived from the digital elevation data and included in the analysis. The distance to the coast was also included as a factor in modeling plant species distribution to account for maritime influences due to proximity to the Mediterranean Sea. All the layers representing the variables employed in the analysis were re-sampled to match the spatial resolution of the DEM used.

D. Modeling Approach

The data used in the current study were collected systematically using field surveys through which the presence/ absence observations were recorded for each species. Generalized linear models (GLMs) or ensembles of regression trees such as random forests (RF) or boosted regression trees, (BRT) are recommended in cases where presence/absence data are available [3], [48], [6]. The current study applied the machine learning ensemble method random forests (RF) to predict the distribution of the selected species using climatological and topographical factors. The collected presence/absence data were divided randomly to two sets; 70% for calibrating the models and 30% for testing and evaluating the models. All the analyses were conducted within the framework of the open source statistical computing environment of R 2.13.1 [49]. The ‘randomForest’ package [50] was used for carrying out the random forests analyses. Random forests analysis (RF) has been used in some studies for modeling species and predicting changes in species distribution under different climate scenarios [51], [52], [10], [53], [54]. It is one of the ‘ensemble modeling’ techniques that have recently been used successfully in ecological modeling [3]. It is composed of an ensemble of [55] classification and regression trees (CART) [56]. The RF approach has the advantage of being a non-parametric approach that can produce a highly accurate classification results and can process a larger number of independent variables [57]. It has been recommended for being robust to outliers and noise [57], [58], [59], [56], [60], [61].

In RF model, an ensemble of classification and regression tree (CART) models is created by training each model on a bootstrap sample of the original training data set. The output from each CART model is then subjected to a voting process whereby the most common vote is selected for producing the final results of a classification and the average of all the tree results is obtained in the case of performing regression. The size of the random forests model (i.e. the number of trees) and the number of variables to be used for splitting nodes at each tree in the random forests model need to be specified by the analyst depending on the study. The selection of these parameters is based on the combination that minimizes the out-of-bag error (oob). Out-of-bag error estimation is used as an assessment of the accuracy of the model. It is estimated by keeping out (out-of-bag) one third of each bootstrap replica generated from the original training data and using it to test the tree models. The use of oob error for evaluating the performance of the RF models is considered a robust unbiased method [57]. The optimum combination of the number of trees in the RF model and the number of variables to be used for splitting nodes was determined based on trials, which revealed that models with a size of 750 trees and four splitting variables at each node attained the lowest error rates. A general model for predicting each species was fit using all the variables, whereby an assessment of the importance of each variable in fitting the model was estimated. The percentage of increase in mean square error (MSE) was caused when a variable that is randomly permuted and introduced to the model was used as basis for selection of variables to create a reduced model for each species.

Table 1. Variables used in building the models of species distribution in the study area.

Variable	Abbreviation	Source
Annual mean temperature	Bio1	Baseline climate data [15] available from: http: //www.worldclim.org Predicted climate data [16] available from: http: //www.ccafs-climate.org/data/
Mean diurnal range (mean of monthly (max temp - min temp))	Bio2	
Isothermality (mean diurnal range/temperature annual range) (*100)	Bio3	
Temperature seasonality (standard deviation *100)	Bio4	
Max temperature of warmest month	Bio5	
Min temperature of coldest month	Bio6	
Temperature annual range (max of warmest month-min of coldest month)	Bio7	
Mean temperature of wettest quarter	Bio8	
Mean temperature of driest quarter	Bio9	
Mean temperature of warmest quarter	Bio10	
Mean temperature of coldest quarter	Bio11	
Annual precipitation	Bio12	
Precipitation of wettest month	Bio13	
Precipitation seasonality (coefficient of variation)	Bio15	
Precipitation of wettest quarter	Bio16	
Precipitation of coldest quarter	Bio19	
Aspect	Aspect	Derived from SRTM DEM [18] Available from: http: //srtm.csi.cgiar.org
Across-slope plan curvature	PlCurv	
Curvature [62]	Curv	
Diffusion insolation	DiffInsol	
Direct insolation	DirInsol	
Downslope profile curvature	PrCurv	
Direct/diffusion insolation ratio	DiffToDir	
Elevation	Elev	
LS factor	LS	
Proximity to sea	ProxtoSea	
Slope [62]	Slope	
Terrain roughness index according to [63]	TRI	
Topographic Wetness Index (TWI) [43]	TWI	
Total insolation	TotInsol	

E. Models Evaluation

The accuracy and credibility of habitat distribution models should be considered in the context of the intended applications [4]. Accuracy assessment and uncertainty about the data used in developing these models should be reflected in and accounted for by any further analysis that might use the products of these models [64]. An account of the most commonly used measures for accuracy assessment of the species distribution models can be found in [3], [11]. The most commonly used threshold-dependent measure for assessing accuracy of habitat distribution models is the Kappa statistic; however kappa has been criticized for producing a biased accuracy assessment. Allouche and colleagues [65] described the bias encountered when using Kappa statistic [66] and suggested using the true skill statistic (TSS) [67] as an alternative method for assessing the accuracy of habitat distribution models. In the current study, both Cohen’s kappa and the TSS are used as threshold-dependent measures in assessing the accuracy of the produced models along with the overall accuracy, sensitivity (the proportion of the correctly predicted presence observations), and specificity (the proportion of the correctly predicted absence observations). The threshold-independent area under the receiver operating curve (AUROC) [68] was also used to assess the accuracy of the models.

$$kappa = \frac{\left(\frac{a+b}{n}\right) - \frac{(a+b)(a+c)+(c+d)(d+b)}{n^2}}{1 - \frac{(a+b)(a+c)+(c+d)(d+b)}{n^2}}$$

$$TSS = \left(\left(\frac{a}{a+c}\right) + \left(\frac{d}{b+d}\right)\right) - 1$$

Where *a*, number of test presence records which were correctly predicted by the model; *b*, number of test absence records which the model predicted as presence; c, number of test presence records which the model predicted as absence; *d*, number of test absence records that were correctly predicted by the model; *n*, the total number of the test records.

F. Studying the Combined Impact of Land Use and Climate Change

Species distribution modeling is used frequently to predict the potential changes in species distribution under different change scenarios [48], [47]. Prediction of the potential shift in plant distribution under different climate change scenarios is considered as one of the important applications of the species distribution models [69], [47]. Most of the studies that project the impact of climate change on species distributions have been applied on global or regional scales (for example; study by Sala and colleagues [14], and study by Skov and Svenning [70]). However, there is a need for applying the same principles at the landscape level which will be of great help to conservation efforts at this scale [71]. The information provided by such tools is considered crucial for decision making related to land management and conservation planning [72], [4]. Most of the studies that have predicted the potential change in plant species under climate change scenarios have focused on temperate regions (for example; [45], [73], [71]). The current study provides an assessment of the potential impact of climate change on the distribution of ten plant species in a desert ecosystem.

Mapping the distribution of all the species recorded in the study area is a lofty goal that cannot be achieved in one single study due to the insufficiency of the occurrence records and additional logistical challenges. To overcome this problem, the current study sought to focus on predicting the distribution of 'important' species with sufficient occurrence records. Important species were defined as those serving crucial functions and providing important services in any ecosystem. This could include, for example, sand stabilizing and nitrogen-fixing plants. Many of the species recorded in the coastal area are considered 'multipurpose' species providing multi-use for local inhabitants [36], [37]. The current study focused on ten important species based on their importance values as indicated by the Species Conservation Importance (SCI) [38] and the number of occurrence records for each species. The value of the index includes information related to the conservation status, commonness, biological type, and utilitarian value of each species. The value of the SCI are in the range from 0.2 to 1,with values approaching 1 indicating species with high importance value and those approaching 0.2 indicating species with a low importance value [38], [39]. The species with SCI value of 0.55 or more and sufficient number of occurrence records (> 100) were modeled.

Land use/land cover maps representing different dates (1988, 2011 and projected 2023) were used to assess the impact of land use change on the distribution of the ten modeled plant species [34]. Each of these LULC maps represents a different stage of human influence on the landscape, with an increase in human impact with time. The maps were reclassified into two categories only to create digital Boolean layers. Natural areas category represent all the areas that have not been transformed by human activities and the man-made category that includes all the artificially created areas (For example urban, roads, orchards and croplands). The natural areas were assigned values of one, while those considered man-made were assigned values of zero. The Boolean layers representing each date were multiplied by the layers that represent the potential distribution of each of the modeled ten species. Thus the reduction or the expansion in the area occupied by each species under each land use scenario was estimated.

For projecting the potential distribution of the ten species of interest under different climatic scenarios, predicted climate changes according to the CSIRO Mk 2.0 &Mk3.0 GCMs [74] were employed. These models are used to represent the predicted climate over the period 2010-2040 under different emission scenarios;

A2A and B2A are high greenhouse emission scenarios, while A1b is a medium emission scenario. The data were retrieved from the CGIAR Research Program on Climate Change, Agriculture and Food Security (CCAFS) web: http://www.ccafs-climate.org/data/. The projected distribution of the plant species in the study area according to the used climate scenarios were compared to their potential distribution under the baseline climate. Twelve scenarios were developed for each species (Table 2) to estimate the change in species habitats under the combined impacts of changes in land use and climate. The increases and the decreases in the habitat area for each species under the different scenarios were estimated.

Table 2. Scenarios of climate and land use change used in the study. The annual mean temperature and the annual precipitation predicted for the period 2010–2040 by each climate change scenario are compared to the baseline climate that represents an average for the period 1950-2000 [15]

Climate change scenarios	Land use change scenario		
	No land use Natural landscape (1)	Current land use scenario (2011) (2)	Simulated future scenario (2023) (3)
a) Average Climate (1950-2000)	Baseline climate/Natural	Baseline climate/2011	Baseline climate/2023
b) A1B (+1.03 ºC & -12.23 mm)	A1B/ Natural	A1B/2011	A1B/2023
c) A2A (+1.14 ºC & +3.11 mm)	A2A/ Natural	A2A/2011	A2A/2023
d) B2A (+1.28 ºC & -6.34 mm)	B2A/ Natural	B2A/2011	B2A/2023

III. RESULTS& DISCUSSION

A. Species Distribution

A total of 244 species were recorded in the study area, out of which 57% are perennials, 38% are annuals and the remaining are biennials or short lived perennials. Species recorded in the study area belong to fifty taxonomic families. Compositae (Asteraceae), Gramineae, Leguminosae (Fabaceae) and Chenopodiaceae are contributing the most to the flora of the region; this is in accordance with the study by Shaltout [75].The use of SII facilitated the selection of the species based on their importance. The distribution of 10 out of the 244 species recorded in the study area was modeled (Table 3).

Eight models out of the ten attained an area under the curve (AUC) value over 0.7, which indicates that these models are of moderate performance [76]. Astragalus spinosus and Stipagrostis obtuse models attained AUC values exceeding 0.65, which indicates that the models are better than random. Based on kappa values, Astragalus spinosus, Echinops spinosus, and Stipagrostis obtuse models are considered of poor performance as they had kappa values less than 0.4 (Table 3). The models of seven species out of the ten performed fairly well as indicated by all the used measures of accuracy assessment. Both models of Haloxylon salicornicum and Noaea mucronata exhibited good performance with kappa and TSS exceeding 0.5, AUC above 0.8, and overall accuracy above 81%.

The accuracy and the predictive power of any species distribution model depends on the quality and the accuracy of the field data employed and the choice of the environmental variables to be used in the model [40]. Taking into account the limitation of the resolution of the environmental data employed in the study, particularly the climatic variables used for predicting the distribution of species in the study area, the results obtained are considered acceptable. The availability of high resolution environmental predictors is important for modeling the distribution of species at landscape scales [77], [47]. Such high resolution environmental data is difficult to obtain for the poorly studied areas. The deficiency in geographic databases (topographic and climatic databases) representing areas in developing countries and underdeveloped areas was and is still one of the major problems that faces researchers.

The pattern of species distribution is often related to a number of environmental variables. Predictive models of species distribution could include variables selected based on a theoretical basis following conceptual model [78]. The conceptual framework for modeling plant species suggested by Franklin [1] was revisited by Austin and Van [47]. They emphasized including environmental predictors that are considered direct factors influencing plant growth and distribution. This included light, temperature, nutrients, water, carbon dioxide and biotic interaction.

Although it is important to include the variables that correlate to the species distribution and also show meaningful biological relationships [78]; some studies fail to include some factors of importance. Austin and Van [47] highlighted the need for inclusion of light as a predictor in models predicting distribution of plant species, which has been overlooked by many studies. They argued that light as a predictor has an important influence on distribution of plant species. In the current study, light was included in modeling species of the study area expressed as total insolation, direct insolation, diffusion insolation, and direct/diffusion insolation ratios. Each of these factors was found to be important for modeling plant species in the study area. Diffusion insolation was found to be important for predicting all the species except for Echinops spinosus, for which direct insolation was found important (Table 4). Austin and Van [47] maintained that the difference in light regime between north and south-facing aspects can result in differences in temperature equal to that resulting from a shift of 200 km in latitude.

Table 3. The modeled important plant species selected out of the 244 species recorded in the study area; abbreviations used; estimated species importance index (SII) values; number of occurrences recorded in the study area; and the measures used to assess the accuracy of the random forests models predicting their distribution. Accuracy assessment measures presented are: Sensitivity; Specificity; True skill statistic (TSS); Cohen's Kappa statistic; the overall accuracy; and the area under the curve (AUC) statistic of the receiver operating characteristic (ROC).

Species	Abbreviation	SII	Number of occurrences	Sensitivity	Specificity	TSS	Kappa	Accuracy	AUC
Anabasis articulata (Forssk.) Moq.	Ana_art	0.72	454	0.92	0.509	0.429	0.447	73.790	0.790
Asphodelus aestivus Brot.	Asp_aes	0.64	119	0.533	0.882	0.415	0.405	81.855	0.828
Astragalus spinosus (Forssk.) Muschl.	Ast_spi	0.64	137	0.442	0.784	0.226	0.191	72.470	0.664
Deverra tortuosa (Desf.) DC.	Dev_tor	0.76	212	0.589	0.828	0.417	0.417	75.709	0.764
Echinops spinosus L.	Ech_spi	0.64	103	0.489	0.847	0.335	0.314	78.138	0.703
Gymnocarpos decanderus Forssk.	Gym_dec	0.64	250	0.835	0.62	0.455	0.401	69.355	0.744
Haloxylon salicornicum (Moq.) Bunge ex Boiss.	Hal_sal	0.6	184	0.709	0.845	0.554	0.507	81.452	0.840
Noaea mucronata (Forssk.) Asch. and Schweinf.	Noa_muc	0.56	211	0.73	0.849	0.579	0.547	81.855	0.872
Stipagrostis obtuse (Delile) Nees	Sti_obt	0.56	208	0.651	0.697	0.348	0.296	68.548	0.671
Thymelaea hirsuta (L.) Endl.	Thy_hir	0.76	300	0.784	0.682	0.466	0.444	72.177	0.789

Table 4. Variables selected for the predictive models for each species based on the percentage increase in MSE when a given variable was randomly permuted and introduced into the model. See Table 1 for variable abbreviations and Table 3 for species binomial abbreviations.

Variable	Ana_art	Asp_aes	Ast_spi	Dev_tor	Ech_spi	Gym_dec	Hal_sal	Noa_muc	Sti_obt	Thy_hir
Bio2	+	+	+	+	+	+	+		+	+
Bio3	+	+						+		+
Bio4	+	+	+	+	+	+	+	+	+	+
Bio12	+	+	+	+	+	+	+			+
Bio13		+						+		+
Bio15										+
Bio16	+	+	+	+	+	+	+	+	+	+
Bio19		+			+					+
ELv	+	+	+		+	+	+	+	+	+
LS			+					+		
Slope				+	+				+	
TRI			+	+						
TWI		+	+	+	+			+	+	+
ProxtoSea	+	+	+	+	+	+	+	+	+	+
DiffInsol	+	+	+	+		+	+	+	+	+
DirInsol		+	+	+	+					
DiffToDir									+	+

In the current study, generally seventeen out of the original thirty environmental variables contributed to the modeling of the species in the study area. Of the climatic variables, the mean of temperature diurnal range, temperature seasonality, annual precipitation and precipitation of the wettest quarter were the common climatic factors in controlling the distribution of most the modeled species (Table 4). Climatic variables representing annual cycle (for example annual mean temperature and annual precipitation) seem to control the general vegetation cover over the broad scale.

Bornkamm and Kehl [24] divided the western desert into five zones characterized by different vegetation cover and plant communities based on the mean annual rainfall. The study area falls within Zone I and Zone II of this classification. The vegetation cover of Zone I (semi-desert with mean annual rainfall > 20 mm) is composed of dwarf shrubs dominated by Thymelaea hirsuta. Zones II and III are full-desert (with mean annual rainfall 10-20 mm) with communities dominated by Asphodelus microcarpus and Plantago albicans. Climatic factors that represent seasonality (e.g. mean of temperature diurnal range, temperature seasonality and precipitation of the wettest quarter) are more important for the distribution of the species at local scales as is suggested by the results of the current study. The results indicate that the land-surface parameters are of influence on the distribution of species. Topographic factors such as elevation, diffusion insolation, direct insolation, and topographic wetness index were found to be important in predicting most of the modeled species (Table 4). Hammouda [79] in a study focusing on the Omayed area (part of the study area) found that species distribution and plant community composition are influenced by topography, the nature and origin of the parent material, in addition to the land use and degree of human intervention. Land-surface parameters controlling moisture availability were found to be of importance for species distribution by some studies that focused on assessing the quantitative relationships between environmental variables and vegetation in the northwestern desert (for example; [80], [81], [82], [83]). Ayyad and Ammar [81] found that abundance and the distribution of the perennials are more affected by factors controlling moisture availability through run-off; such as slope and curvature. Ayyad and Ammar [84] also, found factors controlling moisture availability (for example; slope inclination, topographic position, nature of surface, soil depth and soil texture) which are the most important in controlling vegetation composition in the area. Ayyad and El-Ghareeb [83] found that the micro-variations in the soil were attributed to variations in topography and the nature of parent materials on the distribution of species in the area. The results of the current study also showed that the proximity to sea is one of the common important factors for predicting all the modeled species. Communities of the coastal dunes dominated by Echinops spinosus and Thymelea hirsuta and those of the inland ridges dominated by Gymnocarpos decanderus and Deverra tortuosa are stated to be the most diverse in the area [85]. However, these communities are stated to be threatened due to the establishment of summer resorts on the coastal dunes and the establishment of the irrigation network on the non-saline depressions [86].

B. *Effect of Climate and Land Use Changes on Species Distribution*

1. Effect of land use change

Species distribution models are increasingly used for prediction of the potential distribution of the species in response to disturbance or changes resulting from human intervention. Predictive habitat distribution models are used as important tools for assessing the impact of land use change and other forms of human interference on different species. Habitat distribution models have proven to be useful for modeling both commonly distributed species [87] as well as rare species [12], [54]. Some studies used models with AUC values > 0.6 for projecting the impact of climate change on plant distribution [71]. However, the intention here was to be more conservative and use only the models that showed reasonable performance according to all the accuracy assessment measures to assess the impact of both land use and climate change. As a result, only seven species were mapped to assess the impact of change in land use on their distribution (Figure 2). Assessment was done by comparing the area occupied by each species under no land use change in the area (theoretically natural landscape) to that in the years 1988 and 2011. The results show that all species face reduction in their habitats (Figure 3). The results also show that all the species are at risk for increased reduction of their habitats under the projected land use change by the year 2023.

Noaea mucronata attained the maximum loss in habitat area in 1988 (7.47% of the potential area; Figure 3), this increased five folds by 2011 (37.74%) and six folds by 2023 (44.79%). The major loss for this species occurs between the years 1988 and 2011. This trend is noticed for all the modeled species. Halmy and colleagues [34], [38] assessed the change in the landscape between the years 1988 and 2011 and found that the landscape has experienced changes by which many natural areas were transformed to new uses. The study concluded that the landscape is trending towards being more artificial. This explains the dramatic increase in loss of areas occupied by each species between the years 1988 and 2011. The projected loss in the species' area between the years 2011 and 2023 was shown to be lower than that between 1988 and 2011. Noaea mucronata, Asphodelus aestivus, and Deverra tortuosa (Figure 3) are most affected by the changes in land use in the period 1988-2011 and will continue to be at risk of habitat loss by the year 2023. The distribution of these three species is concentrated in the northern part of the landscape. This part of the landscape has been the most modified by human activities, and will continue to face more modifications pressures in the future.

The urban sprawl, agricultural activities and other activities occurring in the area have resulted in habitat loss. These recent changes in the region place the plant species and their habitats under threat. In the late 1980s, establishment of summer resorts on the coastal dunes started to reshape the landscape of the area. Quarrying activities increased as a result of the establishment of these resorts. Mining and cutting of the limestone ridges in the area provide building materials necessary for the establishment of the resorts. This may have contributed to the fragmentation, destruction and loss of habitats. Species inhabiting the coastal dunes and the non-saline depression habitats are stated to be threatened due to the establishment of summer resorts on the coastal dunes and the establishment of the irrigation network on the non-saline depression [86]. Factors such as habitat size reduction or habitat fragmentation represent the most serious causes of species loss. However, arrangement and connectivity of habitat patches are also of great importance. Habitat fragmentation makes it difficult for wildlife to maintain stable populations [88], [89]. The current study did not assess the fragmentation in the habitat of each species or estimated the degree of connectivity among patches. This will be part of future work planned to include more species with restricted distribution in the area.

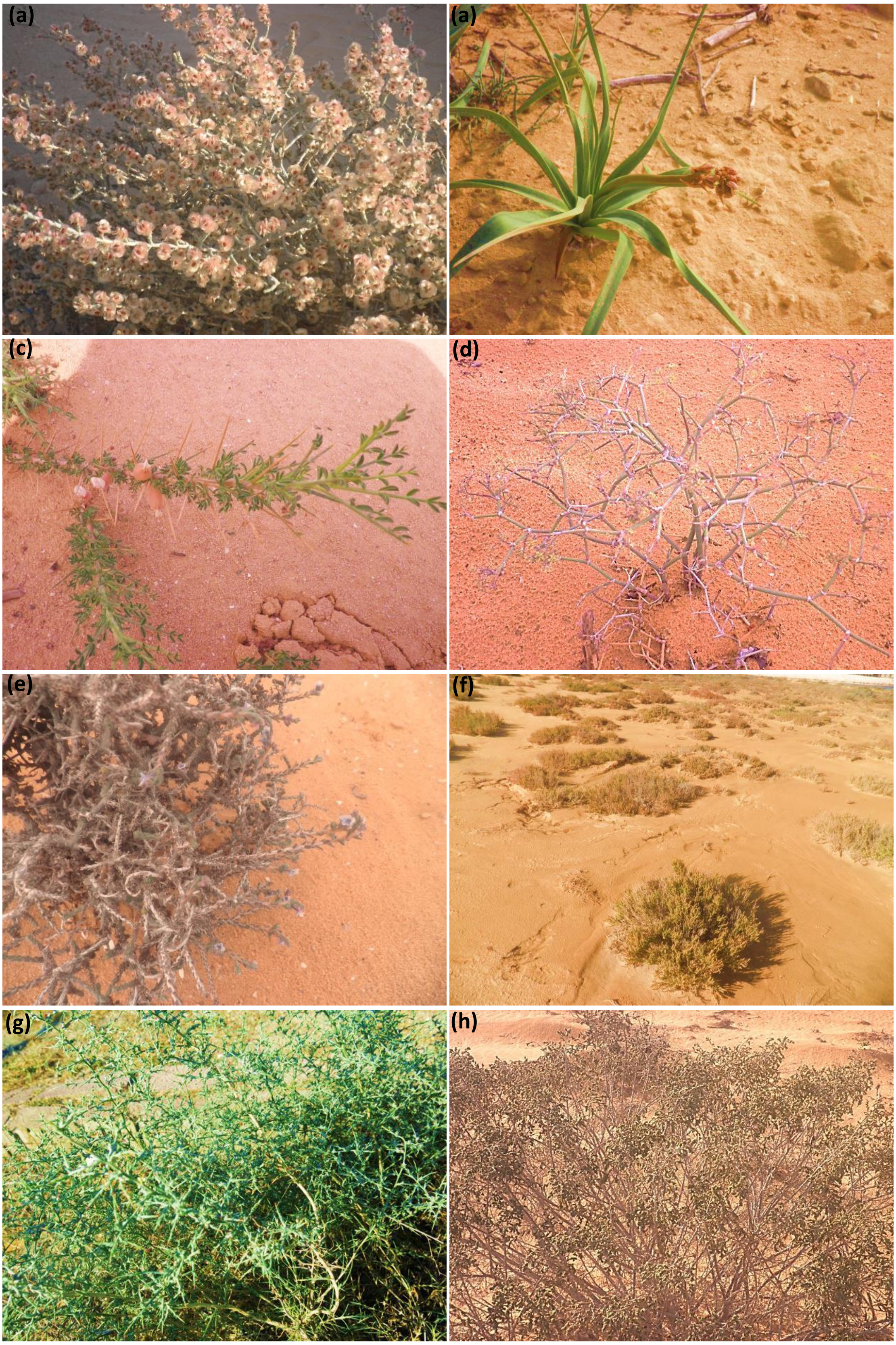

Fig .2. Some of the species modelled; (a) Anabasis articulata, (b) Asphodelus aestivus, (c) Astragalus spinosus, (d) Deverra tortuosa, (e) Gymnocarpos decanderus, (f) Haloxylon salicornicum, (g) Noaea mucronata, and (h) Thymelaea hirsuta.

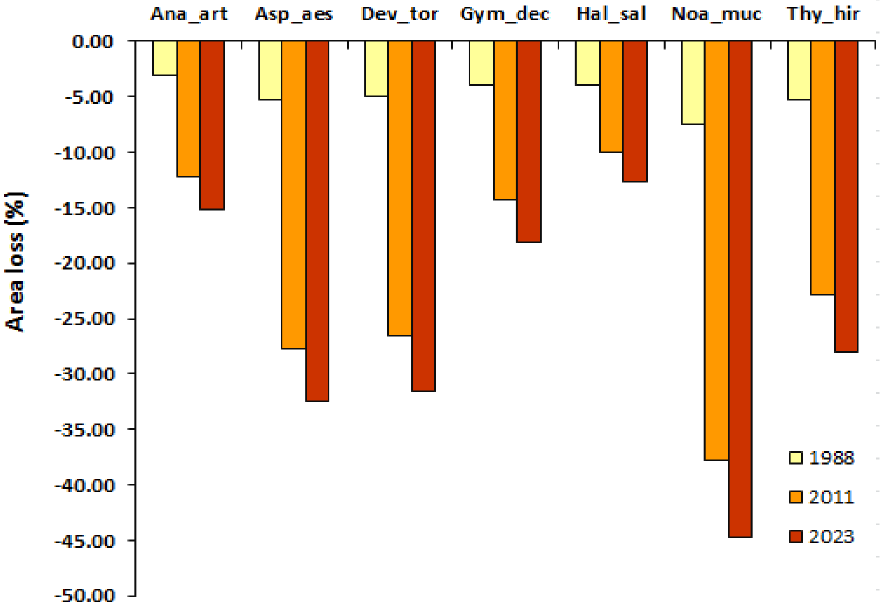

Fig .3. Change in habitat area due to change in land use in 1988, 2011, and the projected change by 2023. The loss is expressed as percentage of the potential habitat area for each species under the baseline climate and no land use. See Table 3 for species binomial abbreviations.

2. Effect of climate change

Many studies have focused on projecting the impact of climate change on the distribution of plant species [45], [90], [14], [73], [91], [92], [71]. Most of these studies have been applied on global or regional scale. The current study attempts to assess the potential impact that climate change might have on the distribution of some plant species at the landscape scale within a desert ecosystem.

Under the CSIRO GCM models, the different emission scenarios used in the current study are predicted to lead to changes in the temperature and precipitation of the area (Table 2 & Figure 4). The study area is expected to experience an increase in annual mean temperature under the three applied scenarios, with B2A expected to result in the highest increase in temperature. Not all the scenarios predict reduction in the annual mean precipitation of the area. The area is expected to experience increase in the annual mean precipitation by 3.11mm compared to the average over the period 1950-2000 under the A2A scenario. Climate has an influence on species distribution at broad scale [45], [93].The results show that at the landscape level and the change in climate under the different emission scenarios have resulted in changes in the modeled species distribution. Although the differences among the climate scenarios developed by the different models up to 2050 are stated to be minor [94], [95], the current results show that the expected impact of each of the used climate scenarios on the modeled species is different (Figure 4).

Noaea mucronata, Asphodelus aestivus, and Anabasis articulataare are expected to be at risk of loss of habitat under all the employed scenarios. The high emission scenarios B2A and A2A cause higher impact on these species compared to the low emission scenario (A1B). For example, under B2A Noaea mucronata, Asphodelus aestivus, and Anabasis articulata are expected to lose about 96%, 58% and 17% of their potential area respectively, while under A1B each are expected to lose 85%, 29%, and 13% of their potential area respectively (Figure 5). Scenario A1B, on the contrary, is expected to cause more loss in area for Asphodelus aestivus and Deverra tortuosa (29% and 7%, respectively) compared to the A2A scenario (23% and 2%, respectively). For Gymnocarpos decanderus, and Haloxylon salicornicum the A1B scenario is expected to cause loss in the area of their habitat (1.2% and 2.2%, respectively), while these species are expected to gain habitat under the other two high emission scenarios (20.5 and 5.8% under A2A scenario, respectively). Under the A1B scenario, there will be an expected reduction in the annual precipitation and precipitation of the wettest quarter compared to the average observed for the period 1950-2000 (Figure 4). On the contrary, under the A2A and B2A scenarios, the area is expected to experience increase in both annual precipitation and precipitation of wettest quarter compared to the average observed for the period 1950-2000. These factors were found to be important for the occurrence of Asphodelus aestivus, Deverra tortuosa, Gymnocarpos decanderus, and Haloxylon salicornicum (Table 4). Thymelaea hirsute seems to favor the change in climate under the three different scenarios. The species is expected to gain habitat under these scenarios. The decrease in temperature seasonality and the increase in annual precipitation, precipitation of wettest month, precipitation of wettest quarter, and precipitation of coldest quarter under A2A and B2A compared to the average for the period 1950-2000 may explain this expected gain in habitat for Thymelaea hirsute under these scenarios. Noea mucronata is expected to be the most affected of the modeled species by the change in climate under the employed scenarios. Noea mucronata seems to be sensitive to the increase in temperature seasonality that is expected to increase under the three scenarios.

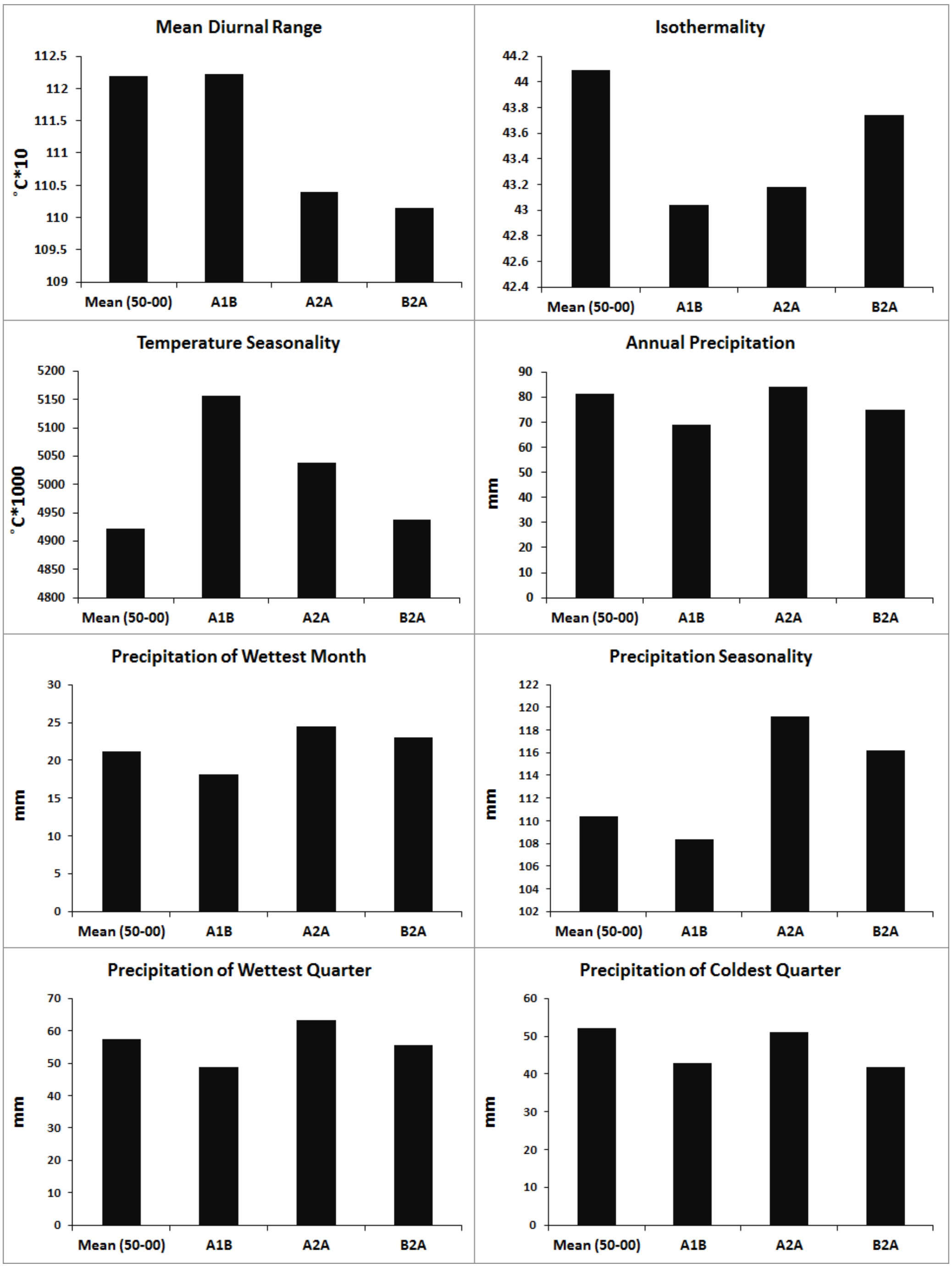

Fig .4 Mean of the climatic variables contributed in modeling plant species in the study area. The mean is calculated over the whole study area for each scenario (A1B, A2A & B2A) and for the baseline climate that represents the mean for the period 1950- 2000.

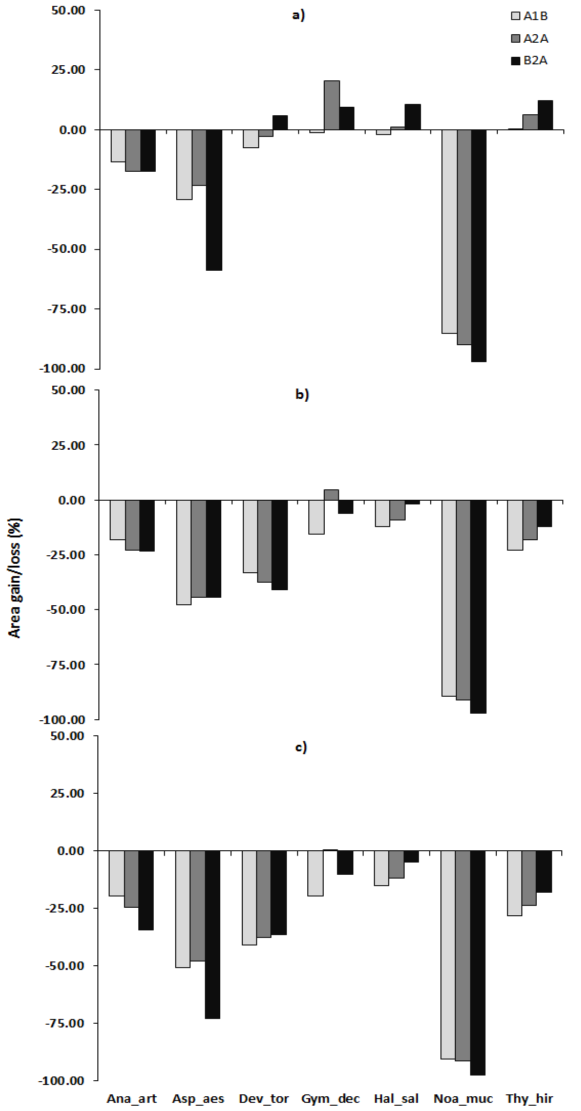

Fig .5. Gain/loss in habitat area under three climate change scenarios combined with different land use scenarios: a) no land use; b) current land use; and c) projected land use scenario by the year 2023. Gain/loss is expressed as percentage of the potential habitat area for each species under the baseline climate and no land use. See Table 3 for species binomial abbreviations.

3. Land use and climate change combined effect

The results show that while the change in land use in the study area resulted in loss of the area of the potential habitat for all species, the change in the climate under the employed scenarios may result in gain in area for some species. The expected loss in the area of Noaea mucronata, Asphodelus aestivus, and Anabasis articulata (96%, 58%, and 17%, respectively) under the high emission climate change scenario B2A is higher than the expected loss under the projected change in land use by the year 2023 (44%, 32%, and 15%, respectively). Under the scenarios of combined change in climate and land use either under the current land use or that projected by 2023, all the species are expected to suffer loss in area (Figure 5). An exception to that is Gymnocarpos decanderus, which is expected to gain area under the combined scenario of A2A emission and each of the current land use scenarios and the projected land use by 2023. However, this increase is less than 5% of the potential area suitable for the species under A2A/2011 scenario and less than 1% under A2A/2023 scenario. The results reveal the serious fate that plant species might face under scenarios of climate and land use change. Immediate actions are needed to ensure that species as Asphodelus aestivus (Figure 6) and Noaea mucronata (Figure 7) are not declining in other places across the northwestern coast. The current study modeled the distribution of the species in part of the phytogeographical region and the status of these species needs to be known over the whole phytogeographical region. More future studies to assess the status of the species in the area, especially those of restricted distribution, are still needed. Based on the findings of these results, measures should be taken to maintain these species in the flora of the region.

IV. CONCLUSIONS

The application of random forests to the employed climatic and land-surface parameter data proved to be successful in predicting the distribution of the plant species in the arid land landscape. The performance of the species distribution models in the current study could be attributed to the resolution of the environmental predictors used. At the landscape level the use of finer scale environmental predictors, especially climatic factors, may increase the prediction power of distribution models. The inclusion of environmental predictors that represent light proved to be of importance for the prediction of some of the modeled species in the study area.

The study found that the expected impact of the A1B, A2Aand B2A scenarios on the distribution of the modeled species is variable. In arid lands some species might be adversely affected by the change in climate under certain scenarios, while others might benefit from these changes. Land use change poses more risk on most of the species modeled compared to climate change. The impact of land use is not differential while that of climate change is. Change in land use in the area resulted in habitat loss for all the modeled species. Land use change impact could be faster and more substantial in reducing the size of plant species habitat. If the current trend in land use change continues, all species will continue to suffer habitat loss. The combined impact of land use and climate change pose serious threats to most of the species modeled. Under combined scenarios of change in land use as projected by 2023 and change in climate, all the species are expected to suffer loss in habitat, except Gymnocarpos decanderus.The results show that some species such as Noaea mucronata and Asphodelus aestivus may suffer serious threats in the area under the combined land use climate change scenarios. So, actions are needed to ensure that these species are not threatened across the northwestern coast and in Egypt. This also, highlights the importance of assessing the impact of land use/climate change scenarios on other species of restricted distribution in the area.The application of species distribution modeling in desert and arid lands can provide a useful tool for mapping species and assessing the impact of human induced changes on different species. Such applications are still rare, and this may be attributed to the fact that most of the arid lands and deserts are located in inaccessible or lightly populated areas. Most of these areas are also located in less developed areas where the systematic surveys of the natural resources are not conducted on a regular basis. The lack of environmental predictors of appropriate landscape resolution to be used for modeling species in such areas is another factor to be considered. The current study will promote more studies that map plant species distribution and assess the risk to important species as a result of human interference. Future studies are needed to assess the magnitude of fragmentation in each species habitat and to estimate the degree of connectivity among patches.

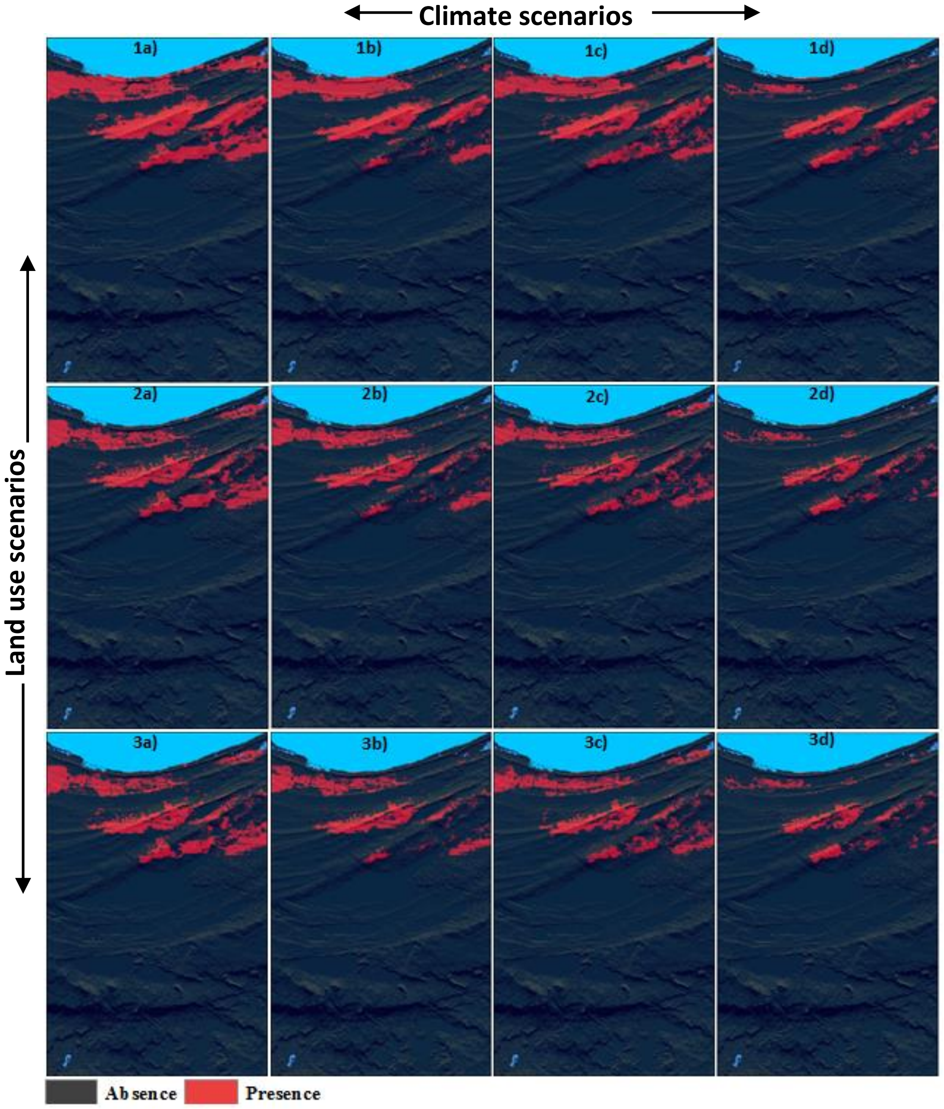

Fig .6 Potential distribution of Asphodelus aestivus under different land use and climate scenarios.1, 2 and 3 represent the natural landscape, current land use and future land use by 2023, respectively; and a, b, c and d represent the average climate (1950-2000), A1B, A2A and B2A climatic scenarios, respectively.

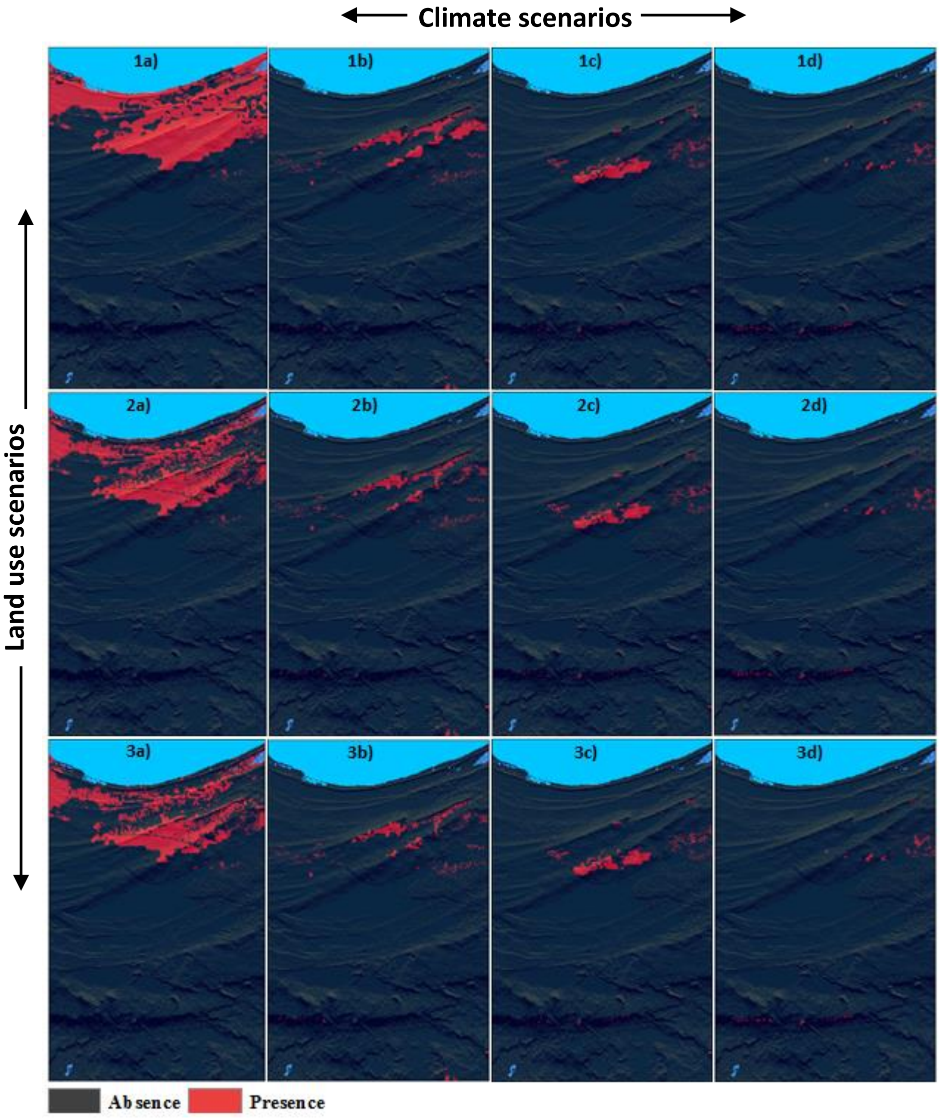

Fig .7 Potential distribution of Noaea mucronata under different land use and climate scenarios.1, 2 and 3 represent the natural landscape, current land use and future land use by 2023, respectively; and a, b, c and d represent the average climate (1950-2000), A1B, A2A and B2A climatic scenarios, respectively.

REFERENCES

[1] J. Franklin, "Predictive vegetation mapping: geographic modelling of biospatial patterns in relation to environmental gradient," Progress in Physical Geography, vol. 19, pp. 474-199, 1995.

[2] J. Elith and J. R. Leathwick, "Species distribution models: Ecological explanation and prediction across time and space," Annual Rev. Ecol. Evol. Syst., vol. 40, pp. 677-697, 2009.

[3] J. Franklin, Mapping Species Distribution: Spatial Inference and Prediction, Cambridge University Press, 2009.

[4] A. Guisan and N. E. Zimmermann, "Predictive habitat distribution models in ecology," Ecological Modeling, vol. 135, p. 147–186, 2000.

[5] A. Guisan and W. Theuriller, "Predicting species distribution: offering more than simple habitat models," Ecology Letters, vol. 8, p. 993–1009, 2005.

[6] J. Elith, S. J. Phillips, T. Hastie, M. Dudík, Y. E. Chee and C. J. Yates, "A statistical explanation of MaxEnt for ecologists," Diversity and Distributions, vol. 17, p. 43–57, 2011.

[7] P. Segurado and M. B. Araújo, Journal of Biogeography, vol. 31, pp. 1555-1568, 2004.

[8] J. Elith, C. H. Graham, P. R. Anderson, M. Dudik, S. Ferrier, A. Guisan et al., "Novel

methods improve prediction of species' distributions from occurrence data," Ecography, vol. 29, pp. 129-151, 2006.

[9] M. J. M. and W. Jetz, "Effects of species' ecology on the accuracy of distribution models," Ecography, vol. 30, p. 135–151, 2007.

[10] P. A. Hernandez, I. Franke, S. K. Herzog, V. Pacheco, L. Paniagua, H. Quintana et al., "Predicting species distributions in poorly-studied landscapes," Biodiversity Conservation, vol. 17, pp. 1353-1366, 2008.

[11] C. Liu, M. White and G. Newell, Ecography, vol. 34, pp. 232-243, 2011.

[12] X. B. Wu and F. E. Smeins, "Multiple-scale habitat modeling approach for rare plant conservation. Landscape and Urban Planning," Landscape and Urban Planning, vol. 51, pp. 11-28, 2000.

[13] J. Franklin, "Moving beyond static species distribution models in support of conservation biogeography," Diversity and Distributions, vol. 16, p. 321–330, 2010.

[14] O. E. Sala, F. S. Chapin, J. J. Armesto, E. Berlow, J. Bloomfield, R. Dirzo et al., "Global Biodiversity Scenarios for the Year 2100," Science, vol. 287, pp. 1770-1774, 2000.

[15] R. J. Hijmans, S. E. Cameron, J. L. Parra, P. G. Jones and A. Jarvis, "Very high resolution interpolated climate surfaces for global land areas," International Journal of Climatology, vol. 25, p. 1965–1978, 2005.

[16] J. Ramirez and A. Jarvis, Disaggregation of global circulation model outputs: Decision and policy analysis working paper No. 2. CGIAR Challenge Program on Climate Change, Agriculture and Food Security, CCAFS., CGIAR Challenge Program on Climate Change, Agriculture and Food Security, CCAFS, 2010.

[17] P. Jones and P. K. Thornton, "Croppers to livestock keepers: livelihood transitions to 2050 in Africa due to climate change," Environmental Science and Policy, vol. 12, p. 427–437, 2009.

[18] A. Jarvis, H. Reuter, A. Nelson and E. Guevara, "Hole-filled SRTM for the globe Version 4," 2008.

[19] A. Bütof, L. R. von Riedmatten, C. F. Dormann, M. Scherer-Lorenzen, E. Welk and H. Bruelheide, "The responses of grassland plants to experimentally simulated climate change depend on land use and region," Global Change Biology, vol. 18, p. 127–137, 2012.

[20] A. C. Hughes, C. Satasook, P. J. J. Bates, S. Bumrungsri and G. Jones, "The projected effects of climatic and vegetation changes on the distribution and diversity of Southeast Asian bats," Global Change Biology, vol. 18, p. 1854–1865, 2012.

[21] J. C. Brito, A. L. Acosta, F. Álvares and F. Cuzin, "Biogeography and conservation of taxa from remote regions: An application of ecological-niche based models and GIS to North-African Canids," Biological Conservation, vol. 142, p. 3020–3029.

[22] M. A. Ayyad and S. I. Ghabbour, "Hot desert of Egypt and Sudan," in Hot desert and arid shrublands, M. Evenari, I. B. Meir and D. Godall, Eds., Amsterdam, Elsevier, 1986, pp. 1-16.

[23] M. A. Ayyad and S. I. Ghabbour, "Dry coastal ecosystem of eastern North Africa," in Dry coastal ecosystems: Africa, America, Asia and Oceania. Ecosystems of the world, vol. 2B, E. van der Maarel, Ed., Amsterdam, Elsevier, 1993, pp. 149-201.

[24] R. Bornkamm and H. Kehl, "Landscape ecology of the western desert of Egypt," Journal of Arid Environments, vol. 17, pp. 271-277, 1989.

[25] SUMAMAD (Sustainable Management of Marginal Drylands), "Omayed Biosphere Reserve and its hinterland," submitted to National UNESCO Commission, Cairo, 2005.

[26] M. S. Abdel Razik, "Plant diversity changes in response to environmental drivers and pressures at El Omayed 'ROSELT/OSS' observatory, Egypt," in The future of the drylands, Conference on Desertification and Drylands Research, Tunisia, 19-21 June 2006, C. C. Lee and T. Schaaf, Eds., Netherlands, UNESCO, pp. 289-309.

[27] M. A. Kassas, A. Abdallah, T. Abul-Dahab, G. M. Atta, M. Esawi, H. Farouk et al., "Management Plan For Omayed Protected Area.," Med Wet Coast, Global Environment Facility and Egyptian Environment Affairs Agency (UNDP-GEFand EEAA), 2002.

[28] V. Täckholm, Students' Flora of Egypt, 2nd ed., Cairo: Cairo University, 1974, p. 888.

[29] L. Boulos, Flora of Egypt, vol. 1, Cairo: Al Hadara Publishing, 1999, p. 417.

[30] L. Boulos, Flora of Egypt, vol. 2, Cairo: Al Hadara Publishing, 2000, p. 352.

[31] L. Boulos, Flora of Egypt, vol. 3, Cairo: Al Hadara Publishing, 2002, p. 373.

[32] L. Boulos, Flora of Egypt, vol. 4, Cairo: Al Hadara Publishing, 2005, p. 617.

[33] L. Boulos, Flora of Egypt: Checklist, Cairo: Al Hadara Publishing, 2009, p. 410.

[34] M. W. Halmy, P. Gessler, J. A. Hicke and B. B. Salem, "Land use/land cover change detection and prediction in the north-western coastal desert of Egypt using Markov-CA," Applied Geography, vol. 63, pp. 101-112, 2015.

[35] S. J. Phillips, M. Dudík, J. Elith, C. H. Graham, A. Lehmann, J. Leathwick and S. Ferrier, "Sample selection bias and presence-only distribution models: implications for background and pseudo-absence data," Ecological Applications, vol. 19, pp. 181-197, 2009.

[36] M. Ayyad, Multipurpose species in Arab African countries, Cairo: UNESCO, 1998.

[37] S. Z. Heneidy and L. M. Bidak, "Potential uses of plant species of the coastal Mediterranean region, Egypt," Pakistan Journal of Biological Science, vol. 7, pp. 1010-1023, 2004.

[38] M. W. A. Halmy, Environmental risk assessment for habitats of the Egyptian northwestern coastal desert (Doctoral dissertation), University of Idaho: ProQuest Dissertations and Theses, 2012.

[39] M. W. A. Halmy and B. B. Salem, "Species conservation importance index (SCI) for comparing sites' conservation value at landscape level.," Brazilian Journal of Botany, 2015.

[40] A. T. Peterson and Y. Nakazawa, "Environmental data sets matter in ecological niche modelling: an example with Solenopsis invicta and Solenopsis richteri," Global Ecology and Biogeography, vol. 17, p. 135–144, 2008.

[41] S. Jelaska, "Vegetation mapping applications," in Goemorphometry: concepts, software, applications, T. T. Hengl and I. Evans, Eds., Elsevier, 2009, pp. 141-169.

[42] V. Olaya, "Basic land-surface parameters," in Goemorphometry: concepts, software, applications, T. Hengl and H. I. Reuter, Eds., Elsevier, 2009, pp. 141-169.

[43] I. D. Moore, P. E. Gessler, G. A. Neilsen and G. A. Petersen, "Soil attribute prediction using terrain analysis," Soil Science Society of America Journal, vol. 57, pp. 443-452, 1993.

[44] SAGA (System for Automated Geoscientific Analyses), 2011.

[45] N. E. Zimmermann and F. Kienast, "Predictive mapping of alpine grasslands in Switzerland: Species versus community approach," Journal of Vegetation Science, vol. 10, pp. 469-482, 1999.

[46] D. J. Kriticos, B. L. Webber, A. Leriche, N. Ota, I. Macadam, J. Bathols and J. Scott, "CliMond: global high resolution historical and future scenario climate surfaces for bioclimatic modelling," Methods in Ecology and Evolution, vol. 3, pp. 53-64, 2012.

[47] M. P. Austin and K. P. Van Niel, "Improving species distribution models for climate change studies: variable selection and scale," Journal of Biogeography, vol. 38, p. 1–8, 2011.

[48] J. Elith, S. J. Phillips, T. Hastie, M. Dudík, Y. E. Chee and C. J. Yates, "A statistical explanation of MaxEnt for ecologists," Diversity and Distributions, vol. 17, p. 1–15, 2010.

[49] R Development Core Team 2.13.1, "A language and environment for statistical computing.," 2011.

[50] A. Liaw and M. Wiener, "Classification and regression by random forest," R News, vol. 2, pp. 18-22, 2002.

[51] A. M. Prasad, L. R. Iverson and A. Liaw, "Newer classification and regression tree techniques: Bagging and random forests for ecological prediction," Ecosystems, vol. 9, p. 181–199, 2006.

[52] D. R. Cutler, T. C. Edwards, K. H. Beard, A. Cutler, K. T. Hess, J. Gibson and J. J. Lawler, "Random forests for classification in ecology," Ecology, vol. 88, p. 2783–92, 2007.

[53] J. S. Evans and S. A. Cushman, "Gradient modeling of conifer species using random forests," Landscape Ecology, vol. 24, p. 673–683, 2009.

[54] J. N. Williams, C. Seo, J. Thorne, J. K. Nelson, S. Erwin, J. M. O'Brien and M. W. Schwartz, "Using species distribution models to predict new occurrences for rare plants," Diversity and Distributions, vol. 15, p. 565–576, 2009.

[55] L. Breiman, J. H. Frriedman, R. A. Olshen and C. J. Stone, Classification and regression trees, (Belmont: Wadsworth International Group), 1984.

[56] J. A. Benediktsson, J. Chanussot and M. Fauvel, "Multiple classifier systems in remote sensing: From basics to recent developments.," in MCS 2007, vol. 4472, M. Haindl, J. Kittler and F. Roli, Eds., Berlin Heidelberg, Springer-Verlag , 2007, pp. 501-512.

[57] L. Breiman, "Random forests," Machine learning, vol. 45, pp. 5-32, 2001.

[58] P. O. Gislason, J. A. Benediktsson and J. R. Sveinsson, "Random forest classification of multisource remote sensing and geographic data.," in Geoscience and remote sensing symposium, 2004. IGARSS 04. Proceedings., 2004.

[59] P. Gislason, J. Benediktsson and J. Sveinsson, "Random forests for land cover classification," Pattern Recognition Letters, vol. 27, pp. 294-300, 2006.

[60] N. Horning, "Random Forests: An algorithm for image classification and generation of continuous fields data sets.," New York, 2010.

[61] V. F. Rodriguez-Galiano, B. Ghimire, J. Rogan, M. Chica-Olmo and J. P. Rigol-Sanchez, "An assessment of the effectiveness of a random forest classifier for land-cover classification," ISPRS Journal of Photogrammetry and Remote Sensing, vol. 67, pp. 93-104, 2011.

[62] L. Zevenbergen and C. Thorne, "Quantitative analysis of land surface topography," Earth Surface Processes and Landforms, vol. 2, pp. 47-56, 1987.

[63] S. J. Riley, S. D. DeGloria and R. Elliot, "A terrain ruggedness index that quantifies topographic heterogeneity," Intermountain Journal of Sciences, vol. 5, pp. 23-27, 1999.

[64] G. J. Roloff, M. L. Donovan, D. W. Linden and M. L. Strong, "Lessons learned from using GIS to model landscape-level wildlife habitat," in Models for planning wildlife conservation in large landscapes, J. Millspaugh and F. R. Thompson III, Eds., Elsevier, 2009, pp. 287-320.

[65] O. Alloche, A. Tsoar and R. Kadmon, "Assessing the accuracy of species distribution models: Prevalence, kappa and the true skill statistic (TSS)," Journal of Applied Ecology, vol. 43, p. 1223–1232, 2006.

[66] J. Cohen, "A coefficient of agreement for nominal scales," Educational and Psychological Measurment, vol. 20, pp. 37-40, 1960.

[67] C. S. Peirce, "The numerical measure of the success of predictions," Science, vol. 4, pp. 453-454, 1884.

[68] S. J. Mason and N. E. Graham, "Areas beneath the relative operating characteristics (ROC) and relative operating levels (ROL) curves statistical significance and interpretation," Quarterly Journal of the Royal Meteorological Society, vol. 128, pp. 2145-2166, 2002.

[69] M. S. Wisz, R. J. Hijmans, J. Li, A. T. Peterson, C. H. Graham and A. Guisan, "Effects of sample size on the performance of species distribution models," Diversity and Distributions, vol. 14, p.

763–773, 2008.

[70] F. Skov and J. Svenning, "Potential impact of climatic change on the distribution of forest herbs in Europe potential of climatic on the distribution of forest herbs impact change in Europ," Ecography, vol. 27, p. 366–380.

[71] M. R. Trivedi, M. D. Morecroft, P. M. Berry and T. P. Dawson, "Potential effects of climate change on plant communities in three montane nature reserves in Scotland, UK," Biological Conservation, vol. 141, pp. 1665-1675, 2008.

[72] C. Margules and M. Austin, "Biological models for monitoring species decline: The construction and use of databases," Philosophical Transactions: Biological Sciences, vol. 344, p. 69–75, 1994.

[73] T. Dirnböck, S. Dullinger and G. Grabherret, "A regional impact assessment of climate and land-use change on Alpine vegetation," Journal of Biogeography, vol. 30, p. 401–417, 2003.

[74] H. B. Gordon, L. D. Rotstayn, J. L. McGregor, M. R. Dix, E. A. Kowalczyk, S. P. O'Farrell, L. J. Waterman, A. C. Hirst, S. G. Wilson, M. A. Collier, I. G. Watterson and T. I. Elliott, "The CSIRO Mk3 Climate System Model. Aspendale: CSIRO Atmospheric Research. CSIRO Atmospheric," CSIRO, 2002.

[75] K. H. Shaltout, "Monitoring flora of the Omayed biosphere reserve and measures of rehabilitation," in Proceedings of the International Workshop on Combating Desertification, 2002.

[76] S. Manel, H. C. Williams and S. J. Ormerod, "Evaluating presence – absence models in ecology: the need to account for prevalence," Journal of Applied Ecology, vol. 38, p. 921–931, 2001.

[77] T. Newbold, "Applications and limitations of museum data for conservation and ecology, with particular attention to species distribution models," Progress in Physical Geography, vol. 34, p. 3–22, 2010.

[78] I. Vaughan and S. J. Ormerod, "Improving the quality of distribution models for conservation by addressing shortcomings in the field collection of training data," Conservation Biology, vol. 17, pp. 1601-1611, 2003.

[79] S. A. K. Hammouda, A study of vegetation and land use in the western Mediterranean desert of Egypt. (Doctoral dissertation), Alexandria: Alexandria University, 1988, p. 194.

[80] M. A. Ayyad, "Vegetation and environment of the western Mediterranean coastal land of Egypt: The habitat of sand dunes," Journal of Ecology, vol. 61, pp. 509-523, 1973.

[81] M. A. Ayyad and M. Y. Ammar, "Relationship between Local physiographic variations and the distribution of common Mediterranean desert species," Vegetatio, vol. 27, pp. 163-176, 1973.

[82] M. A. Ayyad and R. El-Ghareeb, "Microvariations in edaphic factors and species distribution in a Mediterranean salt desert," Oikos, vol. 23, pp. 125-131, 1972.

[83] M. A. Ayyad and R. E. M. El-Ghareeb, "Salt marsh vegetation of the western Mediterranean desert of Egypt," Vegetatio, vol. 49, pp. 3-19, 1982.

[84] M. A. Ayyad and M. Y. Ammar, "Vegetation and environment of the western Mediterranean coastal land of Egypt: II. The habitat of inland ridges," Journal of Ecology, vol. 62, pp. 439-456, 1974.

[85] ROSELT/OSS, "El Omayed ROSELT/OSS Observatory," 2005.

[86] B. B. Salem, "Biosphere reserves on North-Western Egyptian coast, a site for monitoring biodiversity and integrated water management," in Developments in Water Science, vol. 50, A. S. Alsharhan and W. Wood, Eds., Elsevier, 2003, pp. 119-128.

[87] J. Franklin, "Predicting the distribution of shrub species in southern California from climate and terrain-derived variables," Journal of Vegetation Science, vol. 9, pp. 733-748, 1998.

[88] H. R. Akçakaya, M. A. Mccarthy and J. L. Pearce, "Linking landscape data with population viability analysis: Management options for the

helmeted Lichenostomus melanops cassidix," Biological Conservation, vol. 73, p. 169–176, 1995.

[89] H. R. Akçakaya, "Linking population-level risk assessment with landscape and habitat models," The Science of the Total Environment, vol. 274, pp. 283-291, 2001.

[90] A. Guisan and J. Theurillat, "Equilibrium modeling of alpine plant distribution: how far can we go?," Phytocoenologia, vol. 30, p. 353–384, 2000.

[91] C. Peppler-Lisbach and B. Schröder, "Predicting the species composition of Nardus stricta communities by logistic regression modeling," Journal of Vegetation Science, vol. 15, p. 623–634, 2004.

[92] C. D. Thomas, A. Cameron, R. E. Green, M. Bakkenes, L. J. Beaumont, Y. C. Collingham and e. al., "Extinction risk from climate change," Nature, vol. 427, pp. 145-148, 2004.

[93] S. M. McMahon, S. P. Harrison, W. S. Armbruster, P. J. Bartlein, C. M. Beale, M. E. Edwards, J. Kattge and e. al., "Improving assessment and modelling of climate change impacts on global terrestrial biodiversity," Trends in Ecology and Evolution, vol. 26, p. 249–59, 2011.

[94] P. G. Jones, P. K. Thornton and J. Heinke, "Generating characteristic daily weather data using downscaled climate model data from the IPCC ' s Fourth Assessment," 2009.

[95] P. G. Jones and P. K. Thornton, "Generating downscaled weather data from a suite of climate models for agricultural modelling applications," Agricultural Systems, vol. 114, p. 1–5, 2013.

Solitons and the new renewable energy approach

Mahmoud AKDI [1], Moulay Brahim SEDRA [2]
[1] LHESIR, F S K, Ibn Toufail University Kenitra, Morocco,
E-mail address: makerase@gmail.com

[2] LHESIR, F S K, Ibn Toufail University Kenitra, Morocco,
[2] ENSAH, Mohammed First University, Al Hoceima, Morocco
E-mail address: sedramyb@gmail.com

***Abstract* -** This article aims at deepening research on the new renewable energy production from the dams reservoir. Coupled to the solitary waves, the wind generated waves present an attractive natural phenomenon that deserves to be emphasized. The Adomain numerical method is used to model the practical observation regarding the soliton propagation. The actual cases contained in this document provide an illustration of the given principals.

***Keywords* -** Wind genrated waves; solitary waves; Kd-V equation; Adomian method; dams.

I. CONTEXT PRESENTATION

As mentioned in [1], a new concept of renewable energy generation was presented. The main idea consists of operating the wind generated waves in order to produce an electrical energy. The researchers recall that, based on practical observation of several dams, four steps distinguishing this phenomenon can be identified:

Stagnated water: represents the surface of water in the state of stagnation. No movement is noted at this area.

Wind gusts: transition step in which the wind is blowing in gusts on the surface of water;
Wind generated wave: the surface of water is deformed. Generation of waves due to action of wind on the water is assisted;

Wave propagation: the waves so generated are transported away from their creation zone. This distance is considered important compared to the length of the wind generated wave.
All the above steps are presented schematically on Fig. 1.

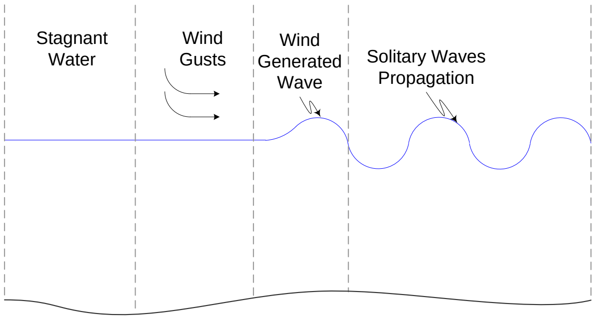

Fig .1. Steps of the phenomenon observed.

Through [1], the researchers were able to establish the physical model governing the creation of the wind-generated waves. In the present document, the researchers will focus more precisely on the fourth step, which consists of wave propagation. The range of propagation of the above waves shows that they can't be qualified as standard ones. As specified on the aforementioned figure, it comes of the solitary wave.

Actually, the solitary wave propagates in nonlinear and dispersive environment. It has localized energy in space and is extremely stable in the presence of disturbances. It moves without changing form or characteristics, and this explains the fact that it is relatively easy to observe in nature, such as in our case.
Hence, the weakly nonlinear Kd-V type theories allow us to elucidate the essential features of these observations. They have the advantage of providing modeling of wave evolution with a reduced wave equation [2].

II. SOLITARY WAVES AND THE KD-V EQUATION

The researchers suggest defining the following, as represented in Fig. 2:

- d: the average depth of the water relative to the free stagnant surface;
- H: the amplitude of the deformation of the surface of water;
- L: longitudinal scale representing a characteristic length of the deformation;
- l: a characteristic width;
- c: a characteristic speed;
- $h(x,y)$: presenting the water depth relative to the free stagnant surface;
- $\vec{V}(x,y,z,t) = \begin{bmatrix} V_x \\ V_y \\ V_z \end{bmatrix}$: presenting the fluid velocity;
- $p(x,y,z,t)$: presenting pressure minus the hydrostatic pressure, devised by the density;
- $u(x,y,t)$: presenting the deformed water elevation relative to the free stagnant surface.

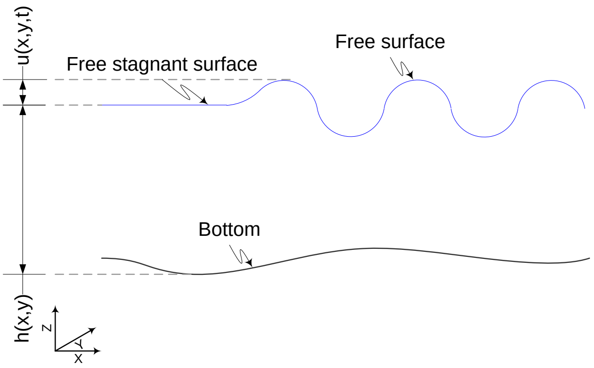

Fig .2. Convention of the characteristic variables of the water deformation.

The fundamental equations (Basic Law of Continuity and Dynamics), constituting the Navier Stokes equations give:

$$\begin{cases} \dfrac{\partial V_x}{\partial x} + \dfrac{\partial V_y}{\partial y} + \dfrac{\partial V_z}{\partial z} = 0 \\ \dfrac{d\vec{V}}{dx} + \overrightarrow{\nabla p} = 0 \end{cases}, \qquad (1)$$

with the following boundary conditions:

$$\begin{cases} V_z = \dfrac{du}{dt}, \qquad p = gu \\ V_z + V_x . \dfrac{\partial h}{\partial x} + V_y . \dfrac{\partial h}{\partial y} = 0 \end{cases} \qquad (2)$$

representing conditions respectively at the free surface and the tangent speed at the bottom and with $p = p_n/\rho + gz$, (p_n being the total pressure).

Introducing the following dimensionless variables:

$$x = \lambda . x', \;\; y = l . y', \;\; z = d . z', \;\; t = \frac{\lambda . t'}{c}, \;\; u = H . u',$$
$$h = d . h', \;\; V_x = \frac{cH}{d} . V_x', \;\; V_y = \frac{cH\lambda}{dl} . V_y', \;\; V_z = \frac{cH}{\lambda} . V_z', \;\; p = Hgp'.$$

where H is the amplitude, λ is a characteristic length, c is a characteristic velocity, d is the average depth of the water column and l is a characteristic length along the axis y.

For the rest and to simplify editing equations, the researchers rewrite the system of Navier-Stokes equations using dimensionless variables without using « ´», namely:

$$\begin{cases} \dfrac{\partial V_x}{\partial x} + \gamma \dfrac{\partial V_y}{\partial y} + \dfrac{\partial V_z}{\partial z} = 0 \\ \dfrac{\partial V_x}{\partial t} + c_0^2 \dfrac{\partial p}{\partial x} + \alpha \left(V_x \dfrac{\partial V_x}{\partial x} + \gamma V_y \dfrac{\partial V_x}{\partial y} + V_z \dfrac{\partial V_x}{\partial z} \right) = 0 \\ \dfrac{\partial V_y}{\partial t} + c_0^2 \dfrac{\partial p}{\partial y} + \alpha \left(V_x \dfrac{\partial V_y}{\partial x} + \gamma V_y \dfrac{\partial V_y}{\partial y} + V_z \dfrac{\partial V_y}{\partial z} \right) = 0 \\ \beta \dfrac{\partial V_x}{\partial t} + c_0^2 \dfrac{\partial p}{\partial z} + \alpha\beta \left(V_x \dfrac{\partial V_z}{\partial x} + \gamma V_y \dfrac{\partial V_z}{\partial y} + V_z \dfrac{\partial V_z}{\partial z} \right) = 0 \end{cases}, (3)$$

with the following boundary conditions:

$$\begin{cases} V_z = \dfrac{\partial u}{\partial t} + \alpha \left(V_x \dfrac{\partial u}{\partial x} + \gamma V_y \dfrac{\partial u}{\partial y} \right), \;\; p = u \;\; \text{for } z = \alpha u \\ V_z + V_x \dfrac{\partial h}{\partial x} + \gamma V_y \dfrac{\partial h}{\partial y} = 0 \;\; \text{pour } z = -h \end{cases} ; \; (4)$$

and :

$$\alpha = \frac{H}{d}, \;\; \beta = \frac{d^2}{\lambda^2}, \;\; c_0^2 = \frac{gd}{c^2}, \;\; \gamma = \frac{\lambda^2}{l^2}.$$

As part of the previous approximation $H \ll d \ll L$, recovered in the second-order, the researchers deduce that $\beta^2 \ll 1$ and $\alpha\beta \ll 1$.

Thus, they arrive at the Boussinesq system:

$$\begin{cases} \dfrac{\partial u}{\partial t} + \dfrac{\partial}{\partial x}\left[(\alpha u + h) \widetilde{V_x} \right] + \gamma \dfrac{\partial}{\partial y}\left[(\alpha u + h) \widetilde{V_y} \right] = 0 \\ \dfrac{\partial \widetilde{V_x}}{\partial t} + c_0^2 \dfrac{\partial u}{\partial x} + \alpha \left(\widetilde{V_x} \dfrac{\partial \widetilde{V_x}}{\partial x} + \gamma \widetilde{V_y} \dfrac{\partial \widetilde{V_x}}{\partial y} \right) + \dfrac{1}{3} \beta h \dfrac{\partial^3 u}{\partial t^2 \, \partial x} = 0; \\ \dfrac{\partial \widetilde{V_y}}{\partial t} + c_0^2 \dfrac{\partial u}{\partial y} + \alpha \left(\widetilde{V_x} \dfrac{\partial \widetilde{V_y}}{\partial x} + \gamma \widetilde{V_y} \dfrac{\partial \widetilde{V_y}}{\partial y} \right) + \dfrac{1}{3} \beta h \dfrac{\partial^3 u}{\partial t^2 \, \partial y} = 0 \end{cases} \; (5)$$

with :

$$\widetilde{V_x} = \frac{1}{h}\int_{-h}^{0} V_x . dz,\ \widetilde{V_y} = \frac{1}{h}\int_{-h}^{0} V_y . dz\ . \qquad (6)$$

If the researchers focus on solutions $\frac{\partial u}{\partial \tau} + \frac{\partial u}{\partial x} = \ominus (\alpha, \beta, \gamma)$, with $\tau = c_0 . t$, for which they accept that solutions spread to the positive x, then they deduce the Kd-V equation for a two-dimensional flow:

$$\frac{\partial}{\partial x}\left(\frac{\partial u}{\partial \tau} + \frac{\partial u}{\partial x} + \frac{3}{2}\alpha u \frac{\partial u}{\partial x} + \frac{1}{6}\beta \frac{\partial^3 u}{\partial x^3}\right) + \frac{\gamma}{2}\frac{\partial^2 u}{\partial y^2} = 0. \qquad (7)$$

In the one-dimensional case, either to $\gamma = 0$, the same equation becomes:

$$\frac{\partial u}{\partial \tau} + \left(1 + \frac{3}{2}\alpha\right) u \frac{\partial u}{\partial x} + \frac{1}{6}\beta \frac{\partial^3 u}{\partial x^3} = 0. \qquad (8)$$

There exist many variants of the Kd-V equation depending on the case study. In a configuration similar to ours, the above equation can take the following form [2]:

$$\eta_t + (c_0 + \alpha_1 \eta + \alpha_2 \eta^2)\eta_x + \beta_1 \eta_{xxx} = 0, \qquad (9)$$

where $\eta(x, t)$ refers to the wave amplitude related to the isopycnal vertical displacement. The coefficients α_1, α_2, and β_1 are functions of the steady background stratification and shear through the linear eigenmode (vertical structure function) of interest. The linear phase speed c_0 is the eigenvalue of the Sturm-Louiville problem for the eigenmode.

The researchers can deduce from the preceding data that handling such equation to get analytic solution cannot be considered as an affordable issue.

The situation can be more complicated when the boundary conditions change due to location and intrinsic site parameters. This is why the researchers present a numerical method in order to insure resolution of the above equation while complying with the efficiency required.

III. THE ADOMIAN DECOMPOSITION METHOD APPLIED TO THE KD-V EQUATION

Consider the Kd-V equation as follows:

$$\frac{\partial u}{\partial t} + 6u\frac{\partial u}{\partial x} + \frac{\partial^3 u}{\partial x^3} = 0,\quad u(x, 0) = f(x) \qquad (10)$$

which can be rewritten as follows:

$$\frac{\partial u}{\partial t} = -Ru - 6N(u),\ \ u(x, 0) = f(x) \qquad (11)$$

where $R = \partial^3/\partial x^3$ represents the linear operator of the Kd-V equation and $N(u) = u\, \partial u/\partial x$ is the non-linear function. According to the ADM, the solution is expressed by:

$$u(x, t) = \sum_{n=0}^{\infty} u_n(x, t), \qquad (12)$$

and the non-linear part:

$$N(u) = \sum_{n=0}^{\infty} A_n, \qquad (13)$$

with:

$$A_n = \frac{1}{n!}\frac{d^n}{d\lambda^n}\left[N\left(\sum_{i=0}^{\infty} \lambda^i u_i\right)\right]_{\lambda=0}, \qquad (14)$$

By integrating with respect to time and using the initial conditions the researchers have:

$$u(x, t) = f(x) - \int_0^t [Lu + 6N(u)]ds. \qquad (15)$$

So:

$$u(x,t) = f(x) - \int_0^t \left[L\left(\sum_{n=0}^{\infty} u_n(x,s)\right) + 6\sum_{n=0}^{\infty} A_n \right] ds. \quad (16)$$

For the KdV equation, the Adomian polynomials can be expressed as follows:

$$A_n = \sum_{i=0}^{n} u_i \frac{\partial u_{n-i}}{\partial x}. \quad (17)$$

This allows the researchers to deduce $u_n(x,t)$, namely:

$$\begin{cases} u_0(x,t) = f(x) \\ u_{n+1}(x,t) = -\int_0^t [Ru_n + A_n] ds, \quad n \geq 0 \end{cases} \quad (18)$$

with the following initials conditions:

$$u(x,0) = \frac{1}{2}\operatorname{sech}^2\left(\frac{x}{2}\right). \quad (19)$$

The researchers proceed in the following to compute $A_n(x,t)$ and $u_n(x,t)$ for $n \in [\![0,10]\!]$ and try to determine the approximate solution $\tilde{U}_n(x,t)$ using the following formula:

$$\tilde{U}_n(x,t) = \sum_{i=0}^{n} U_i(x,t) \quad (20)$$

$$= f(x) - \int_0^t \left[L\left(\sum_{i=0}^{n} u_i(x,s)\right) + 6\sum_{i=0}^{n} A_i \right] ds. \quad (21)$$

The numerical studies can be effectively elaborated by the use of this computational method. Once created, the researchers can predict the evolution of the solitary waves with respect to the spatial and time variables. The following figure gives an idea about the numerical calculation obtained [3] and [4]. There exist other numerical methods that can also be used depending on their calculation effectiveness [5] and [6].

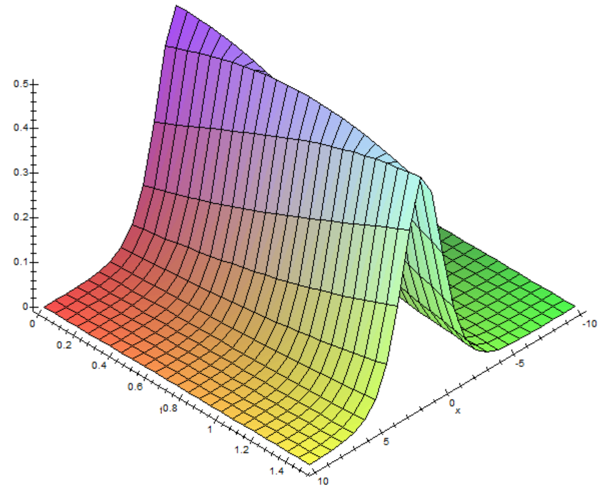

Fig .3. Numerical solution of the Kd-V equation using the ADM method.

IV. INTRINSIC CONDITIONS FAVORING THE EXPLOITATION OF SOLITARY WAVES

The efficiency of the new renewable energy production approach is closely related to the implementation of site conditions. As presented in [7] several parameters are taken in consideration in the site selection. The researchers would like to mention those with critical issues as follows:

- The wind speed constitutes one of the main parameters to take in consideration. The wind speed, the height of the wind generated waves, the swept area and the generated power all together evolve according to the same trend.
- The second one is the wind direction. Indeed, to get optimal conditions of the power extraction, one needs to have both: a regular and a dominant wind direction.

- The third one is the area of the water surface. It allows increasing the recovery of energy during wave propagation.

- Another point is the availability of hydroelectricity plant in order to benefit from the direct injection of the generated electrical power in the network.

Another advantage of this new approach, in addition to those presented previously, lies in benefits due to the intrinsic features of the site implementation. In the following, the researchers will introduce two particular cases illustrating this fact.

A. Topography of the dam location

The speed of the wind is further appreciated in the case of existence of a dominant wind direction. In this sense, the topography of the dam site can filter the wind direction so as to keep a dominant direction. Thus there is consistency in the direction of the wind generated waves.The dam of Ouirgane located in the Atlas Mountains, near of Marrakech city (about 66 Km), reflects this principle. As illustrated in Fig. 4, the dam reservoir along the thalweg.

Fig .4. Satellite image of Ouirgane dam (31°11'23.3"N 8°05'16.5"W) with indication of the wind dominant direction.

Fig. 5 shows that the watersheds elevation constitutes a natural filter with respect to the wind direction: only the wind blowing in a direction parallel to the crest line of the mountains contributes to the creation of the wind generated waves.

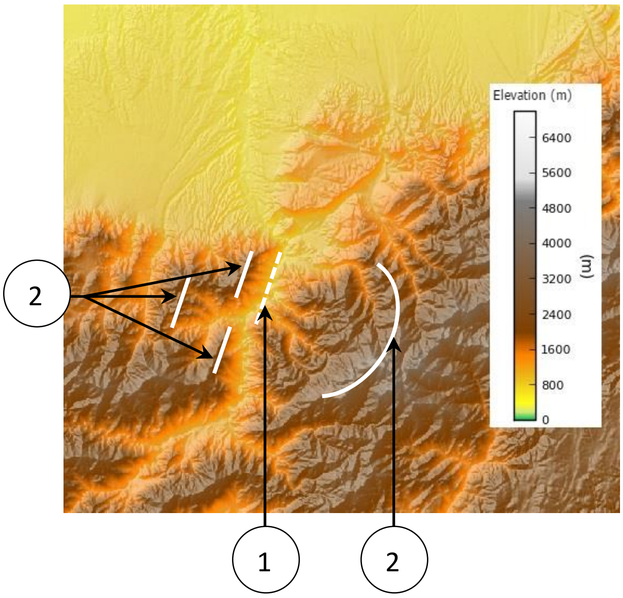

Fig .5. Elevation map at the Ouirgane dam. (1) Refer to the thalweg axis and (2) refer to crest lines of the mountains surrounding the dam reservoir.

Even if the wind direction distribution relating to this region is dispersed among several directions (Cf. Fig. 6), the naturel filter due to topographic feature isolates only the NNE as a dominant wind direction.

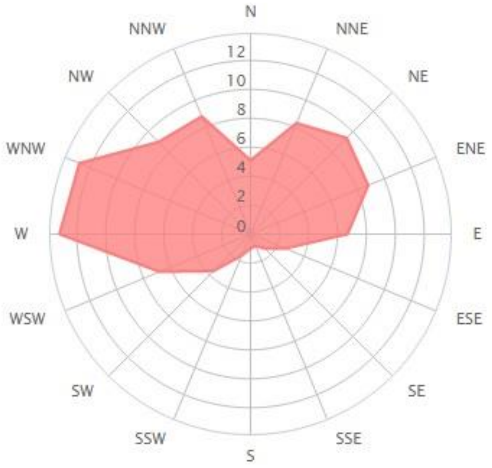

Fig .6. Annual wind direction distribution at Marrakech-Menara airport.

The particular interest reached through this configuration is that the solitary waves once generated continue to propagate along the dam reservoir and do not break. Thus the energy extricated can be recovered a multitude times.

B. Dam wall orientation and solitary waves

We detailed at the beginning of this document the different aspects of the solitary waves, in order to use their application in the new renewable energy concept. The propagation of these waves further away from their emplacement generation offer significant opportunities. This performance can be improved in the case where the dam wall has an orientation perpendicular to the solitary waves propagation as shown in Fig. 7.

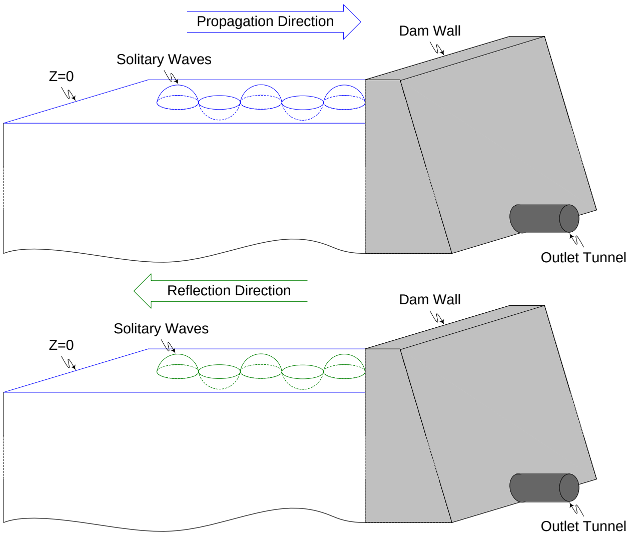

Fig .7. Propagation and reflection of the solitary waves against the dam wall.

For a phenomenon happening a single time, alias the wind generated waves, the swept area is duplicated. This means that the efficiency of any unitary conversion installation responding to this condition will double. The electrical production will occur in the first propagation step and also in the second one after dam wall reflection. Allal Al Fassi dam (about 52 km from Fes city) presented in Fig. 8 gives an appropriate illustration concerning this case. Effectively, as shown in the wind direction distribution in Fig. 9, the dominant wind direction NW is perpendicular to the aforementioned dam wall.

Fig .8. Satellite imagery of Allal Al Fassi dam (33°55'53.0"N 4°40'37.9"W).

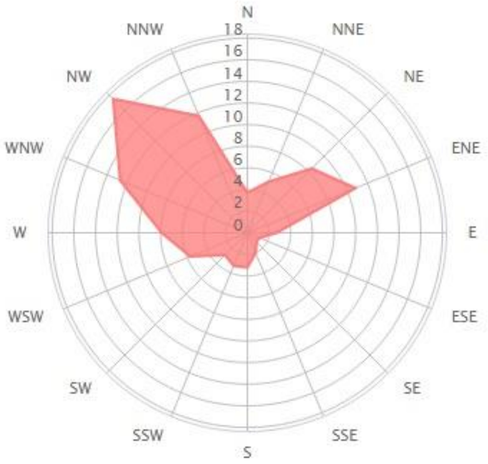

Fig .9. Annual wind direction distribution at Fes-Saïss airport.

V. CONCLUSIONS

In this paper the effect of the combination of the wind generated waves and the solitary waves was proven. Once created under the particular conditions defined, the wind generated waves are transported away from their creation area via solitons. Based on this, the swept area increases significantly and the propagation waves trajectory in dams reservoir becomes longer.

Taking in consideration two particular cases, favorable topographical dam location and the well dam wall orientation, the above performance is further enhanced.

REFERENCES

[1] M. Akdi, M. B. Sedra. (2015). New Approach for Renewable Energy Production from Dams. International Journal of Sustainable and Green Energy. Special Issue: Wind-Generated Waves, 2D Integrable KdV Hierarchies and Solitons. [Online]. 4(3-2), pp. 1-5. Available: http://article.sciencepublishinggroup.com/pdf/10.11648.j.ijrse.s.2015040302.11.pdf

[2] Karl R. Helfrich, W. Kendall Melville. (2006). Long Nonlinear Internal Waves. The Annual Review of Fluid Mechanic. [Online]. 38, pp. 395–425. Available: http://darchive.mbl.edu/bitstream/handle/1912/651/Helfrich%20annurev.fluid.38.050304.pdf?sequence=1

[3] M. Akdi, M. B. Sedra. (2013). Numerical KDV Equation by the Adomian Decomposition Method. American Journal of Modern Physics. [Online]. 2(3), pp. 111-115. Available: http://article.sciencepublishinggroup.com/pdf/10.11648.j.ajmp.20130203.13.pdf

[4] M. Akdi, M. B. Sedra. (2013). Comments on the Adomian Decomposition Methods Applied to the KdV Equation. Applied and Computational Mathematics. [Online]. 2(6), pp. 137-142. Available: http://article.sciencepublishinggroup.com/pdf/10.11648.j.acm.20130206.15.pdf

[5] M. Akdi, M. B. Sedra. (2013). Numerical Simulation of KdV equation. Advanced Studies In Theoretical Physics. [Online]. 7(9-12), pp. 407-418. Available: http://www.m-hikari.com/astp/astp2013/astp9-12-2013/sedraASTP9-12-2013.pdf

[6] M. Akdi. (2013). Study of solitary waves: results of resolution by numerical methods of the Korteweg-de Vries equation and simulation of the fluid flow. PhD Thesis.

[7] M. Akdi, M. B. Sedra. (2015). Prospective Study: Choice of the Potential Sites Intended for the New Renewable Energy Approach. International Journal of Sustainable and Green Energy. Special Issue:Wind-Generated Waves, 2D Integrable KdV Hierarchies and Solitons. [Online]. 4(3-2), pp. 6-9. Available: http://article.sciencepublishinggroup.com/pdf/10.11648.j.ijrse.s.2015040302.12.pdf

Journal of Renewable Energy and Sustainable Development (RESD) Volume 1, Issue 2, December 2015 - ISSN 2356-8569

THE BOOST CONVERTER – REVISITED

B. W. Williams, T. C. Lim
Department of Electronic and Electrical Engineering, University of Strathclyde, Glasgow G1 1XW, UK

Abstract - The dc-to-dc boost converter is a single-switch, single-inductor, switching circuit used to efficiently transform energy from one dc voltage level to a greater voltage level of the same relative polarity. For a specific resistive load range, as the duty cycle decreases, the boost converter inductor enters a discontinuous current mode of operation - the output load current having decreased to a definable level. This paper analyses the fact that a further reduction of load current, as the duty cycle decreases towards zero, will always result in the re-emergence of a continuous inductor current condition. Further, at the other load extreme, high-current, progressively for increasing load current, starting at low duty cycle conditions, the minimum inductor current always increases from a fixed normalised current level, for a specific load range. These and other hitherto unexplored boost converter properties are analysed and verified mathematically and with PSpice simulations.

Keywords - switched mode power supplies, smps, boost converter, dc to dc converters***.***

I. INTRODUCTION

A. Species Distribution Models (SDMs)

The three common non-isolated, single-switch, single-inductor, dc-to-dc converters (switch mode power supplies - smps) are

- the forward (or buck or step-down) converter;
- the step-up (or boost) converter; and
- the inverting step-up/down (or buck-boost) converter.

Each of these converters operates on the principle of taking input dc supply energy, temporarily storing that energy in the magnetic field of an inductor, then that energy is diverted to the load, which can be at a potential and polarity different to the input energy source emf voltage.

This paper is specifically concerned with the boost converter shown in figure 1a and extends the analyses and understanding of its basic traditionally accepted operating modes and properties. The background theory is briefly presented to establish existing boost converter operational interpretation and to define the necessary concepts and parameters.

The boost converter in its basic form converters dc voltage source energy to a higher voltage level, using switch mode (hard or soft) techniques (namely, the switch is either cut-off or fully on - saturated). The boost converter is used to step up the low output voltage of PV arrays to a voltage level commensurate with inverter link voltages suitable for transformerless ac grid interfacing [1]. Because of its continuous input current characteristic the boost converter is used extensively for extracting sinusoidal current at controllable power factor from wind turbine ac generators [2].

As shown in figure 1b, operation and the output voltage are characterised by the switch on-time duty cycle δ, and analysis is centred on the inductor current iL and inductor voltage vL, as shown in figures 1c and 1d. Specifically, in steady-state, analysis is based on the inductor satisfying Faraday's equation

$$v_L = L\frac{di_L}{dt}$$

Steady-state theoretical analysis assumes zero switch and diode losses, an infinite output capacitance C, and zero source and inductor resistance; then the switch on-state and off-state currents created Kirchhoff loops yield

$$L\,\Delta i_L = E_i t_T = v_o t_D \qquad \text{(V.s)} \qquad (1)$$

which after rearranging the last equality, gives the traditional boost converter voltage and current transfer function expression

$$\frac{v_o}{E_i} = \frac{\bar{I}_i}{\bar{I}_o} = \frac{1}{1-\delta} \qquad \text{(pu)} \qquad (2)$$

where, because of zero converter losses, the output power is equal to the input power, namely,

$E_i\bar{I}_i = v_o\bar{I}_o$ - termed power invariance. This expression, equation (2), assumes continuous current in the inductor when the switch is off, during the period tD, such that $t_T + t_D = \tau$, where the steady-state switching frequency is $f_s = 1/\tau$ and the normalised switch on-period is $\delta = t_T/\tau$.

Equation (2) highlights that the relationship between the input and output voltages (and currents) is independent of circuit components *L, C,* and the switching frequency f_s: being dependant only on the switch on-state duty cycle *δ,* provided inductor current flows throughout the whole switch off-state period, t_D, normalised as $\delta_D = t_D / \tau = 1 - \delta$. This inductor current condition is termed *continuous conduction*. A continuous current requirement is highlighted when considering the circuit energy transfer balance between the input and the output:

$$E_i\bar{I}_o + \tfrac{1}{2}L\left(\hat{i}_L^2 - \check{i}_L^2\right)/\tau = v_o\bar{I}_o$$
$$(1-\delta)E_i\bar{I}_i + L\bar{I}_L\Delta i_L/\tau = v_o\bar{I}_o \qquad \text{(W)} \qquad (3)$$

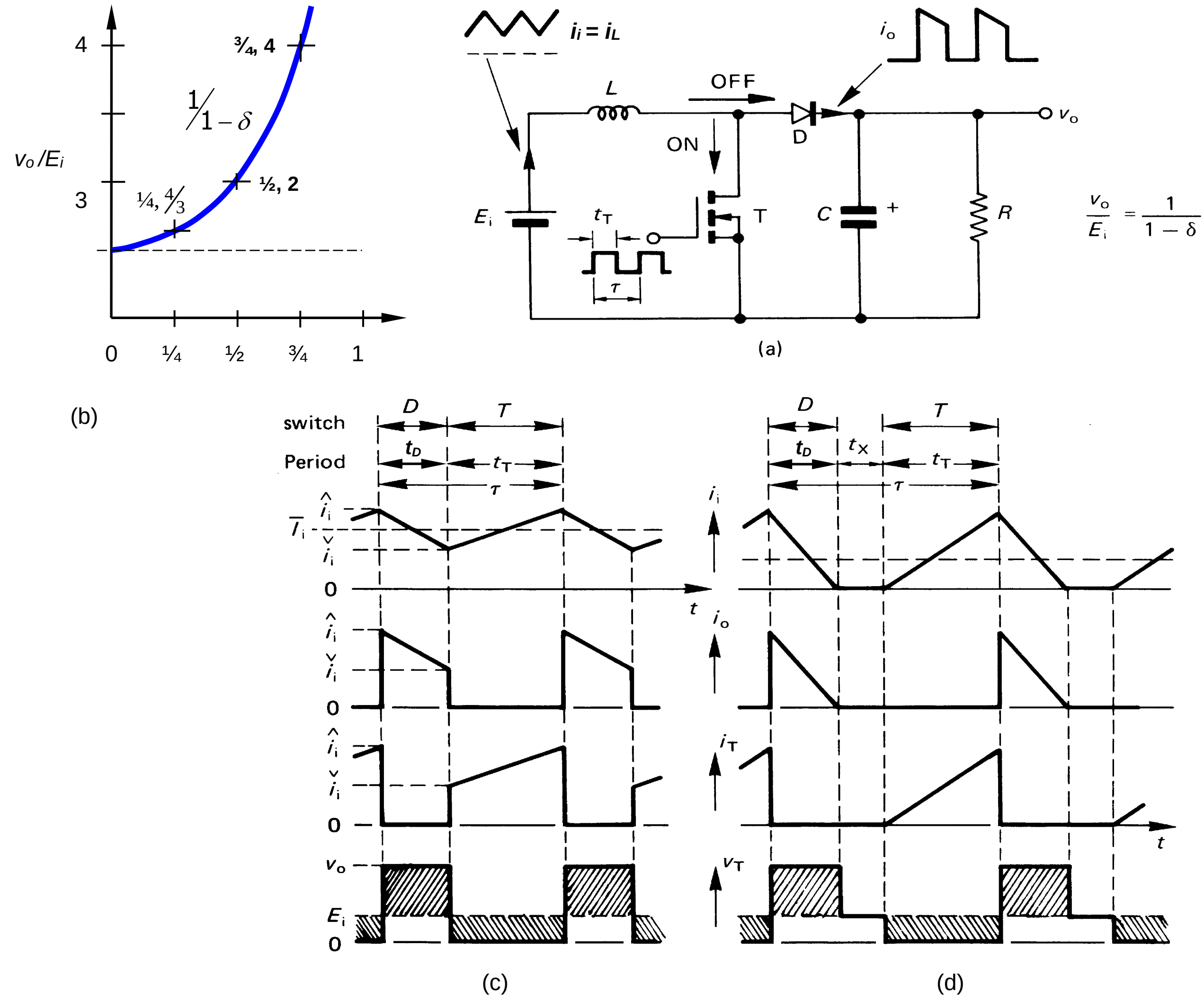

Fig .1. Non-isolated, step-up, flyback converter (boost converter) where vo ≥ Ei: (a) circuit diagram; (b) voltage transfer function dependence on duty cycle δ; (c) waveforms for continuous input (inductor) current; and (d) waveforms for discontinuous input (inductor) current.

The last term in (3) is the continuous power consumed by the load, while the second term is the energy (whence power) transferred from the inductor to the load. The first term is the energy derived from the source Ei delivered through the inductor, while the inductor is also transferring energy to the load (when the switch is off). A similar energy transfer mechanism occurs with the step-up ac auto-transformer. In using the factor 1 - δ in equation (3), it is assumed that energy is transferred to the load from the supply, during the whole period the switch is off, that is, continuous inductor current. Since the inductor is in series with the input, the input current terms are interchangeable with the corresponding inductor current terms, for example, Assuming power from the emf source E$_i$ is equal to power delivered to the load, power invariance, then equation (3) reduces to equation (2), or in a rearranged form

$$E_i + \delta v_o = v_o \qquad \text{(V)} \qquad (4)$$

In this form, it can be seen that the output voltage v_o has a component due the input dc supply E_i, and a boost component proportional to the switch on-state duty cycle δ, illustrating that the output voltage magnitude v_o is equal to or greater than the input voltage (emf) magnitude E_i.

Traditional theory considers when the load energy requirement falls below that level necessitating the inductor carry current during the whole period when the switch is off: termed *discontinuous inductor current*. Three sequential cycle stages (rather than two) now occur during the interval τ:

- the period when the switch conducts, t_T, normalised as $\delta = t_T / \tau$
- the period when the inductor and diode conduct, t_D, normalised as $\delta_D = t_D / \tau$
- the period t_x is when the inductor and diode cease to conduct before $t = \tau$; normalised as $\delta_x = t_x / \tau$

such that $t_T + t_D + t_x = \tau$ or when normalised $\delta + \delta_D + \delta_x = 1$, as shown in figure 1d.

From equation (1), using

$$\hat{i}_L = \frac{E_i t_T}{L} = \frac{E_i \delta \tau}{L} \qquad (5)$$

where $\check{i}_L = 0$ when the switch is turned on then

$$\bar{I}_L - \bar{I}_o = ½\delta \hat{i}_L = ½\delta \frac{E_i \delta \tau}{L}$$

Assuming power invariance and substituting $\bar{I}_L = \bar{I}_i$

$$\bar{I}_o (\frac{v_o}{E_i} - 1) = ½\delta \frac{E_i \delta \tau}{L}$$

that is, after various $E_i \bar{I}_i = v_o \bar{I}_o$ substitutions:

$$\frac{v_o}{E_i} = 1 + \frac{E_i \tau \delta^2}{2L\bar{I}_o} = 1 + \frac{v_o \tau \delta^2}{2L\bar{I}_i} = \frac{1}{1 - \dfrac{E_i \tau \delta^2}{2L\bar{I}_i}} \qquad (6)$$

Note that power invariance is valid for all inductor current conditions, namely, both continuous and discontinuous currents – during steady-state operation. But equation (6) is only valid for discontinuous inductor current, and its boundary with continuous inductor current operation. Equation (6) is consistent with power invariance, where, for discontinuous current, equation (3) becomes

$$v_o \bar{I}_o = E_i \bar{I}_o + ½L \hat{i}_L^2 / \tau \qquad (7)$$

Operational interest centres on the boundary conditions between continuous and discontinuous inductor current, where the basic voltage and current transfer function in (2) remains valid. On the verge of continuous conduction, any of the equations in (6) rearranged give the boundary critical output current

$$\bar{I}_{o\,critical} = \frac{E_i}{2L} \tau \delta (1 - \delta) \qquad (8)$$

Using $v_o = \bar{I}_o R$ and equation (2), the critical boundary load resistance $R_{critical}$ is given by

$$R_{critical} = \frac{v_o}{\bar{I}_{o\,critical}} = \frac{2L}{\tau \delta (1-\delta)^2} = \frac{v_o}{E_i} \times \frac{2L}{\tau \delta (1-\delta)} \qquad (\Omega) \quad (9)$$

A fact not previously specifically stated in the literature, is that the last equality in this critical resistance expression is common to all three single-inductor, single-switch smps (buck, boost and buck-boost):

$$R_{critical} = \frac{v_o}{E_i} \times \frac{2L}{\tau \delta (1-\delta)} \qquad (10)$$

which, for the boost converter, after differentiating the first identity in equation (9) and equating to zero, giving $\delta = ⅓$, has a minimum value of

$$\check{R}_{critical} = \frac{27}{2}\times\frac{L}{\tau} \tag{11}$$

when $\delta = ⅓$ and $v_o = 1.5\times E_i$, which corresponds to a maximum critical current of

$$\bar{I}_{o\,critical} = \frac{v_o}{\check{R}_{critical}} = \frac{\tau v_o}{2L}\times\frac{4}{27} \quad \text{(A)} \tag{12}$$

At other output voltages, when $\delta \neq ⅓$, lower currents (larger load resistance, $> \check{R}_{critical}$) can be tolerated before the onset of discontinuous inductor current. Alternatively, equation (13) shows that critical resistance is inversely proportional to inductor ripple current. That is, a large continuous inductor ripple current and low duty cycle undesirably enhance the early onset of inductor discontinuous ripple current.

$$R_{critical} = \frac{2E_i}{(1-\delta)^2\,\Delta i_L} \tag{13}$$

II. INDUCTOR ONTINUOUS/DISCONTINUOUS CURRENT BOUNDARY OPERATIONAL ANALYSIS METHODS

The expressions in equation (6) are only valid for discontinuous inductor current, and on the boundary with continuous conduction, since their derivation is based on $\check{i}_L = 0$.

Two methods are commonly employed to analyse discontinuous current conduction operation, equation (6), namely:

The voltage transfer function is normalised with respect to

- the maximum discontinuous inductor current in terms of the input current $\bar{I}_i$
- the maximum discontinuous inductor current in terms of the output current $\bar{I}_o$

where in each case the input voltage E_i and output voltage v_o are, in turn, assumed constant.

The voltage transfer function is normalised in terms of the load resistance. This involves the smps time constant *L/R*, (formed by the circuit when the switch is off), being normalised by the reciprocal of the switching frequency, namely, *τ*.

A. Normalisation in terms of the maximum discontinuous inductor current

Of the four possible *I-V* combinations that can be analysed, the case specifically considered here, by way of example, is when the output voltage v_o is assumed constant (as opposed to the input voltage, E_i) and is normalised with respect to the output current, $\hat{\bar{I}}_o$ (as opposed to the input current, $\hat{\bar{I}}_i$). This specific case ($v_o - \bar{I}_o$, effectively load resistance) is considered since it later represents the situation which best presents hitherto unexplored properties.

Consider equation (6), specifically

$$\frac{v_o}{E_i} = 1 + \frac{E_i \tau \delta^2}{2L\bar{I}_o} \tag{14}$$

which gives

$$\frac{v_o}{E_i} = 1 + \frac{\delta^2 v_o \tau}{2L\bar{I}_o} \Big/ \frac{v_o}{E_i} \tag{15}$$

At maximum discontinuous inductor current (at the boundary between continuous and discontinuous inductor current), the transfer function, equation (2) is valid, and on substitution into equation (15) gives a cubic polynomial in *δ*

$$\bar{I}_o = \frac{\tau v_o}{2L}\times\delta(1-\delta)^2 \tag{16}$$

The maximum average output current on the boundary, for a constant output voltage v_o, is found by differentiating (16) with respect to duty cycle *δ*, and equating to zero. On substituting the conditional result $\delta = ⅓$, this yields (as in equation (12))

$$\bar{I}_o = \frac{\tau v_o}{2L}\times\frac{4}{27} \text{ when } \delta = ⅓ \text{ and } \frac{v_o}{E_i} = 1½ \tag{17}$$

Normalising equation (15) with respect to the maximum discontinuous current given by (17), after isolating the voltage transfer ratio, yields

$$\left.\frac{v_o}{E_i}\right|_{v_o\ \text{constant}} = ½ + ½\sqrt{1 + 27\delta^2 \Big/ \frac{\bar{I}_o}{\hat{I}_o}} \tag{18}$$

The boundary equation between continuous and discontinuous inductor current conduction, relating the output current and duty cycle can be found by substituting the transfer function ${}^{1}\!/_{1-\delta}$, which is valid on the boundary, into (18), which yields

$$\frac{\bar{I}_o}{\bar{I}_o} = \tfrac{27}{4}\,\delta\left(1-\delta\right)^2 = \frac{\check{R}_{critical}}{R_{critical}} \tag{19}$$

Equations (14) to (19) are presented in the penultimate column of Table 1, where the results of similar analysis for the other normalised input and output voltage and current conditions, being established background, are also summarised. The table also shows rearranged boundary conditions for each variable (δ, v_o/E_i, and $\bar{I}_o/\bar{I}_o$), in terms of the other variables, as in equation (19), for example.

These normalised equations and their various rearranged forms are plotted in figures 2, 3, and 4. Each figure has four different plots, one for each of the possible normalised input and output voltage and current combination.

i. δ versus $\bar{I}/\bar{I}$ - figure 2 [3]

Figure 2 shows how, to maintain a constant output voltage, the duty cycle must decrease as the load voltage tends to increase once the discontinuous conduction region is entered. As would be expected, independent of which input or output parameter is controlled, discontinuous inductor current results in over charging the output capacitor, thus the duty cycle must be decreased to reduce the energy transferred to the load, so as to maintain the required constant output voltage. Figure 2c shows the normalised condition as per equation (17), namely a peak boundary condition of $\delta = ⅓$ at $v_o = 1.5\times E_i$. Because of power invariance, the two plots on the right in figure 2, have the identical shape, with variables interchanged appropriately.

ii. $\frac{v_o}{E_i}$ versus $\bar{I}/\bar{I}$ - figure 3 [3], [4]

Figure 3 conveys similar information to figure 2. However, figure 3 shows the more practical situation of how, for an increasing load resistance, for a given fixed duty cycle *δ,* the output voltage increases, when the load (hence input) current decreases once entering the discontinuous conduction region. Because of power invariance, the two right hand plots have the same shape. The four plots in figure 3 predict an infinite output voltage, but a finite output current as the load current decreases: for a constant duty cycle, discontinuous inductor current occurs for all currents below the critical level.

iii. $\frac{v_o}{E_i}$ versus δ - figure 4

Figure 4 affords a more informative representation of the various circuit equations. Each of the four parts of figure 4 show voltage transfer function variation with duty cycle. Each plot therefore involves the basic voltage transfer ratio curve, in the continuous current region:

$$\frac{v_o}{E_i} = \frac{1}{1-\delta}$$

The main region of concern is when the normalised current variable is less than one, in other words, when there is a possibility of discontinuous inductor current. By way of example, each graph has plotted two normalised currents of less than one, namely $\bar{I}/\bar{I} = ⅓$ and $⅔$. Both of these load current conditions introduce a region where the transfer function becomes load current dependent – discontinuous inductor current.

In the case where the input voltage E_i is constant, for loads based on the input current, the duty cycle boundary between the two modes occurs at

$$\delta = {}^{\bar{I}_i}\!\big/\!_{\bar{I}_i}$$

$$\text{where } \frac{v_o}{E_i} = \frac{1}{1-\delta^2 \,/\, {}^{\bar{I}_i}\!\big/\!_{\bar{I}_i}} \quad \text{for } \delta \le {}^{\bar{I}_i}\!\big/\!_{\bar{I}_i}$$

For loads based on the output current and constant input voltage, *E*E_i, the boundary between the two inductor current modes occurs at

$$\delta = ½ \pm ½\sqrt{1 - \frac{\bar{I}_o}{\bar{I}_o}}$$

where $\frac{V_o}{E_i} = 1 + 4\delta^2 \,/\, {}^{\bar{I}_i}\!/\!_{\bar{I}_i}$

between the two duty cycle boundary points. Again, because of power invariance this plot is the same as when the output voltage is constant, for varying input current conditions.

The remaining plot in figure 4 and its insert, is most important since it represents the mode where the output conditions are controlled, as is the usual method of using the boost converter. A region of discontinuous inductor current occurs, for duty cycle values above and below which operation returns to continuous conduction [5]. The two boundary conditions for $0 \le \delta \le 1$ are two of the roots of the cubic (see Appendix for the general expressions for roots of this cubic)

$$^{27}\!/\!_4\,\delta\left(1-\delta\right)^2 = \frac{\bar{I}_o}{\hat{I}_o} \qquad (20)$$

and the corresponding voltage transfer function is as shown in Table 2. From Table 1 the voltage transfer function is

$$\frac{V_o}{E_i} = ½\left[1 + \sqrt{1 + 27\delta^2 \,/\, \frac{\bar{I}_o}{\hat{I}_o}}\right]$$

The voltage transfer function for discontinuous inductor current is approximately linear with duty cycle over a wide range:

$$\frac{V_o}{E_i} = ½ \pm {}^{3\sqrt{3}}\!/\!_2\,\delta \,/\, \sqrt{\frac{\bar{I}_o}{\hat{I}_o}}$$

The plot shows that discontinuity commences at

$$\delta = ⅓ \text{ with } \frac{V_o}{E_i} = 1½ \text{ when } \frac{\bar{I}_o}{\hat{I}_o} = 1$$

Another rational boundary solution is

$$\delta = ⅔ \text{ and } ⅔\left(2 - \sqrt{3}\right) \text{ with } \frac{V_o}{E_i} = 3 \text{ when } \frac{\bar{I}_o}{\bar{I}_o} = ½$$

In all four cases (input/output *I-V*), the boundary conditions correspond to the appropriate vertical line $0 \le \bar{I} / \bar{I} \le 1$ boundary intersection points on the plots in figures 2 and 3.The properties of the cubic polynomial in equation (20) bare closer examination. From the Appendix, three real roots exist (discontinuous current conditions) if

$$\bar{I}_o / \bar{I}_o \left(\bar{I}_o / \bar{I}_o - 1\right) < 0$$

which is true for $0 \le \bar{I}_o / \bar{I}_o \le 1$ - the discontinuous inductor current condition. The exact roots of equation (20) in terms of the coefficients of the cubic are given in the Appendix.

The voltage transfer function can be expressed in terms of the duty cycle at the boundary of continuous inductor current. That is, from Table 1 – the third formula column, for v_o constant and the output current normalised

$$\frac{\bar{I}_o}{\hat{I}_o} = {}^{27}\!/\!_4 \times \frac{\left(\frac{V_o}{E_i} - 1\right)}{\left(\frac{V_o}{E_i}\right)^3} = {}^{27}\!/\!_4\,\delta\left(1-\delta\right)^2 \qquad (21)$$

Factorising the last equality, which produces a cubic polynomial, yields

$$\left[\left(1-\delta\right) {}^{V_o}\!/\!_{E_i} - 1\right] \times \left[\delta\left(1-\delta\right) {}^{V_o}\!/\!_{E_i}{}^2 + \delta\, {}^{V_o}\!/\!_{E_i} - 1\right] = 0 \qquad (22)$$

The first root confirms that the boundary for discontinuous conduction is

$${}^{V_o}\!/\!_{E_i} = \frac{1}{1-\delta} \qquad (23)$$

Although real roots exist to the quadratic polynomial in equation (22), for allowable duty cycle values 0≤*δ*<1, both are meaningless except other than to confirm the maximum boundary condition at $\delta = ⅓$, when ${}^{V_o}\!/\!_{E_i} = 1½$ and $\bar{I}_o / \bar{I}_o = 1$.

Table 1. Step-up converter transfer functions with constant input voltage, E_i, and constant output voltage, v_o, with respect to $\bar{I}_o$ and $\bar{I}_i$

continuous inductor current, equation (2)	$\frac{v_o}{E_i} = \frac{1}{1-\delta}$ $\qquad$ $\delta = \frac{\frac{v_o}{E_i} - 1}{\frac{v_o}{E_i}}$			
	E_i constant		v_o constant	
	$\bar{I}_o$	$\bar{I}_i$	$\bar{I}_o$	$\bar{I}_i$
discontinuous inductor current equation (6)	$\frac{v_o}{E_i} = 1 + \frac{\delta^2 E_i \tau}{2L\bar{I}_o}$	$\frac{v_o}{E_i} = \frac{1}{1 - \frac{E_i \tau \delta^2}{2L\bar{I}_i}}$	$\frac{v_o}{E_i} = \frac{1}{1 - \frac{E_i \tau \delta^2}{2L\bar{I}_i}}$	$\frac{v_o}{E_i} = 1 + \frac{\delta^2 v_o \tau}{2L\bar{I}_i}$
Normalised wrt $\hat{I}$	$\frac{v_o}{E_i} = 1 + 4\delta^2 / \frac{\bar{I}_o}{\hat{I}_o}$ where $\hat{I}_o = \frac{E_i \tau}{8L}$	$\frac{v_o}{E_i} = \frac{1}{1 - \delta^2 / \left(\frac{\bar{I}_i}{\hat{I}_i}\right)}$ where $\hat{I}_i = \frac{E_i \tau}{2L}$	$\frac{v_o}{E_i} = \frac{1 + \sqrt{1 + 27\delta^2 / \frac{\bar{I}_o}{\hat{I}_o}}}{2}$ where $\hat{I}_o = \frac{4}{27} \times \frac{v_o \tau}{2L}$	$\frac{v_o}{E_i} = 1 + 4\delta^2 / \frac{\bar{I}_i}{\hat{I}_i}$ where $\hat{I}_i = \left\lvert \frac{v_o \tau}{8L} \right\rvert$
$\bar{I} / \hat{I} = 1\,\text{pu}$ @	$\bar{I}_o / \hat{I}_o = 1\,\text{pu}$ @ $\delta = ½;\ \frac{v_o}{E_i} = 2$	$\bar{I}_i / \hat{I}_i = 1\,\text{pu}$ @ $\delta = 1;\ \frac{v_o}{E_i} \to \infty$	$\bar{I}_o / \hat{I}_o = 1\,\text{pu}$ @ $\delta = ⅓;\ \frac{v_o}{E_i} = 1½$	$\bar{I}_i / \hat{I}_i = 1\,\text{pu}$ @ $\delta = ½;\ \frac{v_o}{E_i} = 2$
change of variable	$\frac{\bar{I}_o}{\hat{I}_o} = 4\delta^2 \times \frac{1}{\frac{v_o}{E_i} - 1}$	$\frac{\bar{I}_i}{\hat{I}_i} = \delta^2 \times \frac{\frac{v_o}{E_i}}{\left(\frac{v_o}{E_i} - 1\right)}$	$\frac{\bar{I}_o}{\hat{I}_o} = {}^{27}\!/_4\,\delta^2 \times \frac{1}{\left(\frac{v_o}{E_i} - 1\right)\frac{v_o}{E_i}}$	$\frac{\bar{I}_i}{\hat{I}_i} = 4\delta^2 \times \frac{1}{\frac{v_o}{E_i} - 1}$
change of variable	$\delta = ½\sqrt{\frac{\bar{I}_o}{\hat{I}_o} \times \left(\frac{v_o}{E_i} - 1\right)}$	$\delta = \sqrt{\frac{\bar{I}_i}{\hat{I}_i} \times \frac{\frac{v_o}{E_i} - 1}{\frac{v_o}{E_i}}}$	$\delta = \sqrt{{}^{4}\!/_{27} \times \frac{\bar{I}_o}{\hat{I}_o} \times \left(\frac{v_o}{E_i} - 1\right)\frac{v_o}{E_i}}$	$\delta = ½\sqrt{\frac{\bar{I}_i}{\hat{I}_i} \times \left(\frac{v_o}{E_i} - 1\right)}$
conduction boundary	$\frac{\bar{I}_o}{\hat{I}_o} = 4 \times \frac{\left(\frac{v_o}{E_i} - 1\right)}{\left(\frac{v_o}{E_i}\right)^2}$ $= 4\delta(1-\delta)$	$\frac{\bar{I}_i}{\hat{I}_i} = \frac{\left(\frac{v_o}{E_i} - 1\right)}{\frac{v_o}{E_i}}$ $= \delta$	$\frac{\bar{I}_o}{\hat{I}_o} = {}^{27}\!/_4 \times \frac{\left(\frac{v_o}{E_i} - 1\right)}{\left(\frac{v_o}{E_i}\right)^3}$ $= {}^{27}\!/_4\,\delta(1-\delta)^2$	$\frac{\bar{I}_i}{\hat{I}_i} = 4 \times \frac{\left(\frac{v_o}{E_i} - 1\right)}{\left(\frac{v_o}{E_i}\right)^2}$ $= 4\delta(1-\delta)$
conduction boundary	$\delta = ½ + ½\sqrt{1 - \frac{\bar{I}_o}{\hat{I}_o}}$	$\delta = \frac{\bar{I}_i}{\hat{I}_i}$	${}^{27}\!/_4\,\delta(1-\delta)^2 = \frac{\bar{I}_o}{\hat{I}_o}$	$\delta = ½ + ½\sqrt{1 - \frac{\bar{I}_i}{\hat{I}_i}}$
conduction boundary	$\frac{v_o}{E_i} = \frac{1}{1-\delta}$	$\frac{v_o}{E_i} = \frac{1}{1-\delta}$	$\frac{v_o}{E_i} = \frac{1}{1-\delta}$	$\frac{v_o}{E_i} = \frac{1}{1-\delta}$

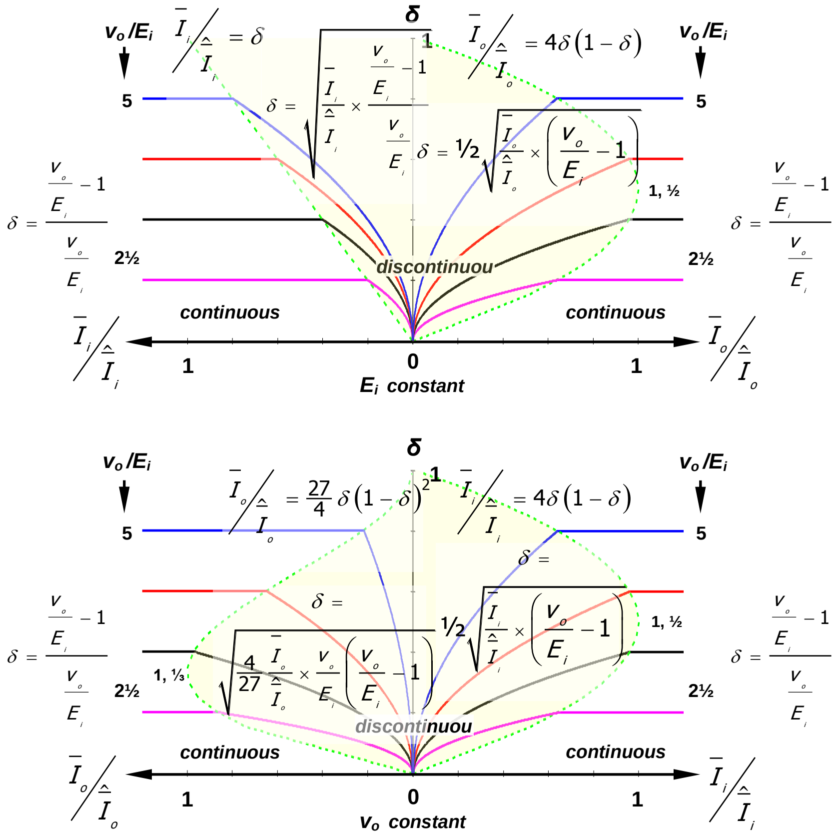

Fig .2. Control of duty cycle δ to maintain a constant output voltage.

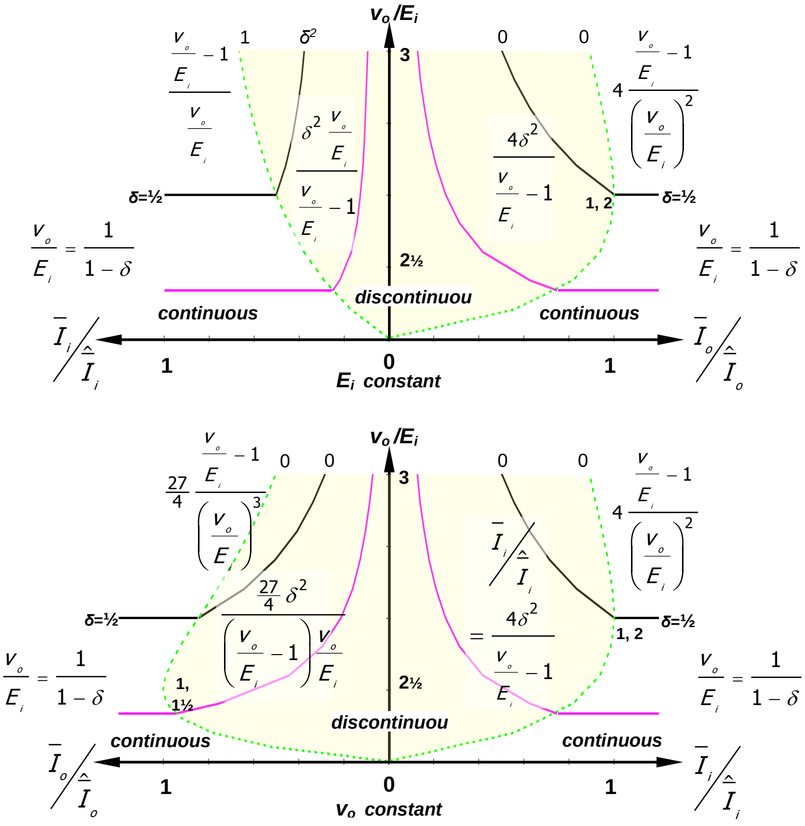

Fig .3. Voltage variation for constant duty cycle δ.

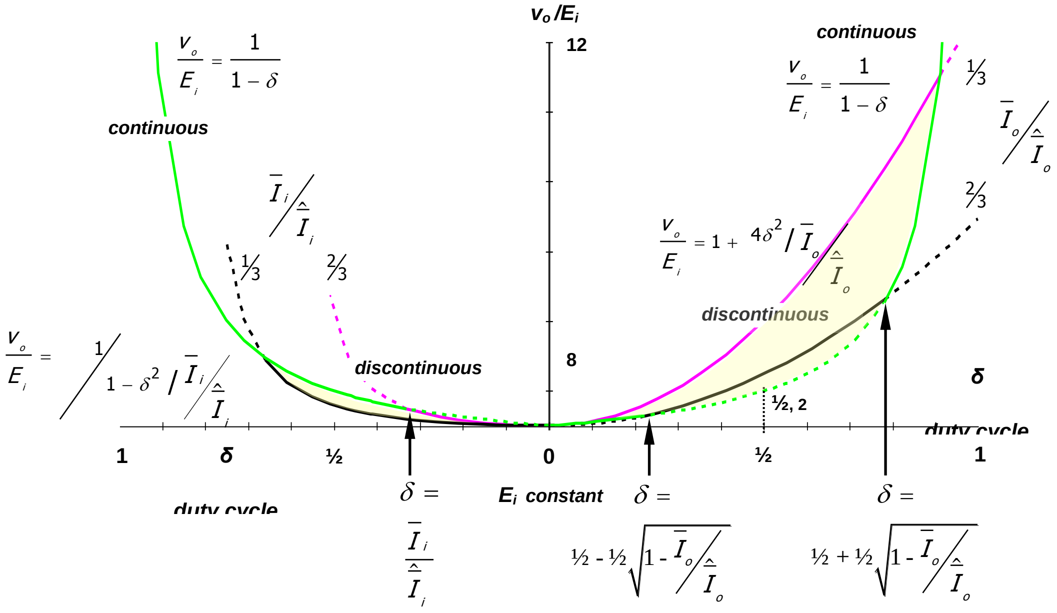

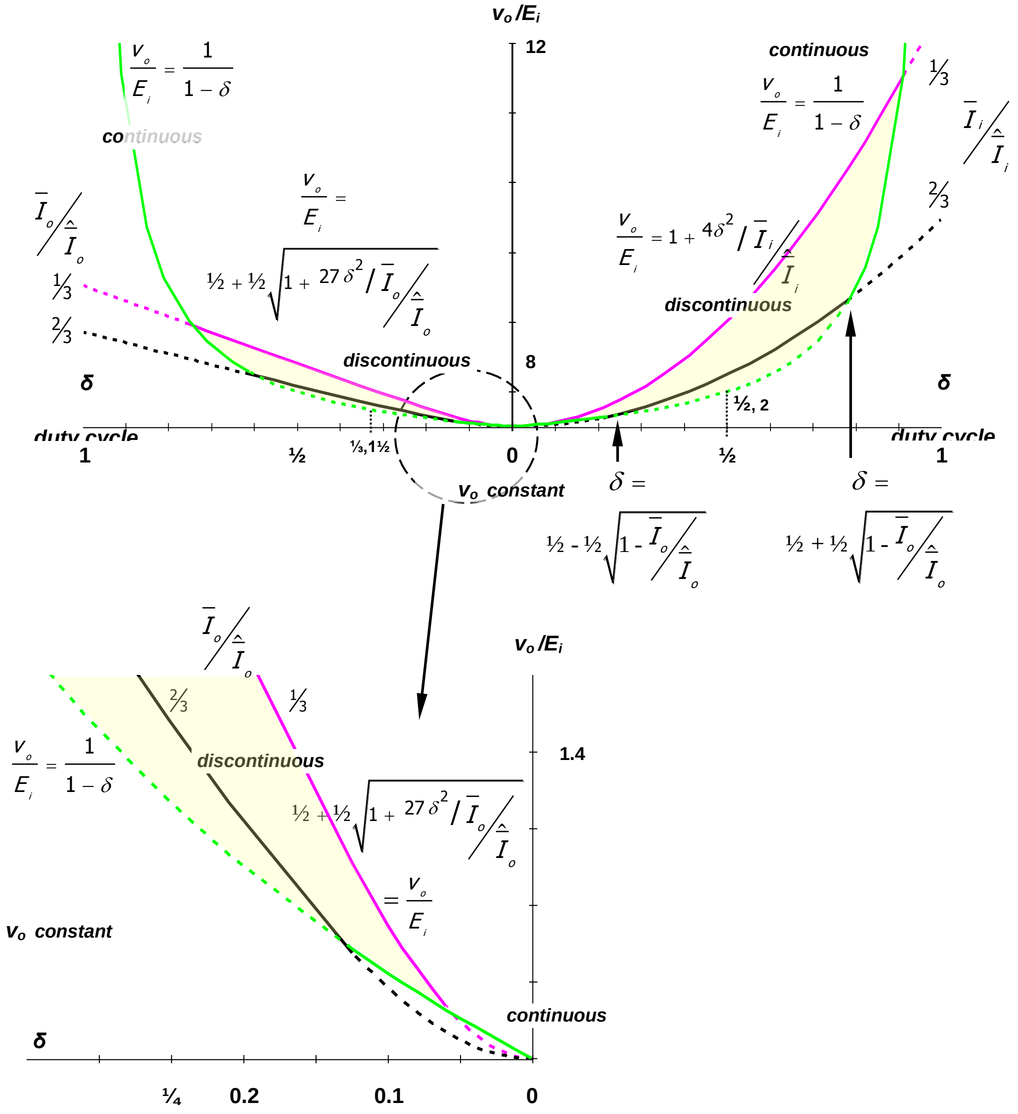

Fig .4. Output voltage variation for constant current.

B. Normalisation in terms of load resistance

In the previous analysis, the transfer function for discontinuous conduction (and its boundary) is normalised with respect to the maximum discontinuous current of the form:

$$\bar{I}_o = \frac{\tau v_o}{L} \tag{24}$$

Multiplying both sides by the load resistance gives

$$\bar{I}_o R = \frac{\tau R}{L} v_o = k \times v_o \tag{25}$$

where

$$k = \frac{\tau R}{L} \qquad \left(= {}^{27}\!/\!_2 / \frac{\bar{I}_o}{\hat{\bar{I}}_o} = {}^{2\pi}\!/\!_Q \right) \qquad \text{(p.u.)} \tag{26}$$

which is the ratio of two time constants – the switch off-period circuit time constant L/R and the reciprocal of the switching frequency, namely, τ. Being relate to circuit *Q*, the symbol *k* in (26) is the ratio of energy delivered divided by total energy stored per cycle – a characteristic not previously observed.

- Discontinuous inductor current [5]:

The peak inductor current $\hat{i}_L$, during discontinuous inductor current operation is determined solely by the duty cycle, according to equation (5). That is

$$\hat{i}_L \frac{R}{E_i} = \frac{R}{E_i} \frac{E_i \delta \tau}{L} = k\delta$$

The average inductor current for discontinuous inductor conduction is shown in Table 2.

Consider the central identity expression in equation (6), which assumes $\check{i}_L = 0$

$$\frac{v_o}{E_i} = 1 + \frac{E_i \tau \delta^2}{2L\bar{I}_o} \tag{27}$$

which is based on the energy equation (7)

$$v_o \bar{I}_o = E_i \bar{I}_o + ½L\Delta i_L^2 / \tau$$

On substitution of *k* into equation (27), after suitable multiplication by *R*, then $v_o = I_o R$, gives (see equation (6))

$$\frac{v_o}{E_i} = 1 + \frac{E_i \tau \delta^2}{2L\bar{I}_o} = 1 + \frac{E_i \tau R \delta^2}{2L\bar{I}_o R} = 1 + \frac{E_i \tau R \delta^2}{2L v_o} = 1 + ½k\delta^2 \frac{E_i}{v_o} \tag{28}$$

Isolating the voltage transfer function, gives for discontinuous conduction

$$\frac{v_o}{E_i} = \frac{\bar{I}_i}{\bar{I}_o} = \bar{I}_o \frac{R}{E_i} = ½\left[1 + \sqrt{1 + 2k\delta^2}\right] \tag{29}$$

where the output current has been normalised by the minimum output current, when $\delta = 0$, the term E_i/R. The voltage transfer function for discontinuous inductor current in (29) along with the normal voltage transfer function in equation (2), are plotted in figure 5. The condition $k = 13½$, the verge of discontinuous inductor current at $\delta = ⅓$ is shown. Also shown is the boundary conditions for increased load resistance, $k = 22$, $\delta = 0.62$. The magnified view inset shows that continuous inductor current operation re-emerges at a low duty cycle of less than $\delta = 0.12$. This re-emergence of continuous inductor current at low duty cycles occurs for $k > 13½$, and can be characterised more rigorously by investigating the minimum inductor current characteristics.

- Continuous inductor current:

The key circuit parameter is the minimum inductor current, $\check{i}_L$, which for continuous inductor current, is given by

$$\check{i}_L = \bar{I}_i - \frac{E_i}{2L}\delta\tau \qquad \text{(A)} \tag{30}$$

Normalisation with respect to the minimum load current, E_i/R, gives

$$\begin{aligned}\check{i}_L \frac{R}{E_i} &= \bar{I}_i \frac{R}{E_i} - \frac{R}{2L}\delta\tau \\ &= \frac{1}{1-\delta}\times\frac{v_o}{E_i} - \tfrac{1}{2}k\delta\end{aligned} \qquad (31)$$

The voltage transfer function, equations (2) and (29), various inductor currents (average $\bar{I}_L$, peak $\hat{i}_L$, minimum $\check{i}_L$, equation (31)), etc. are summarised in Table 2. Critical circuit conditions, namely the boundary between continuous and discontinuous inductor current, occur when the minimum inductor current equals zero, that is, in equation (31) $\check{i}_L$ equals zero:

$$0 = \frac{1}{1-\delta}\times\frac{v_o}{E_i} - \tfrac{1}{2}k\delta \qquad (32)$$

whence, on substituting the voltage transfer function, equation (2), which is valid on the boundary, yields

$$\delta\left(1-\delta\right)^2 = {}^{2}\!/\!_{k} \quad \left(= {}^{4}\!/\!_{27}\bar{I}_o \,/\, \bar{I}_o\right) \qquad (33)$$

as the discontinuous current conduction boundary condition. Note the similarity to equation (19). Such analysis to derive this equation appears in texts [5], but analysis progresses little further.

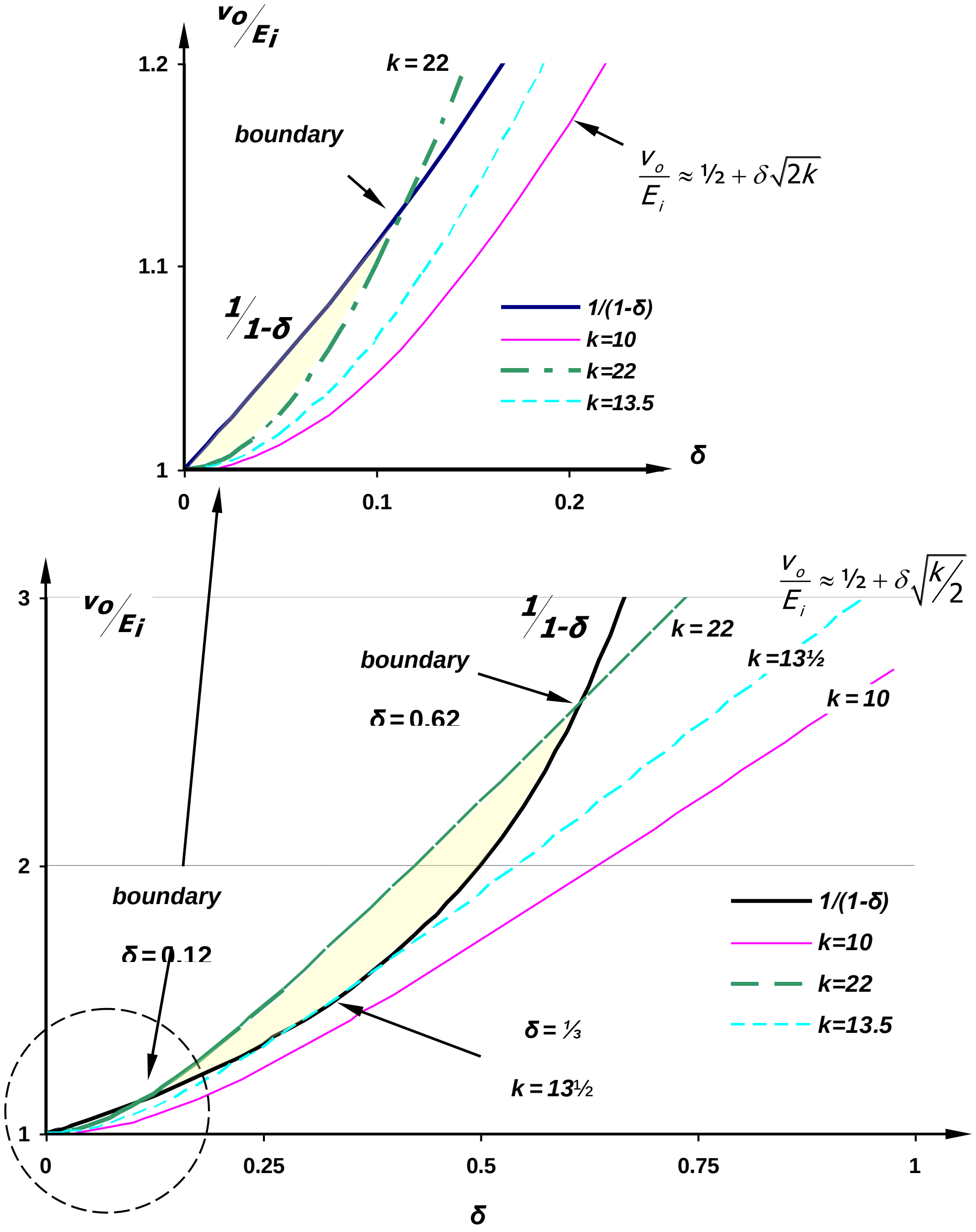

Fig .5. Voltage transfer function variation with duty cycle, showing discontinuous current boundaries.

Table 2. Step-up converter transfer functions, load resistance normalised.

$k = \frac{R\tau}{L}; \quad 0 \le \delta = \frac{t_T}{\tau} \le 1$	Converter	
	Flyback-boost or step-up	
	discontinuous	continuous
$\delta_{critical}(k) =$ $k \ge \frac{2}{\delta(1-\delta)} \times \frac{V_o}{E_i}$	$k > 27/2$ $\delta(1-\delta)^2 \le 2/k$	$k \le 27/2$ $\forall\delta$
$\frac{V_o}{E_i}(k,\delta) = \frac{\bar{I}_i}{\bar{I}_o} = \bar{I}_o \times \frac{R}{E_i}$	$\tfrac{1}{2}\left[1+\sqrt{1+2k\delta^2}\right]$	$\frac{1}{1-\delta}$
$\delta_D = \frac{t_D}{\tau}$	$\delta \times \frac{1}{\frac{V_o}{E_i}-1} \ge 2\delta$ $\check{\delta}_D = 2\delta$	$1-\delta$
$\delta_x = \frac{t_x}{\tau}$ $= 1-(\delta+\delta_D)$	$1 - \delta \times \frac{\frac{V_o}{E_i}}{\frac{V_o}{E_i}-1}$ $\delta_x = \sqrt{3/2k} = 1-3\delta$	0
$\hat{i}_L \times \frac{R}{E_i}, \quad \check{i}_L \times \frac{R}{E_i}$	$k\delta, 0$	$\frac{1}{1-\delta} \times \frac{V_o}{E_i} \pm \tfrac{1}{2}k\delta$
$\bar{I}_L \times \frac{R}{E_i}$ $\bar{I}_L = \tfrac{1}{2}\left(\hat{i}_L + \check{i}_L\right)(\delta+\delta_D)$	$\tfrac{1}{2}k\delta^2 \times \frac{\frac{V_o}{E_i}}{\frac{V_o}{E_i}-1}$ $\left.\bar{I}_L \times \frac{R}{E_i}\right\|_{\min} = 9/4$	$\frac{1}{1-\delta} \times \frac{V_o}{E_i}$ $\left.\bar{I}_L \times \frac{R}{E_i}\right\|_{\min} = 1$
$I_c = 0$ $i_L(\delta \le t \le \delta+\delta_D) \le I_o$	$\left.t/\tau\right\|_{t \le t_T} = \delta$	$\left.t/\tau\right\|_{t \le t_T} = \delta$
	$\forall\delta$ $t/\tau = \delta_D\left(1 - \frac{V_o/E_i}{k\delta}\right)$ $t_T < t \le \tau$	if $k \le 2$ then $I_c \ne 0$, otherwise $\delta \le 1-\sqrt{\frac{2}{k}} \qquad k \ge \frac{2}{1-\delta} \times \frac{V_o}{E_i}$ $\left.t/\tau\right\|_{t_T < t \le \tau} = \tfrac{1}{2}(1-\delta) + \frac{V_o}{E_i} / k$ $t_T < t \le \tau$
$\frac{\Delta v_C}{V_o}$	$\frac{\delta\tau}{RC} \frac{\tfrac{1}{2}k\delta\left(1-\frac{V_o}{E_i}\frac{1}{k\delta}\right)^2}{\left(\frac{V_o}{E_i}-1\right)\frac{V_o}{E_i}}$	$\frac{\delta\tau}{RC}$
		$\frac{1}{1-\delta} \times \frac{V_o}{E_i} - \tfrac{1}{2}k\delta \ge I_o \frac{R}{E_i}$

III. MATHEMATICALLY ANALYSIS OF THE BOUNDARY CUBIC POLYNOMIAL

Consider equation (33) rearranged into a more general cubic polynomial form

$$y = \delta(1-\delta)^2 - c \quad \text{where} \quad c = 2/k \tag{34}$$

As a cubic polynomial, at least one real root exists for δ. The effect of the constant term c is to produce a Y-axis shift of the basic cubic function, thus in this case, determining if one or more real roots exist.

The duty cycle range of interest is $0 \le \delta \le 1$ and $c \ge 0$ (representing positive output current). Although primarily interested in the roots of this cubic, those roots are uniquely associated with the properties of the local maxima and minima. Equating the first differential to zero (and testing for a maxima or minima) yields $\hat{\delta} = \frac{1}{3}$ and $\check{\delta} = 1$, both independent of c. The local minima $\check{\delta} = 1$ always occurs at a value of $-c$, the Y-axis intercept value (when $\delta = 0$). The inflexion point (second differential equated to zero) gives $\delta_{\text{inflex}} = \frac{2}{3}$, whence a local maxima and minima always exist.

The local maxima and minima represent the δ values at which roots emerge and disappear respectively, as the value of c (the Y-axis intercept) shifts the cubic plot up the Y-axis (decreasing current), as shown in figure 6.

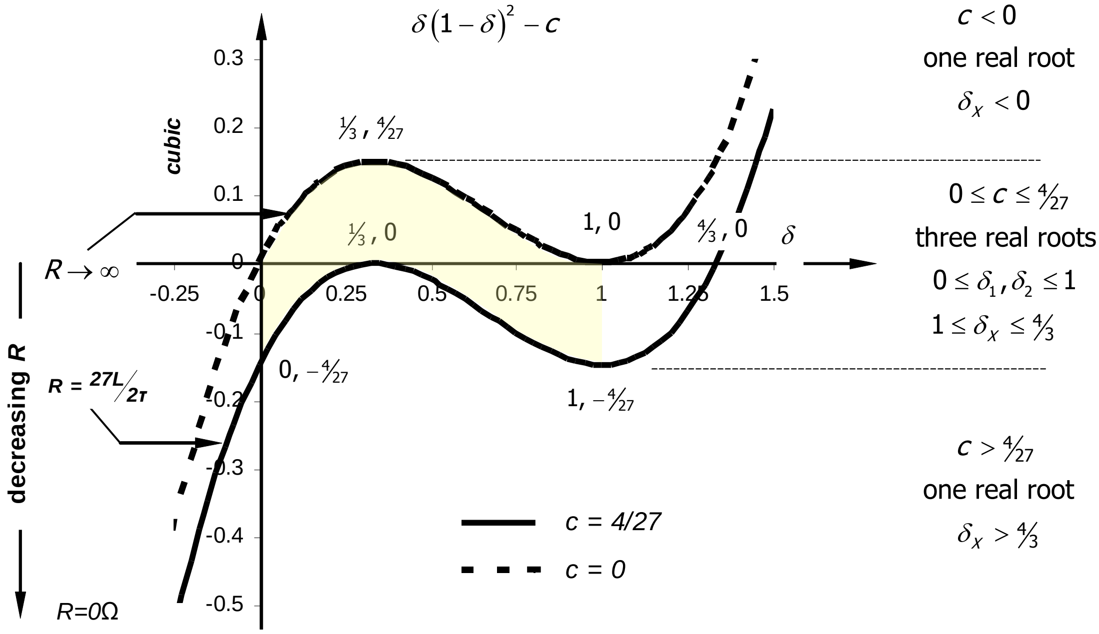

Fig .6. Boundary conditions for three real roots to the cubic equation.

Solvable, unique boundary solutions exist for δ when all three real roots exist such that two are coincident (real and equal). These cases are plotted in figure 6. Equation (34) is equated to the following general cubic with two coincident roots, which releases a solution degree of freedom.

$$\delta(1-\delta)^2 - c = 0 = (\delta - \delta_X)(\delta - \delta_{critical})^2 \qquad (35)$$

By expanding both sides and equating coefficients, because of the released degree of freedom, a unique, viable, quadratic solution results, yielding:

$\delta_{critical} = \frac{1}{3}$ or 1 and $\delta_X = \frac{4}{3}$ and for $\delta = \frac{1}{3}$, $c = 4/27$ ($k = 13\frac{1}{2}$). The root $\delta_X = \frac{4}{3}$ supports the fact that when only one real, positive root exists, that root occurs for $\delta_X \ge \frac{4}{3}$. Similar analysis on the local minimum yields that if only one real negative root exists that single root must be less than zero, hence a single root solution is in the range $0 \ge \delta_X \ge \frac{4}{3}$; always outwith the range of interest, $0 \le \delta \le 1$. The local minima also yields coincident roots, at $\delta = 1$, when $c = 0$ ($k \rightarrow \infty$, an output open circuit). Exact solutions for the roots of the cubic polynomial, in terms of its coefficients, can be found in the Appendix.

IV. INTERPRETATION OF THE BOOST CONVERTER BOUNDARY CUBIC POLYNOMIAL

- Interpretation of the cubic analysis results, is:

if $k < 13\frac{1}{2}$ ($c > 4/27$, with no real roots between $0 < \delta < 1$), discontinuous inductor current does not occur for any duty cycle δ. From equation (26), continuous inductor current results if

$$k = \frac{\tau R}{L} \le {}^{27}\!/_{2} \tag{36}$$

As k increases above $13\frac{1}{2}$ ($0 < c < 4/27$), as the load resistance increases and the load current decreases, a region about $\delta = ⅓$ spreads asymmetrically (towards $\delta = 1$ and towards $\delta = 0$), where δ in that range results in discontinuous inductor current. The implication of the critical range spreading in both directions about $\delta = ⅓$, is significant. For a given fixed load resistance, with $k > 13\frac{1}{2}$, as the duty cycle decreases from a maximum, discontinuous inductor current results before $\delta = ⅓$, ***but***, as the duty cycle is reduced below $\delta = ⅓$, further towards zero, continuous inductor current conduction always re-emerges [5].

- A *corollary*, at first sight contradictory, is that:

if the duty cycle δ is maintained constant as the load current is decreased (k increased), once discontinuous inductor current occurs, continuous inductor current operation does not re-emerge (if the duty cycle is maintained constant), as confirmed by any of the four plots in figure 3.

In figure 3 once a constant duty cycle contour enters the shaded discontinuous current region, the output voltage increases and the constant duty cycle contour remains in the discontinuous current region as the current decreases to zero. Only if the duty cycle is decreased (decreasing the energy being transferred to the load) can operation re-enter the continuous inductor current region. Theoretically continuous inductor current occurs at $\delta = 0$.

The normalised design monogram in figure 7, illustrating the equations in Table 2 with $k = 22$, for which discontinuous conduction occurs according to equation (31), illustrates the properties of the cubic boundary equation (33). For $k = 22$, the boundary values for discontinuous conduction are $0.12 \le \delta_{crit} \le 0.62$. In figure 7, the inductor current waveform is continuous for $\delta = 0.65$, then discontinuous when the duty cycle is reduced to $\delta = 0.3$. If the duty cycle is further reduced, to $k = 0.05$, continuous conduction is predicted, as substantiated by the PSpice plots in figure 8c.

Figure 8, parts a to c, show PSpice plots for three load conditions ($k = 10$, $13\frac{1}{2}$, and 22). The first, figure 8a, is when $k = 10$, and continuous inductor current occurs for all δ, as predicted. The plot in figure 8b, shows operation on the verge of discontinuous conduction, when for $\delta = ⅓$ the minimum inductor current just reaches zero, as predict for $k = 13\frac{1}{2}$. Figure 8c shows the case for $k = 22$, when discontinuous inductor current results, but re-emerges at a lower duty cycle.

The reason why continuous current recommences at low duty cycles ($\delta < ⅓$) is related to the amount and how energy is transferred to the load. During normal operation, when the switch is off, two sources transfer energy to the load, as shown by equation (3).

$$E_i \,\overline{I}_o + \tfrac{1}{2} L\left(\hat{i}_L^{2} - \check{i}_L^{2}\right)/\tau = v_o \,\overline{I}_o$$

The source E_i energy is proportional to load current, while the energy from the inductor is quadratic current dependent, and the load current is proportional to voltage. The output voltage decreases according to ${}^{1}\!/_{1-\delta}$ when inductor conduction is continuous, but is approximately proportional to duty cycle (from equation (29) and figure 5), when discontinuous. The energy from the supply when the switch is off is that necessary to maintain the output at its minimum value E_i, equation (4), while the inductor energy produces the boost voltage above E_i, δv_o.

At high duty cycles the necessary quadratic inductor energy reduces at the same rate as the output energy fall rate which is dependant on the duty cycle. At the boundary of discontinuous inductor current, the troughs of the inductor current are unable to reverse (therein transferring energy back to the dc supply), which results in excess energy being transferred to and retained by the load circuit. As the duty cycle is decreased below this level, the load energy rate decreases approximately linearly with duty cycle, at a faster rate than the inductor energy rate reduction. As the duty cycle decreases further, the load requirement is such to necessitate inductor energy associated with continuous inductor current. The inductor energy again balances the boost voltage according to the transfer function $1/1-\delta$.

Progressive a larger percentage of energy must be provided by the supply energy component, which can only support an output voltage E_i. As δ tends to zero the vast majority of the load energy is provided directly by the dc supply; with a continuous load (hence inductor) current, $\bar{I}_o = E_i/R$ from the supply when $\delta = 0$ and the inductor ripple current is zero.

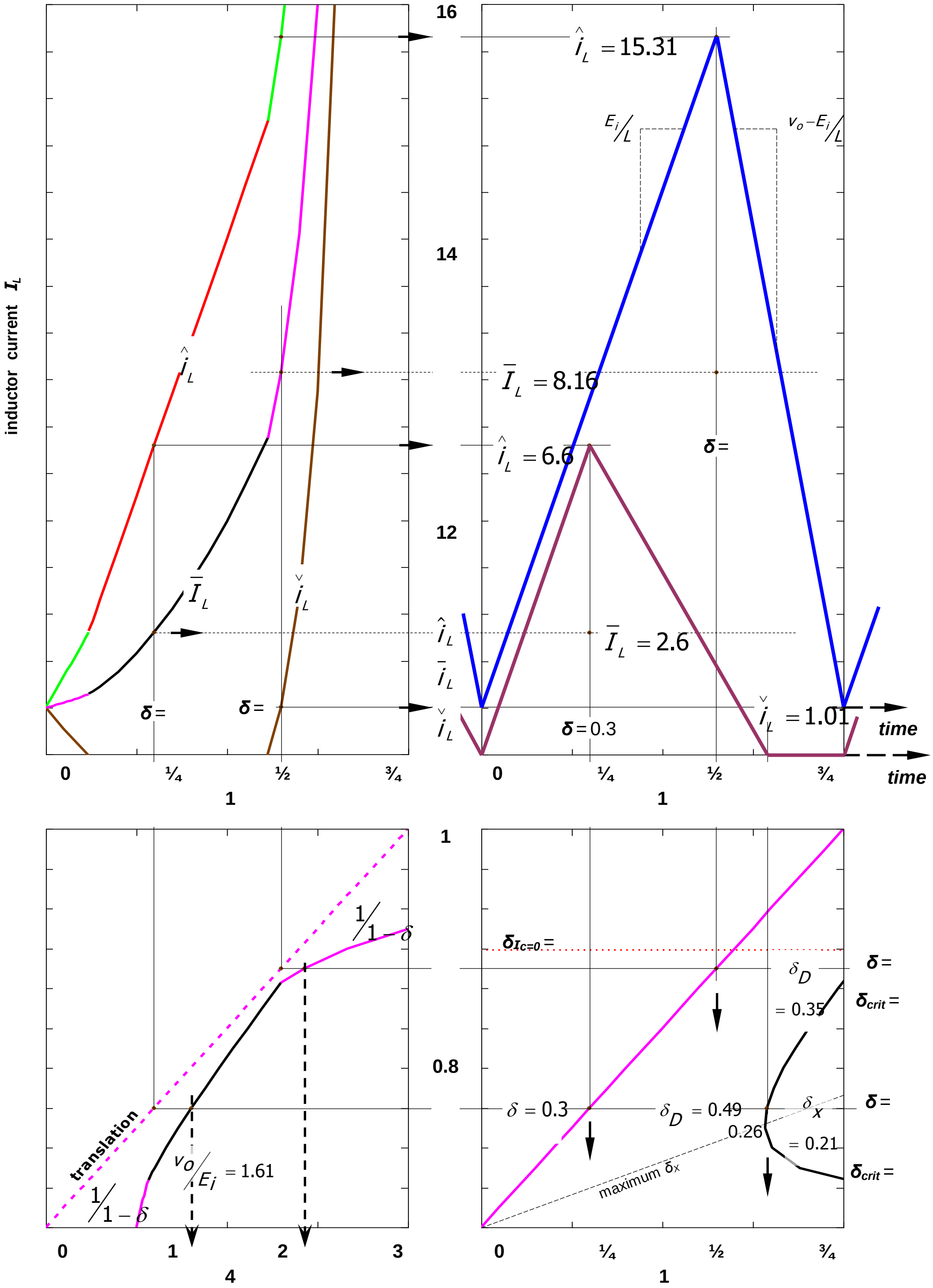

Fig .7. Step-up converter performance monogram for k = 22, giving discontinuous inductor current for 0.12 ≤ δcrit ≤ 0.62. Inductor time domain current waveforms for δcont = 0.65 (continuous inductor current) and δdis = 0.3 (discontinuous inductor current). Capacitor discharge in switch-off period δ ≤ 0.7.

V. GENERAL ANALYSIS OF THE BOOST CONVERTER

Figure 9 shows the minimum inductor current at the boundary of discontinuous inductor current, as given by equation (31), plotted in three different domain combinations. Specifically the plots are combinations of *k*, *δ,* and the normalised minimum inductor current:

$$\check{i}_L \frac{R}{E_i} = \frac{1}{(1-\delta)^2} - \tfrac{1}{2}k\delta \qquad (37)$$

Together the four shown plots reveal the underlying mechanisms of the boost converter. Reversible converter operation has been assumed in equation (37), that is the voltage transfer function, equation (2), is always valid. This recognises that if the boost converter is reversible (extra switch and diode) then the inductor current can reverse and the transfer function given by equation (2) remains valid for all *δ*, provided $\bar{I}_o \ge 0$ with a passive *R* load.

The first plot, 8a, of minimum inductor current versus load, *k*, shows the minimum inductor current reaching zero when the load resistance reaches $k = 13\tfrac{1}{2}$ for $\delta = \tfrac{1}{3}$, thereby confirming the solution to (35).

The minimum current locus is derived from differentiation of equation (37)

$$\frac{d}{d\delta}\check{i}_L \frac{R}{E_i} = \frac{2}{(1-\delta)^3} - \tfrac{1}{2}k = 0$$

whence $\delta = 1 - \sqrt[3]{\frac{4}{k}}$ such that $k \ge 4$

Substitution of this duty cycle condition back into equation (37) gives

$$\left.\check{i}_L \frac{R}{E_i}\right|_{\min} = \frac{1}{\left(\sqrt[3]{\frac{4}{k}}\right)^2} - \tfrac{1}{2}k\left(1 - \sqrt[3]{\frac{4}{k}}\right) \qquad (38)$$

The straight line (equation (31)) tangents (of slope ½*δ* from differentiation of equation (37) with respect to *k*) represent the minimum inductor current variation for a constant duty cycle *δ* as the load *k*, is changed. This plot is not readily interpreted when $k < 4$ (high load current levels), for it tends to predict tangents such that $\delta < 0$. Obviously $\delta = 0$ is a restriction, hence the minimum locus plot in figure 9a is shown dashed for $k < 4$.

The plot in figure 9b shows minimum inductor current plotted against duty cycle *δ* for different load conditions, *k*. The locus of the minimum possible inductor current for a given load is derived by differentiating equation (37) with respect to *δ* and equating to zero, giving

$$k = \frac{4}{(1-\delta)^3}$$

which on substitution back into equation (37) yields the locus:

$$\left.\check{i}_L \frac{R}{E_i}\right|_{\min} = \frac{1-3\delta}{(1-\delta)^3} \qquad (39)$$

The plot (and equation (39) when equal to zero) confirms the critical inductance current condition occurring at $k = 13\tfrac{1}{2}$ for $\delta = \tfrac{1}{3}$. Figure 9b sheds some light on the converter mechanisms when $k < 4$. As the load current increases, (that is, load resistance decreases - *k* decreases) the locus of minimum inductor current increases, the minimum value of which increases as duty cycle decreases. At $k = 4$, the minimum possible inductor current of 1 pu, $\check{i}_L = E_i / R$, occurs at $\delta = 0$, any further decrease in load resistance results in the minimum normalised inductor current of 1pu continuing to occur at $\delta = 0$. The theoretical locus for *k*=0, that is an output short circuit is shown, with *k* < 0 being shaded as an unobtainable operating region.

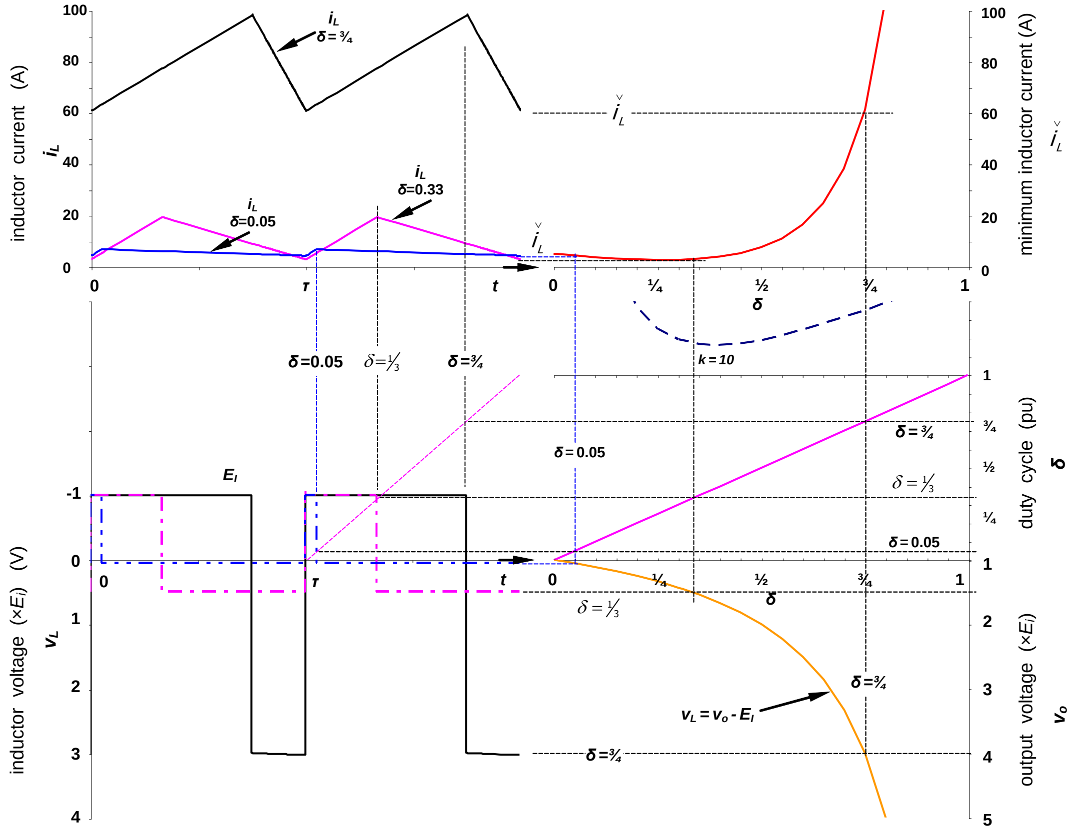

Fig .8a. Step-up converter performance, k=10=R. [Ei = 50V, R = 10Ω, L = 100μH, τ = 100μs, δ = 0.05, ⅓, ¾]

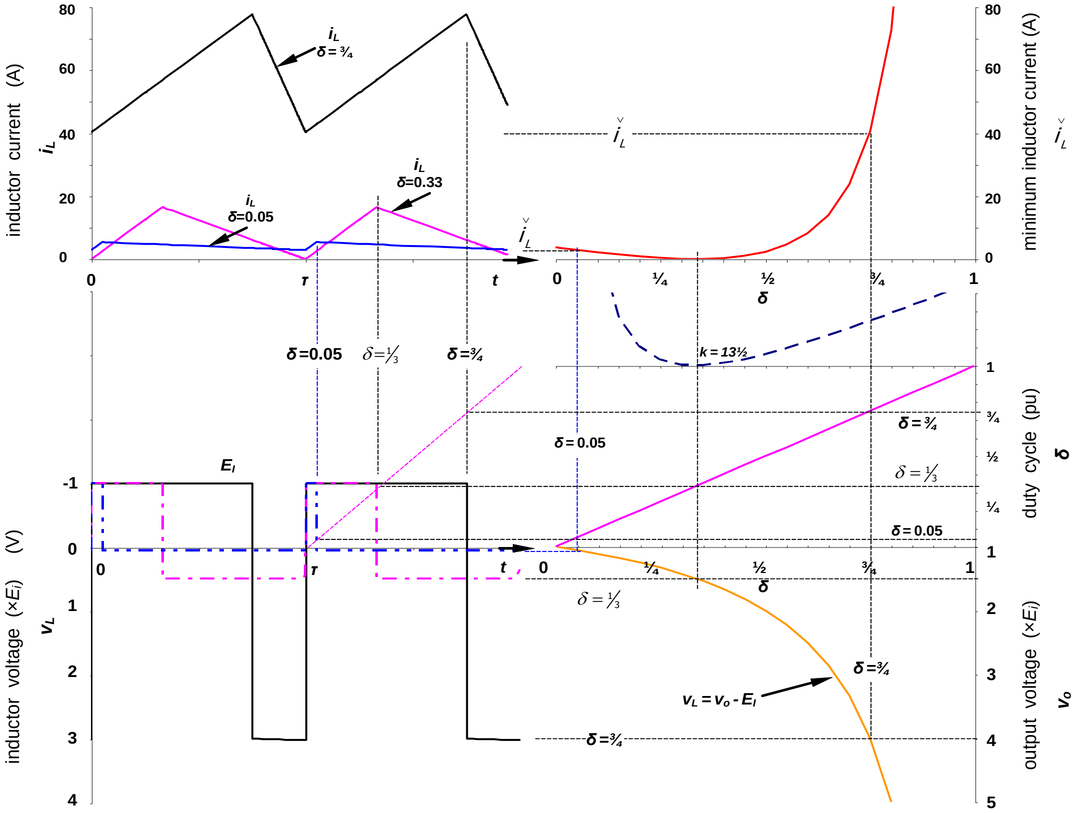

Fig .8b. Step-up converter performance, k=13½=R.[Ei = 50V, R = 10Ω, L = 100μH, τ = 100μs, δ = 0.05, ⅓, ¾]

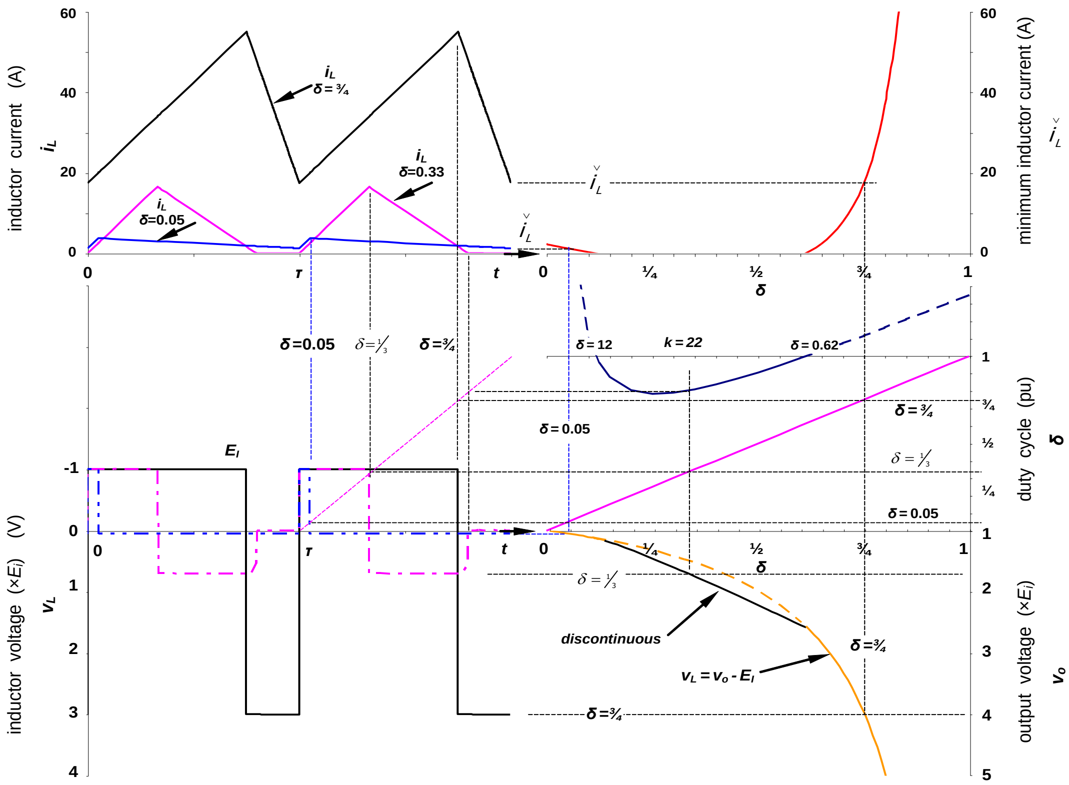

Fig .8c. Step-up converter performance, k=22=R.[Ei = 50V, R = 10Ω, L = 100μH, τ = 100μs, δ = 0.05, ⅓, ¾]

Further insight is gained into operation below $k = 4$, by plot 8c which shows load resistance k plotted against duty cycle δ. The locus of minimum load resistance k for a given duty cycle is given by differentiating (37) with respect to duty cycle, when the equation is expressed in terms of k, namely

$$k=\frac{2}{\delta}\left(\frac{1}{(1-\delta)^2}-\check{i}_L\frac{R}{E_i}\right)$$

which on differentiation and equating to zero yields

$$\check{i}_L\frac{R}{E_i}=\frac{1-3\delta}{(1-\delta)^3}$$

and on back substitution gives

$$k\big|_{\min}=\check{k}=\frac{4}{(1-\delta)^3} \qquad (40)$$

The region of discontinuous inductor current for $k > 13½$ is shown shaded, and is indicated as reversible.

Notice that quadratic type minimum inductor current contours are not obtained when $k < 4$. The best way to interpret the region for $k < 4$ is to examine the extreme limit, when $k = 0$. In the limit, as the load resistance tends to zero, $k = 0$, the minimum inductor current is restricted by the duty cycle. Certain operating current and duty cycle conditions are unobtainable, as shown in plot 8d. As the minimum inductor current increases (less ripple current) the minimum necessary duty cycle increases in order to maintain the output voltage. Since the ripple current maximum peak to peak is fixed (but proportional to duty cycle), this means a limitation on the minimum ripple current at high current levels and low duty cycles. The boundary for forbidden operation in figure 9d (and also shaded in figure 9b) is given by $k = 0$ in equation (37), that is

$$\check{i}_L\frac{R}{E_i}\bigg|_{k=0}=\frac{1}{(1-\delta)^2}=\bar{I}_L\frac{R}{E_i} \qquad (41)$$

The average normalised inductor current is given when $k = 0$ in equation (37) or equation (41).

The limitation area is between $0 < k < 4$, as shown in figure 9d, where the upper bounds is

$$\left.\check{i}_L \frac{R}{E_i}\right|_{k=4} = \frac{1}{(1-\delta)^2} - 2\delta \qquad (42)$$

Rearranging equation (41) gives the minimum duty cycle for k < 4, for which the minimum normalised inductor current is not restricted, as shown in figure 9d.

$$\left.\check{\delta}\right|_{k=0} = 1 - \frac{1}{\sqrt{\check{i}_L \dfrac{R}{E_i}}} \quad \text{for } k < 4 \qquad (43)$$

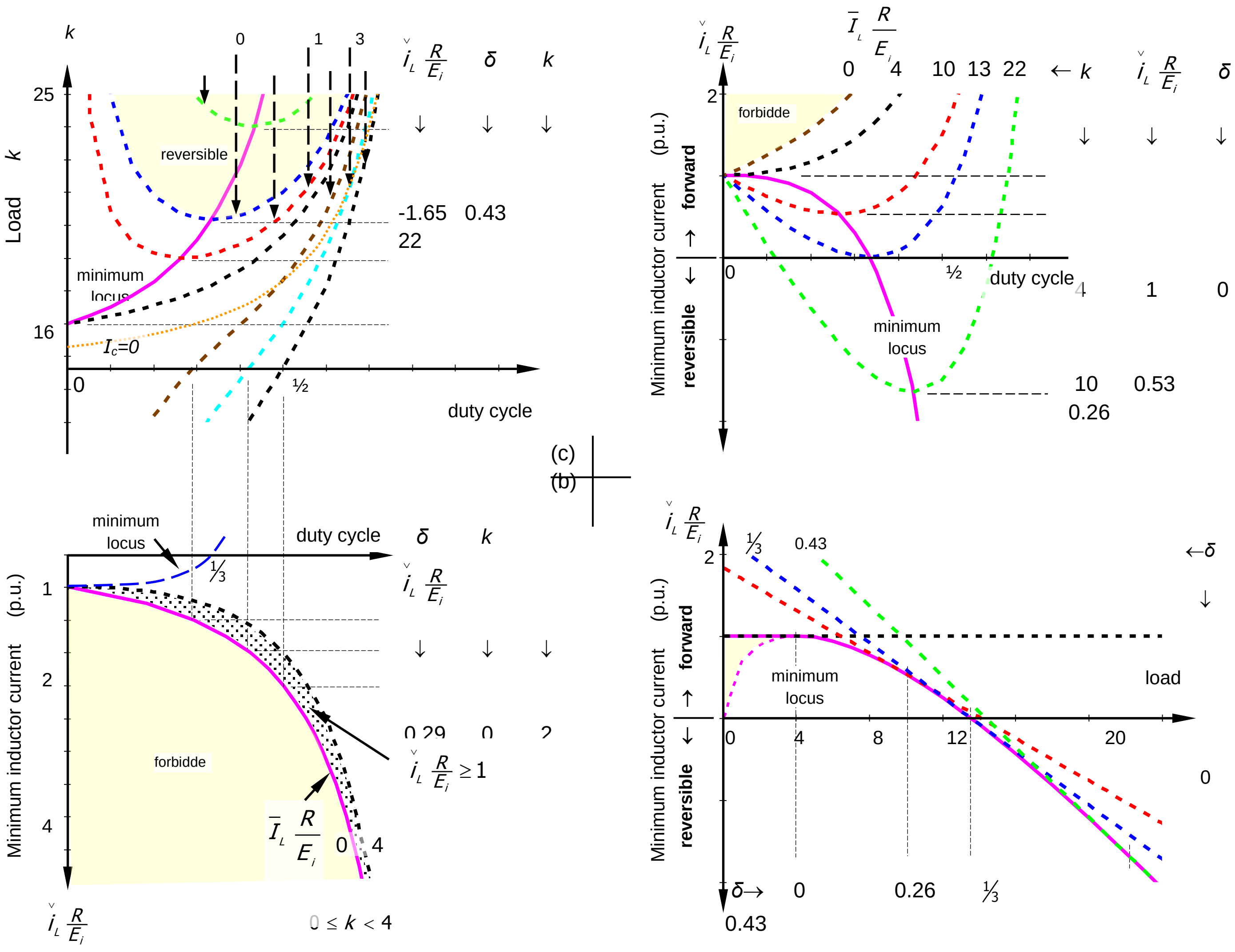

Fig .9. Step-up converter characteristic load curves.

- Maximum period δ_X for zero inductor current

Figure 10 shows the boost converter characteristics for discontinuous inductor current when operating at the maximum length of time with a discontinuous current condition, δ_X. From Table 2, the period of zero inductor current, is given by

$$\delta_X = 1 - \delta \times \frac{\dfrac{V_o}{E_i}}{\dfrac{V_o}{E_i} - 1}$$

$$\text{and} \quad \frac{V_o}{E_i} = \tfrac{1}{2}\left[1 + \sqrt{1 + 2k\delta^2}\right]$$

The maximum non-conduction period, (after eliminating the voltage transfer function, then differentiating and equating to zero) is when

$$k\delta^2 = \frac{3}{2} \text{ for } k \ge {}^{27}\!/_{2} \tag{44}$$

which yields for $\delta = \sqrt{{}^{3}\!/_{2k}}$

$$\delta_X = 1 - 3\delta = 1 - \sqrt{{}^{27}\!/_{2k}} \tag{45}$$

$$\check{\delta}_D = 2\delta = \sqrt{{}^{6}\!/_{k}} \tag{46}$$

when, during discontinuous inductor current, a constant output voltage results

$$\frac{v_o}{E_i} = 1\tfrac{1}{2} \tag{47}$$

These equations reconfirmed the verge of discontinuous inductor current condition, when k=13½, $\delta = ⅓$, $\delta_x = 0$, and $v_o / E_i = 1½$.

Operation at the longest inductor discontinuous current duration point results not only in a constant output voltage, equation (47) but also in a constant average normalised inductor current given by

$$\bar{I}_L \times \frac{R}{E_i} = \tfrac{1}{2}k\delta^2 \times \frac{\frac{v_o}{E_i}}{\frac{v_o}{E_i} - 1} = \tfrac{1}{2} \times {}^{3}\!/_{2} \times \frac{{}^{3}\!/_{2}}{{}^{3}\!/_{2} - 1} = {}^{9}\!/_{4} \quad \text{pu}$$

while the minimum inductor current is zero for all $k >$ 13½, the peak inductor current is

$$\hat{i}_L \times \frac{R}{E_i} = k\delta = \frac{3}{2\delta}$$

These inductor currents are shown in figure 10, along with the boundary case k = 13½ for continuous inductor current conduction.

VI. DISCONTINUOUS CAPACITOR CURRENT DURING THE SWITCH OFF PERIOD

Output ripple voltage is dominated by the capacitor ripple voltage, which is related to the output capacitor

- charging current variation
- equivalent series resistance
- equivalent series inductance

Generally for the boost converter, when the switch is on, the output capacitor provides the entire constant load current $\bar{I}_o$. The capacitor ripple voltage due to this constant discharge is given by

$$\Delta v_C = \frac{1}{C}\int_0^{t_T} \bar{I}_o dt = \frac{1}{C}\bar{I}_o t_T$$

That is

$$\frac{\Delta v_C}{v_o} = \frac{\delta\tau}{RC} \qquad (\text{pu}) \tag{48}$$

This equation assumes that the capacitor only discharges when the switch is on. Under lower duty cycle conditions the capacitor is prone to provide load current when the switch is off, when the inductor current falls to a level which is insufficient to provide all the load current requirement. Such a condition occurs with discontinuous inductor current, that is $\check{i}_L = 0$, as shown in figure 11 (which is figure 9c reproduced for clarity). This boundary condition is defined by equation (33), that is

$$k > {}^{2}\!\big/_{\delta(1-\delta)^2} \tag{49}$$

The capacitor ripple voltage increases above that given by equation (48) and is given by

$$\frac{\Delta v_C}{v_o} = \frac{\delta\tau}{RC}\,\frac{\tfrac{1}{2}k\delta\left(1 - \frac{v_o}{E_i}\frac{1}{k\delta}\right)^2}{\left(\frac{v_o}{E_i} - 1\right)\frac{v_o}{E_i}} \tag{50}$$

The voltage transfer function is given by equation (29).

In fact a more restrictive boundary than equation (49) exists, which is characterised by equating the minimum inductor current to the load current such that I_c = 0, that is $0 < \check{i}_L < \bar{I}_o$. From Table 2, for continuous inductor current the boundary is given by

$$\frac{1}{1-\delta} \times \frac{v_o}{E_i} - \tfrac{1}{2}k\delta = \bar{I}_o \frac{R}{E_i}$$

which, as shown in Table 2, produces a region defined by

$$k > \frac{2}{(1-\delta)^2} \tag{51}$$

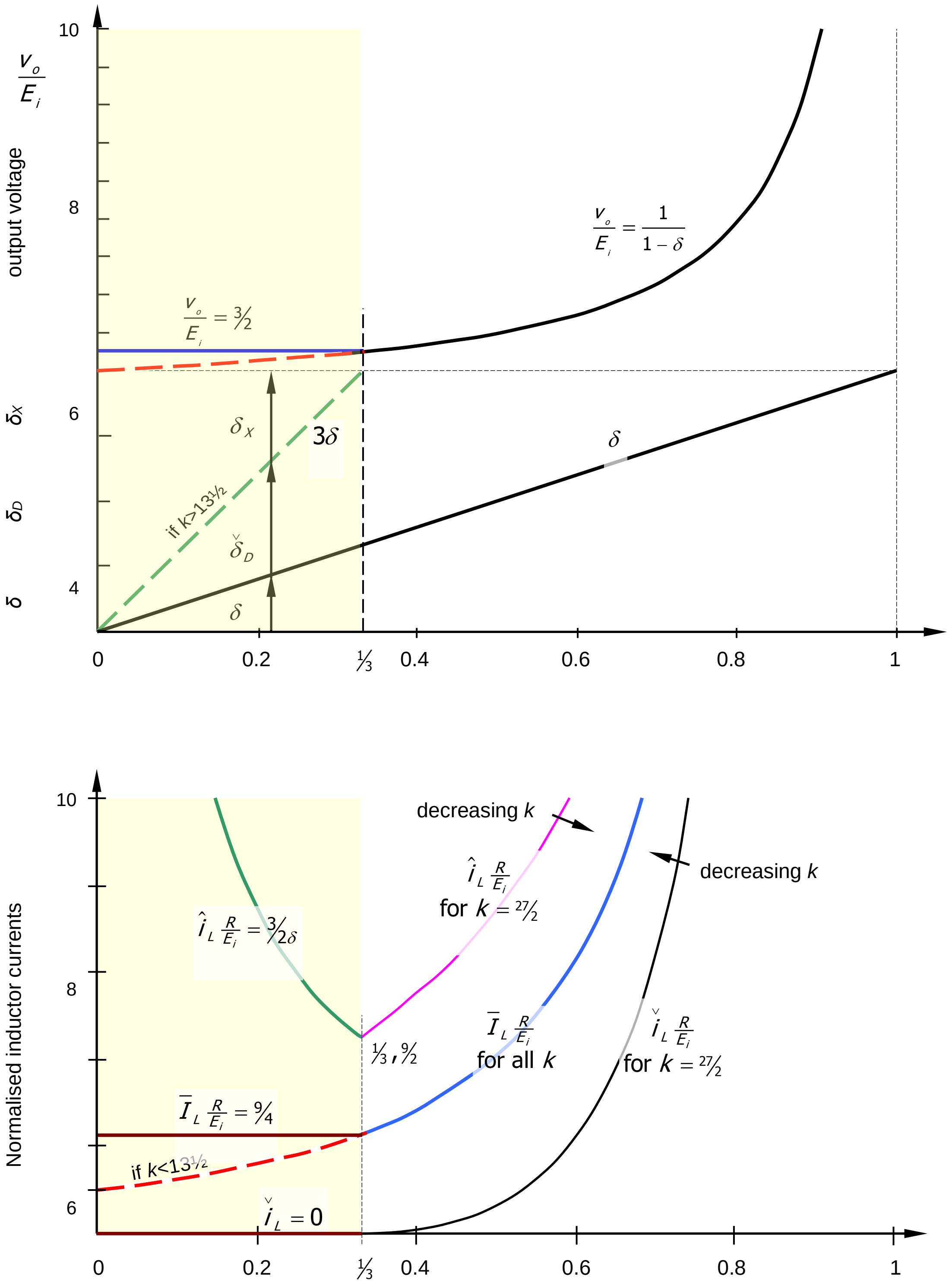

Fig .10. Locus of maximum discontinuous current characteristics.

This boundary is related by the duty cycle δ to the boundary specified by equation (49), both equations being shown in figure 11. Provided discontinuous inductor current does not occur, the voltage transfer function given by equation (2) remains valid. The output ripple voltage magnitude is given by

$$\begin{aligned}\frac{\Delta v_C}{V_o} &= \frac{\delta\tau}{RC}\frac{1}{2k}\left[\frac{1}{1-\delta} + ½k\left(1-\delta\right)\right]^2 \\ &= \frac{\delta\tau}{RC} + \frac{\delta\tau}{RC}\frac{1}{2k}\left[\frac{1}{1-\delta} - ½k\left(1-\delta\right)\right]^2\end{aligned} \qquad (52)$$

The first equality is for when the ripple voltage increases, as the capacitor is recharged immediately after the switch is turned off. The second equality comprises the two components when the capacitor voltage decreases, namely when the switch is on and during the latter part of the switch off period once the inductor current falls below the load current level $\bar{I}_o$.

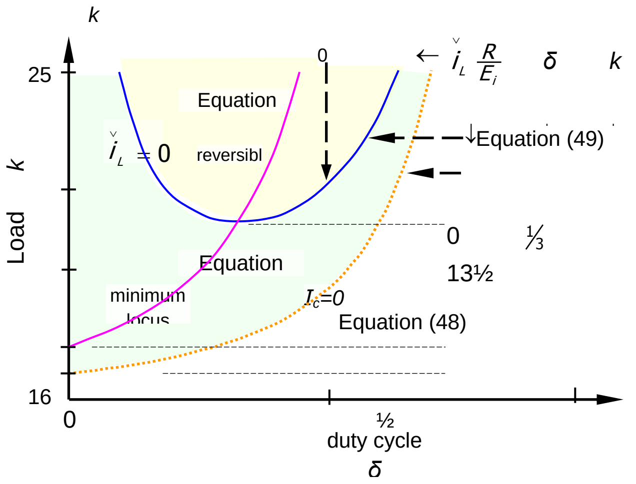

Fig .11. Zero capacitor current characteristics in switch off-state.

VII. CONCLUSIONS

The discontinuous inductor current properties and characteristics of the boost converter have been investigated. Specifically, the re-emergence of continuous inductor current at low duty cycles has been quantified. This property never occurs if the load is varied and the duty cycle is fixed. The minimum inductor current properties at high current have also been investigated. Output capacitor ripple voltage has also been quantified for both discontinuous inductor current and a more likely condition where the inductor current falls below the load current level.

VIII. APPENDIX: EXACT ROOTS OF A CUBIC EQUATION IN TERMS OF ITS COEFFICIENTS

- From Table 1, at the boundary of continuous conduction, equation (21),

$$\frac{\left(\frac{V_o}{E_i}-1\right)}{\left(\frac{V_o}{E_i}\right)^3}=\delta(1-\delta)^2$$

and from Table 2, equation (33)

$$\delta(1-\delta)^2={}^2\!/_k$$

Equating yields

$$\frac{\left(\frac{V_o}{E_i}-1\right)}{\left(\frac{V_o}{E_i}\right)^3}={}^2\!/_k$$

Rearranging gives the normalised cubic equation

$$\left(\frac{V_o}{E_i}\right)^3-\tfrac{1}{2}k\times\frac{V_o}{E_i}+\tfrac{1}{2}k=0$$

Substituting

$$\frac{V_o}{E_i}=X+{}^k\!/_{6X}$$

and solving the resultant quadratic yields

$$X=\sqrt[3]{\tfrac{1}{4}k\left(-1\pm\sqrt{1-{}^{2k}\!/_{27}}\right)}$$

whence for $\frac{V_o}{E_i}\geq 1$

$$\begin{aligned}\frac{V_o}{E_i}&=X+{}^k\!/_{6X}\\&=\sqrt[3]{\tfrac{1}{4}k\left(-1+\sqrt{1-{}^{2k}\!/_{27}}\right)}+{}^{k}\!\Big/_{6\sqrt[3]{\tfrac{1}{4}k\left(-1+\sqrt{1-{}^{2k}\!/_{27}}\right)}}\\&=\sqrt[3]{\tfrac{1}{4}k\left(-1+\sqrt{1-{}^{2k}\!/_{27}}\right)}+\tfrac{1}{6}k\sqrt[3]{\tfrac{1}{4}k\left(1+\sqrt{1-{}^{2k}\!/_{27}}\right)}\end{aligned}$$

From the discriminant, for more than one real root

$k\geq{}^{27}\!/_2$ for which $\frac{V_o}{E_i}={}^3\!/_2$ whence $\delta=\tfrac{1}{3}$ at $k={}^{27}\!/_2$

Note that a *negative* discriminant is the correct condition for more than one real root [6].

- The solution to equation (21), for the duty cycle in terms of the normalised maximum critical inductor current (let $I = \overline{I}_o / \hat{\overline{I}}_o$) is

$$\delta_1 = \tfrac{1}{3}\sqrt[3]{(2I-1)+2\sqrt{I(I-1)}} + \tfrac{1}{3}\sqrt[3]{(2I-1)-2\sqrt{I(I-1)}} + \tfrac{2}{3} \quad (53)$$

The remaining two roots $\delta_{2,3}$ are

$$\delta_{2,3} = -\tfrac{1}{2}\delta_1 + 1 \pm j\frac{1}{2\sqrt{3}}\left(\sqrt[3]{(2I-1)+2\sqrt{I(I-1)}} - \sqrt[3]{(2I-1)-2\sqrt{I(I-1)}}\right) \quad (54)$$

which are all real roots if $0 \le I \le 1$.

- The solution to equation (33), for the duty cycle in terms of the normalised load resistance factor *k*, is found by substituting $I = {}^{27}\!/_{2k}$ into equations (53) and (54), such that more than one real root results if $0 \le {}^{27}\!/_{2k} \le 1$, that is $k \ge {}^{27}\!/_{2}$.

REFERENCES

[1] Kjaer, S.B.; Pedersen, J.K.; Blaabjerg, F. 'A review of single-phase grid-connected inverters for photovoltaic modules', Industry Applications, IEEE Transactions on, 2005, Vol. 41, Issue: 5, pp.: 1292 - 1306, DOI: 0.1109/TIA.2005.853371

[2] Al-Saffar, M.A.; Ismail, E.H.; Sabzali, A.J.. 'Integrated Buck–Boost–Quadratic Buck PFC Rectifier for Universal Input Applications., Power Electronics, IEEE Transactions on, 2009, Vol. 24, Issue: 12, pp 2886 - 2896, DOI: 10.1109/TPEL.2009.2023323

[3] Mohan. N., et al., 'Power Electronics', J Wiley & Sons, 2003, Chapter 7.

[4] Bausiere. R., et al., 'Power Electronics, dc-dc conversion', Springer-Verlag, 1992, Chapter 6.

[5] Erickson. R.W., 'Fundamentals of Power Electronics', Springer, 2001, Chapter 5.

[6] http://www.sosmath.com/algebra/factor/fac11/fac11.html

Journal of Renewable Energy and Sustainable Development (RESD) Volume 1, Issue 2, December 2015 - ISSN 2356-8569

Artificial Neural Network Algorithm for Condition Monitoring of DC-link Capacitors Based on Capacitance Estimation

Hammam Soliman, Huai Wang, IEEE Member, Brwene Gadalla, Frede Blaabjerg, IEEE Fellow
Department of Energy Technology, Aalborg University,
Aalborg 9220, Denmark,
has@et.aau.dk, hwa@et.aau.dk, bag@et.aau.dk, fbl@et.aau.dk

***Abstract* -** In power electronic converters, reliability of DC-link capacitors is one of the critical issues. The estimation of their health status as an application of condition monitoring have been an attractive subject for industrial field and hence for the academic research filed as well. More reliable solutions are required to be adopted by the industry applications in which usage of extra hardware, increased cost, and low estimation accuracy are the main challenges. Therefore, development of new condition monitoring methods based on software solutions could be the new era that covers the aforementioned challenges. A capacitance estimation method based on Artificial Neural Network (ANN) algorithm is therefore proposed in this paper. The implemented ANN estimated back converter. Analysis of the error of the capacitance estimation is also given. The presented method enables a pure software based approach with high parameter estimation accuracy.

Keywords* -** Capacitor condition monitoring; capacitor health status; Capacitance estimation.***

I. INTRODUCTION

Condition monitoring is an important strategy to estimate the health condition of power electronic components, convert- ers and systems. It is widely applied in reliability or safety critical applications, such as wind turbines, electrical aircraft, electric vehicles, etc., enabling the indication of future failure occurrences and preventive maintenances. In [1], the condition monitoring of semiconductor devices used in power electronics is well reviewed. Besides the power devices, and according to [2], electrolytic capacitors are sharing 60% of the failure distribution for power converter elements as shown in Fig.1, therefore, capacitors are another type of reliability critical components.

In the last two decades, a large number of research results on condition monitoring of capacitors has been published. The majority of the condition monitoring methods for capacitors are based on estimation of the capacitance C and equivalent series resistance (ESR), which are indicators of the degradation of capacitors [3]. For aluminum electrolytic capacitors, the widely accepted end-of-life criteria are 20% capacitance reduction or double of the ESR. For film capacitors, a reduction of 2% to 5% capacitance may indicate the reach of end-of-life. Therefore, a method which can estimate the C value could be applied on both aluminum electrolytic and film capacitors. However, obtaining the values of C or ESR is an important step since it gives an indication of the ageing process and its acceleration. Fig. 2(a) shows a simplified equivalent model of capacitors and Fig. 2(b) plots the corresponding frequency characteristics. It can be noted that the capacitor impedances are distinguished by three frequency regions dominated by capacitance, ESR and the Equivalent Series Inductance (ESL), respectively.

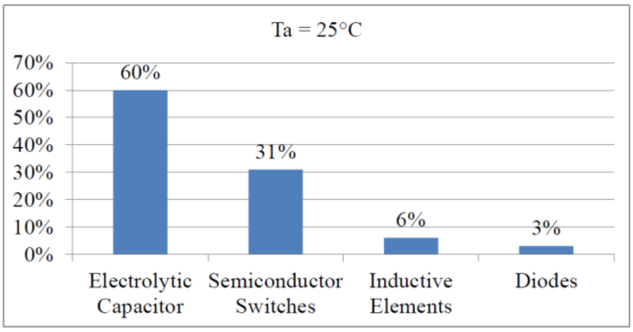

Fig .1. Distribution of failure for power converetr elements [2

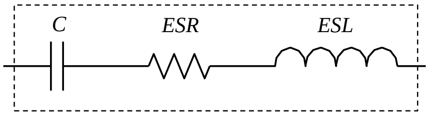

(a) Simplified equivalent model of capacitors

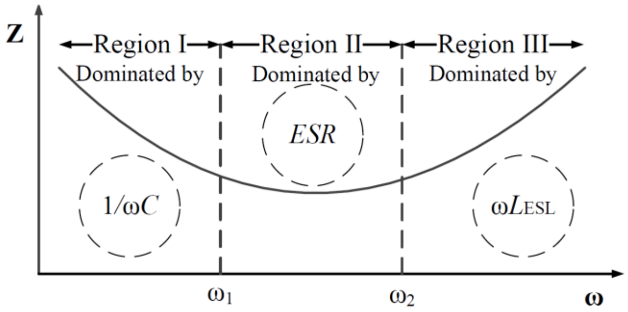

(b) Impedance characteristic of capacitors

Fig .2. Equivalent model and impedance characteristics of capacitors.

From the methodology point of view in [4], condition monitoring methods in the literature are classified into three categories as the following: a) Capacitor ripple current sensor based methods, b) Circuit model based methods, and c) Data and advanced algorithm based methods. The following three subsections are defining the principle of each category with its corresponding examples from the literature.

A. Capacitor ripple current sensor based methods

The basic principle of the this category is to estimate the capacitance and/or the ESR by using the capacitor ripple voltage and current information at region I and II (as shown in Fig. 2(b)). In [2, 5–7], an external current injection at low fre-quency is the main approach to achieve condition monitoring, it has been applied to PWM AC/DC/AC converter in [2], [5], and [7], while in [6] it has been applied to a sub-module capacitor in moulder multilevel converter.

B. Circuit model based methods

This category is based on that instead of injecting external signals, the capacitor current can be obtained indirectly de- pending on both the circuit model and the operation principle of PWM switching converters. In [8], an on-line condition monitoring based on capacitance estimation is proposed, the capacitor ripple current is calculated using the difference between the input current sensor, and the output current flows to the inverter which is based on the transistor switching statues.

C. Data and advanced algorithm based methods

This category, obtaining a strong correlation between the available parameters and the parameters to be estimated is the main concept. In [9], an external voltage is injected to the reference voltage of the capacitor at low frequency, the obtained capacitor power is used as a training data in sake of finding an identification model based on Support Vector Regression (SVR). After using a group of training data, a generated function is used to analyse the correlation between the known capacitor power and its corresponding capacitance value. Although the previous mentioned methods have been ver- ified by simulation and experimental work, errors, complex- ity, and cost increasing due to extra hardware are common shortcomings. Therefore, the developed technologies are rarely adopted in practical industry applications, implying that new condition monitoring methods based on software solutions and existing feedback signals, without adding any hardware cost, could be more promising in practical applications.

This paper aims to propose a condition monitoring method based on Artificial Neural Network (ANN) that uses existing power stage and control information and existing spare re- sources of digital controllers. It requires no extra hardware cir- cuitry (e.g., current sensors and corresponding signal condition circuits), no external signal injection, and therefore minimises the increased complexity and cost. Main sections in this paper are as the following: Section II gives the basic principle of ANN applied for capacitor condition monitoring. Section III illustrates the applied ANN to a back to back converter study case. Section IV presents the results achieved by the proposed method based on ANN, followed by the conclusion.

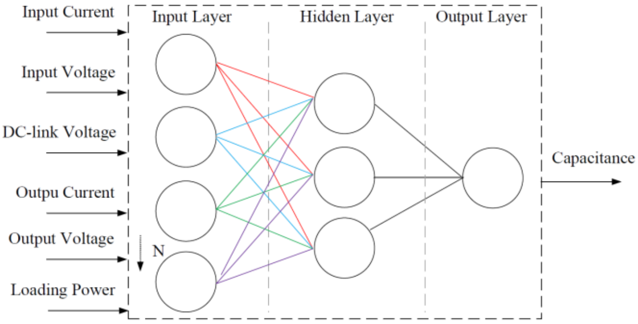

Fig .3. The structure of the Artificial Neural Network.

II. ANN FOR CAPACITOR CONDITION MONITORING

Implementation of capacitor condition monitoring using ANN is motivated by the shortcomings that have been investigated earlier in this paper. Avoiding the usage of direct/indirect current sensors is one of the main advantages of using ANN to obtain the estimated value of C. Instead of sensing the capacitor current iC, only the input terminal and output terminal information of the power converters are used as inputs to the ANN, while the capacitance is the ANN's target, and then the network is responsible for estimating the value of C when using different inputs than the trained ones. Normally, during the operation of the power converter, the required terminal information to train the ANN is supposed to be available. Taking the power level of the applied converter into consideration while the network is trained, is improving the ANN's estimated results by being more robust against dynamic variations of the loading power. Fig.3 illustrates the structure of the proposed ANN. The basic structure of any neural network consists of three layers, input, hidden, and output layers. The input layer is where the available amount of data N fed to the ANN will be stored. The hidden layer job is to transform the inputs into a function that the output layer can use, while the output layer transforms the hidden layer activations into a scale which the operator wanted the output to be on target.

III. CAPACITANCE ESTIMATION BASED ON ANN

Capacitance estimation based on ANN is applied to a back to back converter as shown in Fig. 4. The specifications of the converter are listed in Table I.

Capacitance values in the range between (1000μF and 5000μF) with 100μF step are used as targets to the network, each value of these 41 samples corresponds respectively to the single phase RMS input/output voltages, currents, and the DC-link voltage. Since the different loading condition of the back-to-back converter is also considered, three groups of 41 samples under the respective loading level of 10 kW, 7 kW and 4 kW are used.

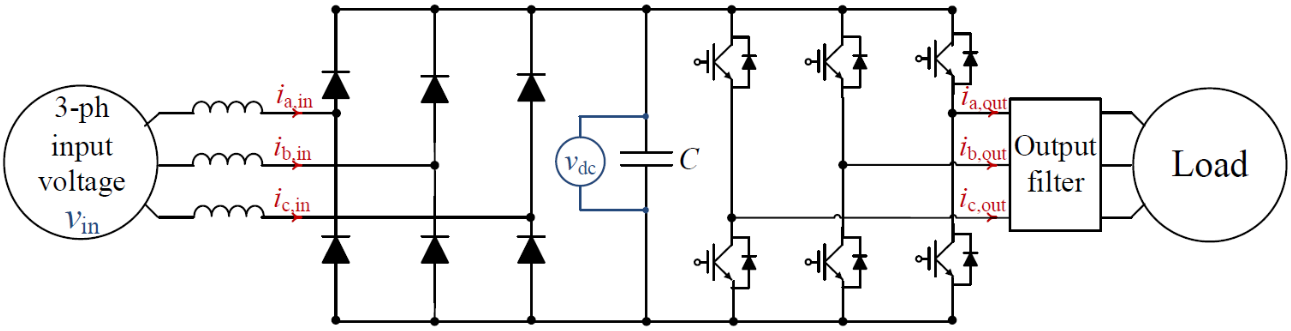

Fig .4. A back-to-back converter.

Table 1. THE SPECIFICATIONS OF THE BACK-TO-BACK CONVERTER PARAMETERS.

Input AC Voltage (V_{L-L})	600 V
Output AC Voltage (V_{L-L})	380 V
Rated DC-link Voltage (V_{dc})	780 V
Full Power Level (P_o)	10 kW
Capacitance (C)	5000 μF

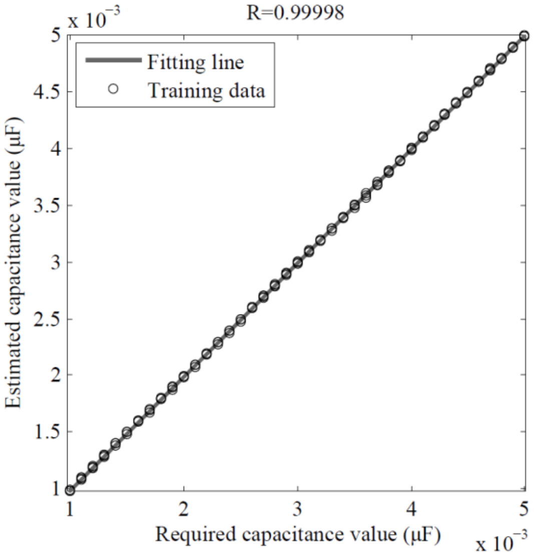

Fig .5. Regression responce of the trained network..

All the 123 samples are fed to a single hidden layer ANN consisting of 10 neurons using the Neural Fitting Tool (nftool) in MATLAB software. This tool is usually used for estimation and prediction of problems in which the neural network maps between a data set of numeric inputs and a set of numeric targets. The iteration algorithm used in this training is Levenberg-Marquardt, which typically takes more memory but less time. The training automatically stops when generalisation stops improving, as indicated by an increase in the mean square error of the validation samples. During the training observing the Regression value R is important, since Regression values measure the correlation between outputs and targets. An R value of 1 means a close relationship, while 0 means a random relationship. Fig. 5 shows the regression response of the trained network in this paper. It can be noted that all the 123 input data are exactly aligned on the fitting line and the values of R are close to 1. Based on this result, the network stopped training and the ANN is generated to be used.

IV. SIMULATION RESULTS AND DISCUSSION

In this section, the trained network is tested for verification purpose. The inputs to the ANN are stored in the Matlab work- space, and they are sent to the ANN as a group set every 0.2 seconds. Each group set is resulting in one corresponding output (estimated C value). The same group set of inputs is sent until a new set is available in the work-space. The same back to back converter as shown in Fig. 4 is used for the simulation test, but with two capacitors C1 and C2 connected in parallel through switches to have the option to switch between them to simulate the degradation of C. At the timing (5 sec) the capacitor C2 will be switched on instead of C1 . Fig.6 shows the capacitance value estimated by the trained ANN. The simulation results for the estimated parameters and their corresponding errors are shown in Table II. The estimated results verify that the trained ANN is responding for the changes in the capacitance value, and the statues of the capacitor could be easily identified.

Table 2. SIMULATION RESULTS FOR ESTIMATED CAPACITANCE..

C1*actual*=5000μF	C1*estimated*=4991μF	Error=0.18%
C2*actual*=4000μF	C2*estimated*=3996μF	Error=0.1%

Moreover, to prove the accuracy of the trained ANN, the network is tested to identify the reduction of 50μF out of 5000μF and the resulted estimation is shown in Fig. 7. For the initial stage, the estimated value is 4991μF and for the degraded case, the estimated value is 4945μF, which gives a 0.18% error as a maximum.

To test the robustness of the trained ANN against loading power variations, the ANN is tested to estimate a capacitance value of 5000μF during a loading power change. The esti- mated results with their corresponding errors percentage are shown in Fig. 8.

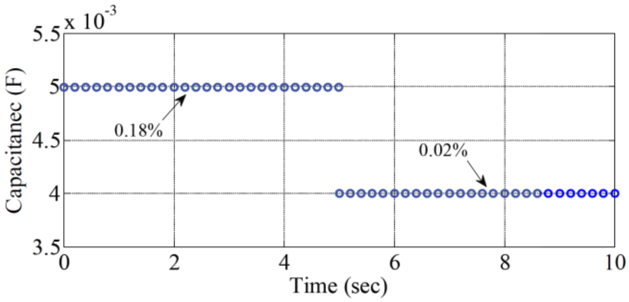

Fig .6. Tested DC-link capacitor change in a back-to-back converter.

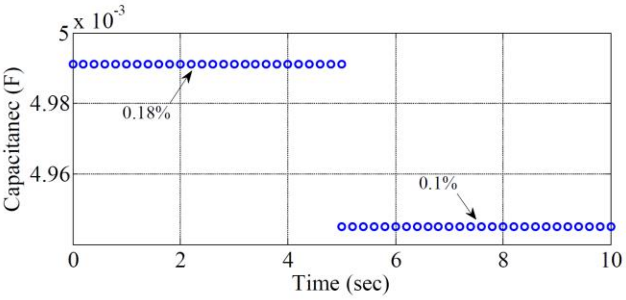

Fig .7. Trained ANN accuracy for the capacitance change shown in Fig. 6.

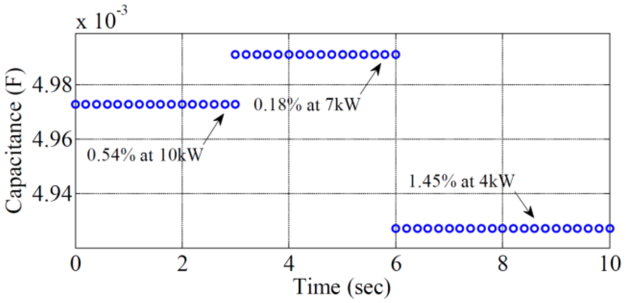

Fig .8. Trained ANN accuracy for the loading power change.

Moreover, for further verification of the ANN accuracy, a set of random values of capacitance between the ranges of (1000μF-5000μF) are applied under three different power levels, their actual and estimated values are shown in Fig.9. The actual and estimated values of capacitance of the set applied under 70% power level are presented in Table III.

In sake of showing the impact of the training data amount on the accuracy of the trained ANN, another network (ANN2) is trained by using 63 samples instead of 123 samples considering the same conditions of (ANN1) which have been trained earlier in this paper. Fig. 10 shows that the errors estimated by ANN2 are higher than the ones estimated previously by ANN1, implying the trade-off between estimation accuracy and required computation resource.

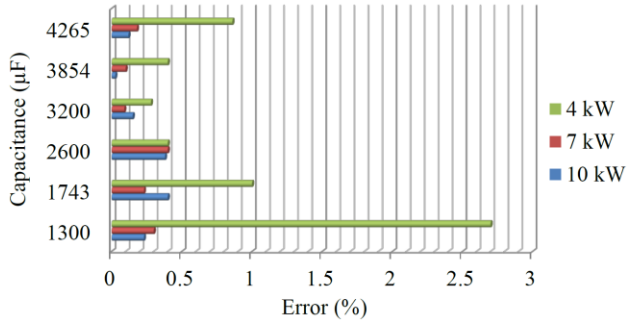

Fig .9. Estimation error analysis under different level of power.

Table 3. SIMULATION RESULTS FOR ESTIMATED CAPACITANCE (AT 7KW).

$C_{actual}=1300\mu F$	$C_{estimated}=1296\mu F$	Error=0.3%
$C_{actual}=1743\mu F$	$C_{estimated}=1747\mu F$	Error=0.23%
$C_{actual}=2600\mu F$	$C_{estimated}=2589\mu F$	Error=0.4%
$C_{actual}=3200\mu F$	$C_{estimated}=3203\mu F$	Error=0.09%
$C_{actual}=3854\mu F$	$C_{estimated}=3850\mu F$	Error=0.1%
$C_{actual}=4265\mu F$	$C_{estimated}=4257\mu F$	Error=0.18%

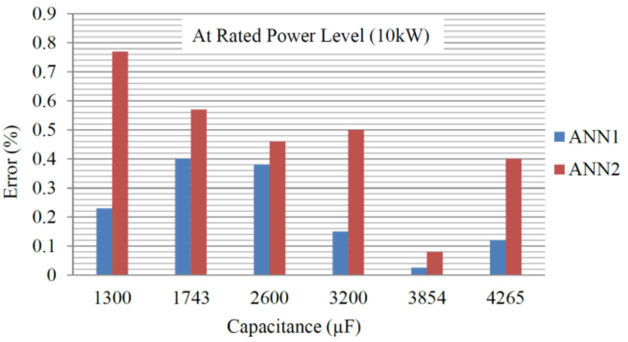

Fig .10. Estimation error analysis by different trained ANNs.

The last accuracy analysis is performed to observe the error percentage of the estimated capacitance with respect to different degree of changes of the original value of 5000μF, the results are shown in Fig. 11. It can be noted that the estimation errors of the proposed ANN are below 0.25%. It can respond and estimate correctly the capacitance values even under a very low level of capacitance reduction of 0.2% changes.

The following remarks are given from the results presented in this section:

- The simulation results of the proposed method based on ANN verify that condition monitoring methods based on software solutions could be an attractive alternative for the practical industry applications.

- It can be noted from the results that trained ANN is capable to respond to a very small change of capacitance and estimate the capacitance value within the range in which the network is trained.

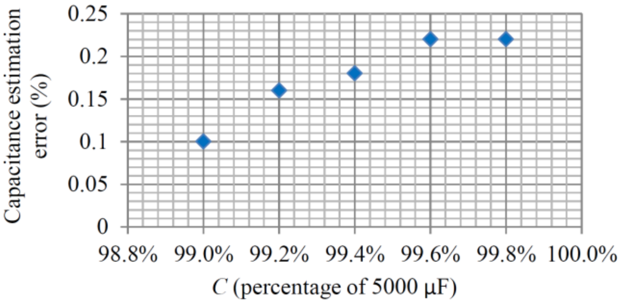

Fig .11. Estimation error analysis under different level of capacitance reduction at rated power level.

- It should be noted that the accuracy of the trained ANN strongly depends on the amount, quality, and accuracy of the data used in the training.

V. CONCLUSIONS

A new capacitor condition monitoring method based on Artificial Neural Network algorithm is proposed in this paper. It is applied to a back-to-back converter study case to estimate the capacitance value change of the DC-link capacitor. The proposed method requires no additional hardware circuit and could be implemented by using the spare resources of existing digital controllers in most of power electronic systems, implying a minimum increased cost (e.g., only in the research and development part). The error analysis under different DC-link capacitance values and different level of capacitance reduction with respect to the initial value are given, achieving a maximum estimation error that is well below 0.5%, which could be acceptable in many practical applications. The impact of training data amount on the error analysis is also given.

REFERENCES

[1] S. Yang, D. Xiang, A. Bryant, P. Mawby, L. Ran, and P. Tavner, “Condition monitoring for device reliability in power electronic converters: A review,” IEEE Transactions on Power Electronics, vol. 25, no. 11, pp. 2734–2752, Nov 2010.

[2] X.-S. Pu, T. H. Nguyen, D.-C. Lee, K.-B. Lee, and J.-M. Kim, “Fault diagnosis of dc-link capacitors in three-phase ac/dc pwm converters by online estimation of equivalent series resistance,” *IEEE Transactions on Industrial Electronics*, vol. 60, no. 9, pp. 4118–4127, Sept 2013.

[3] H. Wang and F. Blaabjerg, “Reliability of capacitors for dc-link applications in power electronic converters-an overview,” *IEEE Transactions on Industry Applications*, vol. 50, no. 5, pp. 3569–3578, Sept 2014.

[4] H. Soliman, H. Wang, and F. Blaabjerg, “A review of the condition monitoring of capacitors in power electronic converters,” in *Electromotion Joint International Conference (ACEMP - OPTIM), 2015 IEEE*, August 2015, pp. 243–249.

[5] D.-C. Lee, K.-J. Lee, J.-K. Seok, and J.-W. Choi, “Online capacitance estimation of dc-link electrolytic capacitors for three-phase ac/dc/ac pwm converters using recursive least squares method,” *in Proceedings of Electric Power Applications*, vol. 152, no. 6, pp. 1503–1508, Nov 2005.

[6] Y.-J. Jo, T. H. Nguyen, and D.-C. Lee, “Condition monitoring of submodule capacitors in modular multilevel converters,” in *Energy Conversion Congress and Exposition (ECCE), 2014 IEEE*, Sept 2014, pp. 2121–2126.

[7] T. H. Nguyen and D.-C. Lee, “Deterioration monitoring of dc-link capacitors in ac machine drives by current injection,” *IEEE Transactions on Power Electronics*, vol. 30, no. 3, pp. 1126–1130, March 2015.

[8] A. Wechsler, B. Mecrow, D. Atkinson, J. Bennett, and M. Benarous, “Condition monitoring of dc-link capacitors in aerospace drives,” *IEEE Transactions on Industry Applications*, vol. 48, no. 6, pp. 1866–1874, Nov 2012.

[9] A. Abo-Khalil and D.-C. Lee, “Dc-link capacitance estimation in ac/dc/ac pwm converters using voltage injection,” *IEEE Transactions on Industry Applications*, vol. 44, no. 5, pp. 1631–1637, Sept 2008.

Investigation of Efficiency and Thermal Performance of the Y-source Converters for a Wide Voltage Range

Brwene Gadalla, Erik Schaltz, Member IEEE,Yam Siwakoti, Member IEEE, Frede Blaabjerg, Fellow, IEEE
Department of Energy Technology, Aalborg University,
Aalborg 9220, Denmark,
bag@et.aau.dk, esc@et.aau.dk, yas@et.aau.dk, fbl@et.aau.dk

Abstract - The Y-source topology has a unique advantage of having high voltages gain with small shoot through duty cycles. Furthermore, having the advantage of high modulation index increases the power density and improves the performance of the converter. In this paper, a collective thermal and efficiency investigation is performed in order to improve the reliability of the converter. Losses evaluation in the semiconductor devices (switching/conduction), the capacitors (ESR), and the inductors (core/winding) are presented. Moreover, the junction temperature evaluation of the devices is considered under 25◦ C ambient temperature. The analysis is carried out at the following voltages gain (2, 3, and 4), and at the following winding factors (4, and 5) using PLECS toolbox. The results show that, the power losses and the junction temperature are directly proportional with the voltage gain and the winding factor.

Keywords – Y-Source Converter-core losses-winding losses-Thermal-Voltage gain-Duty cycle.

I. INTRODUCTION

Y-source power converter has been used in many renewable energy applications such as; renewable generation systems [1], fuel cell applications [2], and more recently with electric vehicles [3]. Due to the importance of the thermal behaviour from the reliability point of view, a collective investigation of efficiency and thermal performance has to be done for the Y-source converter. Unreasonable temperature during the operation of the converter affects the performance, the devices lifetime, and hence, the reliability of the power electronic components in the converter. Therefore, controlling the tempera- ture within the reasonable limits provides: 1- higher power densities. 2- lower cost system configuration. 3- reliability improvement from lifetime point of view. 4- increase of the overall efficiency of the converter. 5- insuring safety and preventing the catastrophic design mistakes.

Practical applications require high switching frequency with small shoot through cycles to reduce the power losses during the turn-on and turn-off transients. For a short duration, a high current passes through the switch causing high voltage stress and high junction temperature. Moreover, having higher voltages gain increases the stress in the device which needs to be designed carefully. Thus, it is very important to consider the thermal challenges earlier in the design stage. Considering these challenges improves the performance of the converter by protecting the devices to be exposed to excessive temperatures that shorten their lifetime [4], and hence, the reliability of the converter.

This paper aims to investigate the thermal performance of the Y-source converter operating under 500 W at switching frequency of 20 kHz [5], [6], and [7]. The investigation is considered at voltages gain (2, 3, and 4), and at winding factors (4, and 5). The main sections in this paper are as follows: Section II gives the topology of the Y-source converter and its theory of operation. Section III illustrates the calculations of the efficiency and losses. Section IV presents the simulated case studies. Section V presents the simulation results and discussion, followed by the conclusion.

II. TOPLOGY AND THEORY OF OPERATION

The Y-source converter is a very promising topology for higher voltage gain in a small duty ratio and in a very wide range of adjusting the voltage gain [6]. Very high modulation index can be achieved with this topology as well. The range of duty cycle in the Y-source is narrower than Z-source and the boost and higher in the modulation index. Fig.1 (a) shows the Y-source impedance network is realized a three-winding coupled inductor (N1, N2, and N3) for introducing the high boost at a small duty ratio for SW. It has an active switch SW, passive diodes (D1, D2), a capacitor C1, the windings of the coupled inductor are connected directly to SW and D1, to ensure very small leakage inductances at its winding terminals.

- In the ST state, when the switch is turned on, D1 and D2 are off causing the capacitor C1 to charge the magnetizing inductor of the coupled transformer and capacitor C2 discharge to power the load.

- In the NST state, when the switch is non-conducting,D1 starts to conduct causing the input voltage to recharge the capacitor C1 and the energy from the supply and the transformer to flow to the load and when D2 starts conducting, it recharges C2 and the load to be continuously powered.

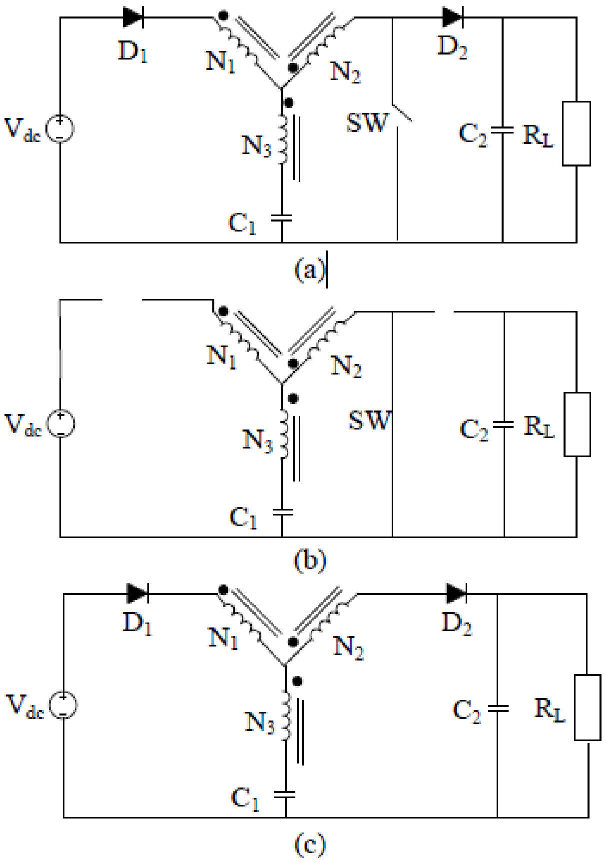

Fig .1. Illustration of a)Y-source converter, b) its equivalent "ST state", and c) its equivalent "NST state" circuits..

The input /output voltage relation and the duty cycle isexpressed in (1)

$$V_{out} = \frac{V_{in}}{(1-KD)} \qquad (1)$$

where, V_{out} is the output voltage, V_{in} is the input voltage, D is the duty cycle and K is the winding factor.

The winding factor K is calculated according to the turns ratio of the three-winding coupled inductor as expressed in (2)

$$K = \frac{N_1 + N_3}{N_3 - N_2} \qquad (2)$$

where, (N_1 : N_2 : N_3) is the turns ratio of the coupled inductor.

And the modulation index M of the Y-source is expressed in (3)

$$M = 1.15\,(1-D) \qquad (3)$$

where, D is the duty cycle required for the voltage gain and M is the modulation index.

III. EFFICINCY AND LOSS CALCULATIONS

In this section, further illustration for the formulas used in calculating the relevant losses and verified by the simulation results. Having passive elements in the Y-source circuit, may have some advantages as 1) minimizing the stresses according to the desired design, 2) reduceing the switching and conduction losses on the devices, 3) lowering shoot through duration, since they are storing energy.

A. Switching and conduction losses calculations

Switching losses occurs when the device is transitioning from the blocking state to the conducting state and vice-versa. This interval is characterized by a significant voltage across its terminals and a significant current through it. The energy dissipated in each transition needs to be multiplied by the frequency to obtain the switching losses:

The switching losses P_{sw} are expressed in (4):

$$P_{sw} = (E_{on} + E_{off}) \times f_{sw} \qquad (4)$$

Where, E_{on} and E_{off} are the energy losses during on and off of the switch, f_{sw} is the switching frequency. Conduction losses occurs when the device is in full conduction. The current in the device is whatever is required by the circuit and the voltage at its terminals is the voltage drop due to the device itself. These losses are in direct relationship with the duty cycle.

The average conduction losses P_{cond} are expressed in (5):

$$P_{avg.cond} = \frac{1}{T}\int_0^T [v_{ce}(t) \times i_{ce}(t)]\, dt \tag{5}$$

where, v_{ce} is the on state voltage, an i_{ce} is the on state current. And in (6):

$$\mathrm{T} = \frac{1}{\mathrm{f}_{\mathrm{sw}}} \tag{6}$$

B. Capacitor ESR losses calculations

The Equivalent Series Resistance ESR is the value of resistance which is equal to the total effect of a large set of energy loss mechanisms occurring under the operating conditions. So, the capacitors losses are expressed in (7):

$$\mathbf{P}_{\mathbf{cap.loss}} = \mathbf{I}^2_{\mathbf{cap.}} \times \mathrm{ESR} \tag{7}$$

where, $I_{cap.}$ is the rms current passing through the capacitor, and ESR is the equivalent series resistance measuring the effect of the losses dissipated in the capacitor.

C. Winding and core losses calculations

According to Steinmetz's equation [8], which is a physics equation used to calculate the core loss of magnetic materials due to magnetic hysteresis.

The core losses are expressed in (8):

$$P_v = k f^{\alpha} \hat{B}^{\beta} \tag{8}$$

Where, $\hat{B}$ is the peak induction of a sinusoidal excitation on the efficiency and junction temperature performances. Furthermore, measuring all the relevant losses as listed in section with frequency f, P_v is the time-average power loss per unit volume, and the material parameters (α, β, k) are material parameters.

The improved generalized Steinmetz's equation is expressed in (9):

$$P = \frac{1}{T}\int_0^T k_i \left|\frac{dB}{dt}\right|^a \left(\Delta B^{b-a}\right) dt \tag{9}$$

Where, ΔB is the flux density from peak to peak and in (10):

$$k_i = \frac{k}{(2\pi)^{\alpha-1}\int_0^{2\pi} |cos\theta|^{\alpha} \times 2^{\beta-\alpha} d\theta} \tag{10}$$

Where, *(β, α, k)* are the material parameter found by curve fitting, and θ is the angle of the sinusoidal waveform simulated.

IV. CASE STUDIES

In this section, simulations are carried out to verify the performance of the Y-source converter using the parameters listed in Table I.

Table 1. THE USED PARAMETERS OF THE SIMULATED MODEL.

Parameters	**Values / Models**
Input voltage V_{in}	100 V - 133 V - 200 V
Output voltage V_o	400 V
Output Power P_o	500 W
Switching frequency f_s	20 kHz
Resistive load R_l	320 Ω
MOSFET *SW*	SPW47N60C3 650 V, 47 A
Diode $D_1 - D_2$	SD600N/R 600 V, 600 A
Core type *V*	MPP C055863A2

Table 2. SIMULATION PARAMETERS AT THREE CASES.

Parameters	**Values**
Size of AWG	15
Winding factor *K*	4 5
Turns ratio $N_1 : N_2 : N_3$	80:16:48 48:16:32
DC-resistance $R_{dc-Y\ source}$	0.0735 Ω 0.0441Ω
	0.0147 Ω 0.0147Ω
	0.0441 Ω 0.0294Ω

The ratings of the devices are chosen according to the voltage and current stresses across them. Where, investigating the impact of varying the voltage gain and the winding factor on the efficiency and junction temperature performances. Fur- thermore, measuring all the relevant losses as listed in section While having the same switching frequency 20 kHz, rated power 500 W, and constant ambient temperature 25 ◦C. Table II summarize the case studies investigated.

- Case 1:

Simulation was carried out with voltage gain factor 2 with different value of shoot-through ratio, using winding factors 4 and 5. The rated power 500 W was applied to all the simulations.

- Case 2:

Simulation was carried out with voltage gain factor 3 with different value of shoot-through ratio, using winding factors 4 and 5.

- Case 3:

Simulation was carried out with voltage gain factor 4 with different value of shoot-through ratio, using winding factors 4 and 5.

V. SIMULATION RESULTS AND DISSCUSION

PLECS toolbox is used for the Y-source converter circuit. All the relevant losses results are calculated based on the afore-mentioned equations in the simulated model. The simulated parameters are listed in Table II. Where, the comparison is between 2 different winding factors (4, and 5), and 3 different voltage gains (2, 3, and 4), the size of the wire is 15 AWG and the values of the DC resistance are calculated according to 11:

$$R_{dc} = R_{dc/singlelayer} \times \frac{N}{L} \tag{11}$$

Where, ($R_{dc/singlelayer}$) is the dc resistance per single layer, N is the no. of turns, and L is the length of single layer.

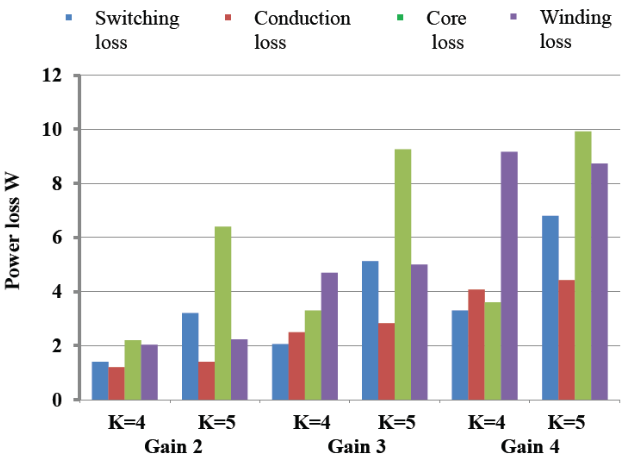

Fig .2. Representation of the relevant losses for cases I, II, and III.

Table 3. THE SIMULATED SHOOT-THROUGH DUTY CYCLE FOR EACH CASE.

Cases	Gain	Winding factor *K*		Duty cycle *D*	
Case I	2	4	5	0.125	0.1
Case II	3	4	5	0.16674	0.133
Case III	4	4	5	0.18754	0.15

Table 4. THE SIMULATED SHOOT-THROUGH DUTY CYCLE FOR EACH CASE.

Cases	Winding factor *K*		Total power losses *W*		Efficiency %	
Case I - Gain 2	4	5	6.93	13.19	98.61	97.48
Case II - Gain 3	4	5	12.6	22.2	97.5	95.8
Case III - Gain 4	4	5	20.2	29.9	96.1	94.4

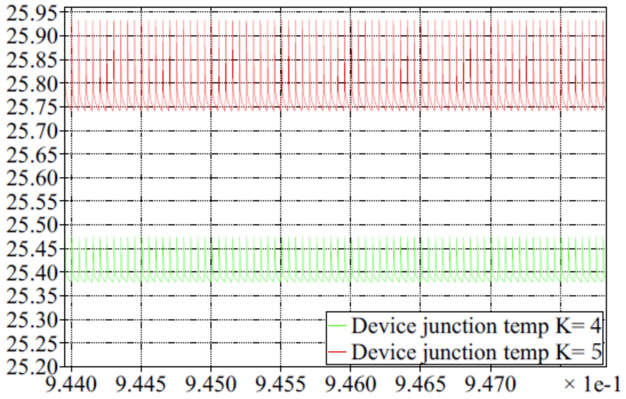

Fig .2 Junction temperation representation at gain 2 for K= 4 and K= 5.

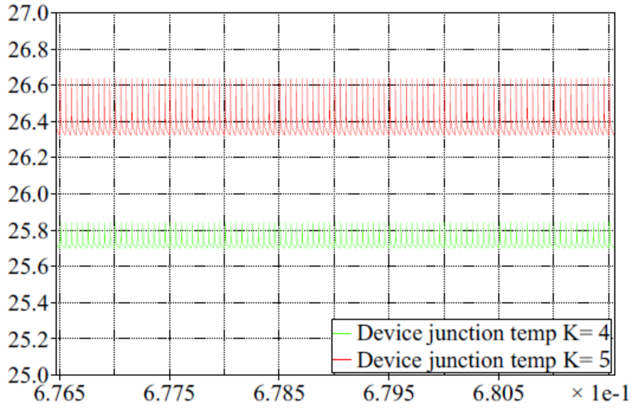

Fig .4 Junction temperation representation at gain 2 for K= 4 and K= 5.

Fig. 2 presents the difference between the relevant losses of the devices (switching, conduction, core and winding losses) for each winding factor and voltage gain. For the capacitor ESR losses, it can be neglected, since it is very small where, the largest is 0.26 watts at gain 4 and winding factor 5. For the shoot through duty ratios for each case is listed in Table III. The simulation results indicate that the higher the voltage gain and winding factor, the higher the power losses and the junction temperature which are listed in Table IV. For the junction temperature variation in the MOSFET for different gains and winding factors in steady state, Figures 3, 4 and 5 that show the behaviour of the junction temperature under different voltage gains and winding factors. The highest junction temperature is at voltage gain factor of 4 and winding factor of 5 as expected.

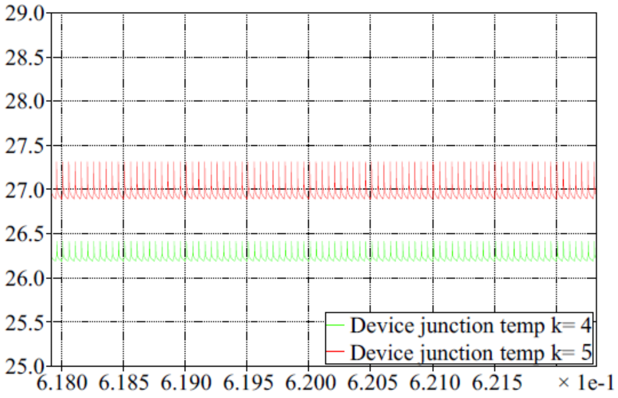

Fig .5 Junction temperation representation at gain 4 for K= 4 and K= 5.

VI. CONCLUSIONS

This paper investigates the thermal performance and the efficiency of semiconductor devices and passive elements in the Y-source converter of rated power 500 W. In sake of designing a reliable converter, the thermal performance is extremely important to be considered. Measurements of the junction temperatures and relevant losses are demonstrated. The impact of different voltage gains and winding factors is performed and studied. The measurements of the junction temperature variation shows that there is no overstress on the devices during the operation, this is due to the unique advantage in the Y-source converter of having high voltage gains with very small duty ratio. The results of the relevant losses with respect to varying the voltage gains and winding factor are reasonable. It can be seen from the results that while increasing the voltage gains and the winding factors, the total power loss increase as well. The performance of the Y-source converter is very promising. Although having voltage gain factor of 4, the performance is efficient and the converter's efficiency is ranging between 94.4 % and 96 % with respect to the winding factor variation.

REFERENCES

[1] J.-M. Shen, H.-L. Jou, and J.-C. Wu, "Ripple voltage suppression method for dc/dc boost converter of the grid- connected renewable power generation system," in IEEE International Conference on Sustainable Energy Technologies, 2008. ICSET 2008., Nov 2008, pp. 110–115.

[2] Y. Siwakoti, F. Z. Peng, F. Blaabjerg, P. C. Loh, and G. Town, "Impedance-source networks for electric power conversion part i: A topological review," IEEE Transactions on Power Electronics, vol. 30, no. 2, pp.

699–716, Feb 2015.

[3] O. Hegazy, J. Van Mierlo, and P. Lataire, “Analysis, control and comparison of dc/dc boost converter topologies for fuel cell hybrid electric vehicle applications,” in Proceedings of the 2011-14th European Conference on Power Electronics and Applications (EPE 2011), Aug 2011, pp. 1–10.

[4] A. K. Chanudhary, S. K. Singh, S. Singh, and F. Ahmed, “Reliability tests and thermal modelling for inverter in hybrid electrical vehicles,” International Journal of Scientific Technology Research, vol. 1, no. 4, pp. 1–5, May 2012.

[5] Y. Siwakoti, G. Town, P. C. Loh, and F. Blaabjerg, “Y- source inverter,” in IEEE 5th International Symposium on Power Electronics for Distributed Generation Systems (PEDG), 2014, June 2014, pp. 1–6.

[6] Y. Siwakoti, P. C. Loh, F. Blaabjerg, and G. Town, “Y- source impedance network,” in 2014 Twenty-Ninth Annual IEEE Applied Power Electronics Conference and Exposition (APEC),, March 2014, pp. 3362–3366.

[7] Y. Siwakoti, P. C. Loh, F. Blaabjerg, S. Andreasen, and G. Town, “Y-source boost dc/dc converter for distributed generation,” IEEE Transactions on Industrial Electronics,, vol. 62, no. 2, pp. 1059–1069, Feb 2015.

[8] J. Muhlethaler, J. Biela, J. Kolar, and A. Ecklebe, “Core losses under the dc bias condition based on steinmetz parameters,” IEEE Transactions on Power Electronics, vol. 27, no. 2, pp. 953–963, Feb 2012.

Scan the QR Code

Journal of
Renewable Energy and Sustainable Development

RESD

Volume 1, Issue 2 , December 2015 ISSN 2356-8569

ISSN 2356-8518

http://apc.aast.edu

مركز الأكاديمية للنشر
ACADEMY Publishing Center